Article

Developmental Cell

A Self-Organized PLT/Auxin/ARR-B Network Controls the Dynamics of Root Zonation Development in *Arabidopsis thaliana*

Graphical Abstract

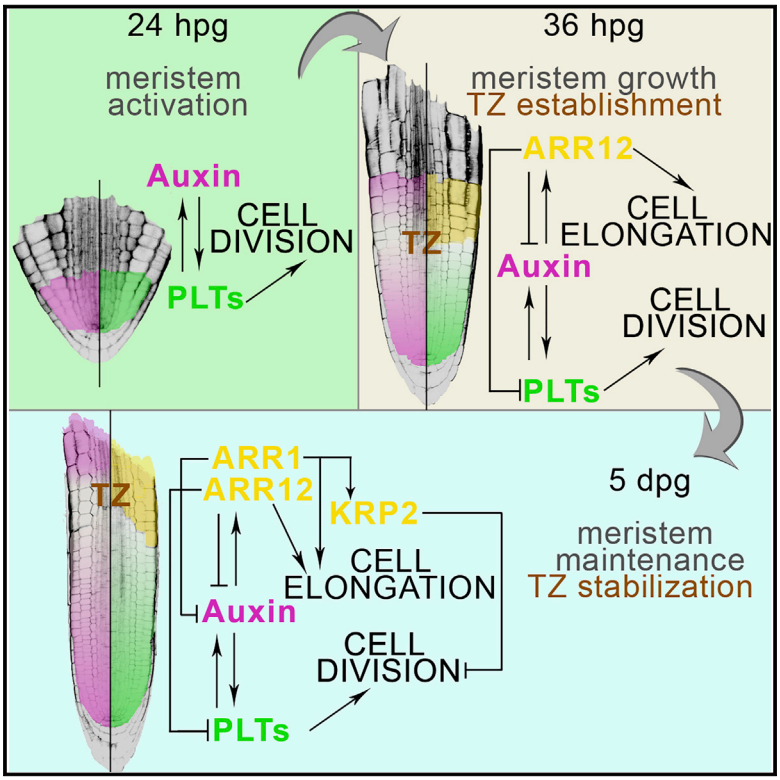

Highlights

- Upon germination, cell divisions generate a PLT drop that forms the transition zone
- A PLTs-ARR12 mutual antagonism restricts early root meristem expansion
- ARR1 repression of cell division via KRP2 is key for meristem size stabilization
- Auxin-PLTs-ARRs form a network responsible for self-organized root patterning

Authors

Elena Salvi, Jacob Pieter Rutten, Riccardo Di Mambro, ..., Raffaele Dello Ioio, Sabrina Sabatini, Kirsten Ten Tusscher

Correspondence

sabrina.sabatini@uniroma1.it (S.S.), k.h.w.j.tentusscher@uu.nl (K.T.T.)

In Brief

How organs grow and stabilize when reaching a functional size is a central question in biology. Using the root of *Arabidopsis* as a model system and combining molecular genetics with computational modeling, Salvi et al. unveiled an auxin-PLTs-ARRs molecular network controlling the self-organized patterning of the root from germination onward.

Salvi et al., 2020, Developmental Cell *53*, 1–13
May 18, 2020
https://doi.org/10.1016/j.devcel.2020.04.004

CellPress

Developmental Cell

CellPress

Article

A Self-Organized PLT/Auxin/ARR-B Network Controls the Dynamics of Root Zonation Development in *Arabidopsis thaliana*

Elena Salvi,[1,4] Jacob Pieter Rutten,[2,4] Riccardo Di Mambro,[3] Laura Polverari,[1] Valerio Licursi,[1] Rodolfo Negri,[1] Raffaele Dello Ioio,[1] Sabrina Sabatini,[1,5,*] and Kirsten Ten Tusscher[2,*]

[1]Department of Biology and Biotechnologies "C. Darwin," Laboratory of Functional Genomics and Proteomics of Model Systems, University of Rome "Sapienza", via dei Sardi, 70, 00185 Rome, Italy

[2]Computational Developmental Biology Group, Department of Biology, Utrecht University, Padualaan 8, 3584 CH Utrecht, the Netherlands

[3]Department of Biology, University of Pisa - via L. Ghini, 13, 56126 Pisa, Italy

[4]These authors contributed equally

[5]Lead Contact

*Correspondence: sabrina.sabatini@uniroma1.it (S.S.), k.h.w.j.tentusscher@uu.nl (K.T.T.)

https://doi.org/10.1016/j.devcel.2020.04.004

SUMMARY

During organogenesis, coherent organ growth arises from spatiotemporally coordinated decisions of individual cells. In the root of *Arabidopsis thaliana*, this coordination results in the establishment of a division and a differentiation zone. Cells continuously move through these zones; thus, a major question is how the boundary between these domains, the transition zone, is formed and maintained. By combining molecular genetics with computational modeling, we reveal how an auxin/PLETHORA/ARR-B network controls these dynamic patterning processes. We show that after germination, cell division causes a drop in distal PLT2 levels that enables transition zone formation and ARR12 activation. The resulting PLT2-ARR12 antagonism controls expansion of the division zone (the meristem). The successive ARR1 activation antagonizes PLT2 through inducing the cell-cycle repressor *KRP2*, thus setting final meristem size. Our work indicates a key role for the interplay between cell division dynamics and regulatory networks in root zonation and transition zone patterning.

INTRODUCTION

Organogenesis is a complex process in which different cells and tissues at different developmental stages need to be coordinated to guarantee the final shape of the organ. In plants, upon seed germination, the activities of localized structures called meristems allow organogenesis to continue after embryogenesis. Within meristems, stem cells generate all tissue types and sustain post-embryonic indeterminate organ growth.

In the model plant *Arabidopsis thaliana* at the end of embryogenesis, the root organ consists of a stem cell niche and few stem cell daughters (Scheres et al., 1994). Upon seed germination, the stem cell niche becomes active, building up the root meristem and initiating root growth. Stereotyped divisions of stem cell daughters generate cell files in which cells' distance from the tip reflects their age. In these early stages, cell division exceeds differentiation, causing the meristem to expand. At 5 days post seed germination (dpg) root meristem development is completed. A dynamic equilibrium is reached where cell division, fueling meristem expansion, is balanced by cell differentiation that constantly culls back meristem size, thus ensuring a stable number of meristematic cells. At this point, along the longitudinal axis, the root consists of the division zone (meristem), including the stem cell niche and transit amplifying daughter cells, and the elongation and differentiation zone, where cells stop dividing, elongate and differentiate. In each tissue, the boundary between dividing and elongating cells is called the transition boundary, with boundaries of different cell files constituting the transition zone (TZ) (Figure 1A).

Several factors are known to be involved in patterning root zonation and positioning of the TZ: the polar transport of the phytohormone auxin leads to the formation of an auxin gradient with its maximum centered at the stem cell niche (Blilou et al., 2005; Grieneisen et al., 2007; Sabatini et al., 1999). Auxin controls the distribution of the PLETHORA (PLT) transcription factors, which also display a graded distribution (Aida et al., 2004). Importantly, auxin-induced *PLT* transcription only occurs near the stem cell niche, and cell division and cell-to-cell movement of the stable PLT protein play a critical role in PLT gradient formation (Mähönen et al., 2014). PLT protein has been shown to control root zonation in a dosage-dependent manner: high PLT levels near the quiescent center (QC) are necessary to maintain slow-mitotic stem cells, intermediate PLT levels in the meristem induce rapid cell divisions, and low PLT levels at the end of the meristem are necessary to allow cell expansion and differentiation (Galinha et al., 2007; Mähönen et al., 2014). Another key phytohormone, cytokinin (CK), was found to shape auxin distribution in the meristem. Cytokinin signaling, through the

Please cite this article in press as: Salvi et al., A Self-Organized PLT/Auxin/ARR-B Network Controls the Dynamics of Root Zonation Development in *Arabidopsis thaliana*, Developmental Cell (2020), https://doi.org/10.1016/j.devcel.2020.04.004

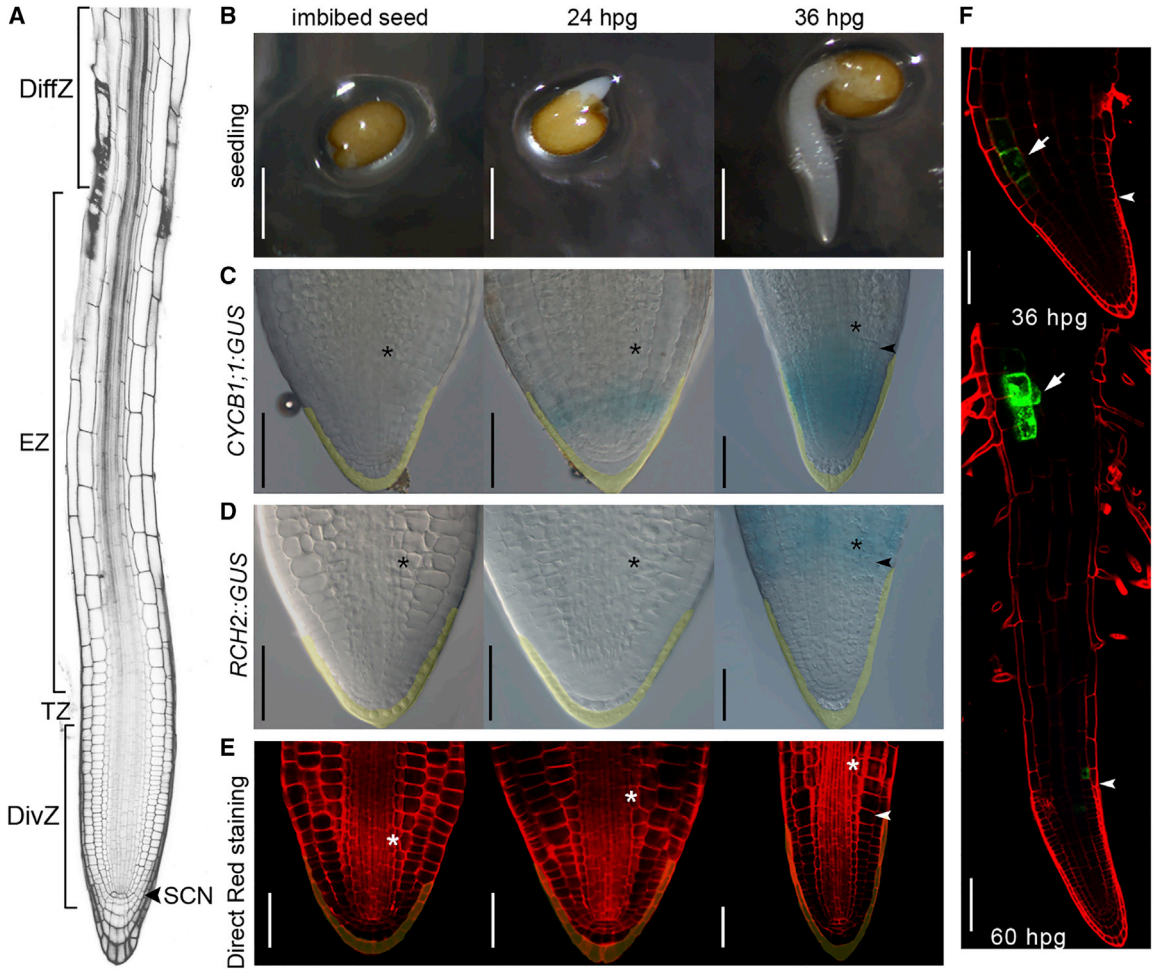

Figure 1. The TZ Appears Early upon Stem Cell Niche Activation

(A) Schematic representation of *A. thaliana* mature root zones. SCN, stem cell niche; DivZ, division zone; TZ, transition zone; EZ, elongation zone; and DiffZ, differentiation zone.

(B) Germinating wild-type seedlings and radicle protrusion from the seed at different time points: from the left; imbibed seed, 24 h after seed plating (hpg); 36 hpg. Scale bars represent 0.5 mm.

(C) Differential Interference Contrast (DIC) microscopy images of the histochemical β-glucuronidase (GUS) assay detecting *CYCB1;1:GUS* localization at different time points: from the left, seed, 24 hpg; 36 hpg.

(D) DIC microscopy images of the histochemical GUS assay detecting *RCH2:GUS* expression at different time points: from the left, 24 hpg; 36 hpg.

(E) Laser scanning confocal microscopy representative images of radicle morphology and appearance of the TZ at different time points: from the left; seed, 24 hpg; 36 hpg.

(F) Laser scanning confocal microscopy representative images of the clonal analysis in root meristems harboring the *DHCN4a* construct: at the top, at 36 hpg a GFP-positive multi-cellular clone is present in the incipient TZ. At the bottom, the same root at 60 hpg, where the same GFP-positive multi-cellular clone moved further shootward relative to the root tip but did not divide. Scale bars represent 50 μm. Arrowheads point the first elongating cell belonging to the incipient TZ, arrows point the GFP-positive multi-cellular clone.

In (C–E) asterisks mark the start of the hypocotyl, i.e., the first cells of the hypocotyl double-layered cortical tissue; the most external layer of the LRC tissue is false colored in light yellow; seed imbibed for 5 days, arrowheads point the first elongating cell belonging to the incipient TZ enclosed in the LRC tissue, scale bars represent 50 μm.

See also Figure S1.

ARABIDOPSIS RESPONSE REGULATOR 1 (ARR1) transcription factor, generates an auxin minimum that positions the TZ (Di Mambro et al., 2017).

Still, it remains unknown which regulatory mechanisms drive the unfolding and subsequent stable maintenance of the auxin, PLT, and cytokinin signaling activities that together dictate meristem size and TZ position. In particular, it is currently not known which processes trigger the establishment of the TZ and the onset of elongation and differentiation or how the balance between cell division and cell differentiation necessary for a stable meristem size and TZ position is achieved. As cells continuously move through and out of the meristem, this puts specific constraints on stable TZ positioning. Specifically, it requires the constant and dynamic reprogramming of meristematic cells into cells with differentiation features at a tightly controlled position. Thus, how initial TZ formation and its subsequent continuous

Please cite this article in press as: Salvi et al., A Self-Organized PLT/Auxin/ARR-B Network Controls the Dynamics of Root Zonation Development in *Arabidopsis thaliana*, Developmental Cell (2020), https://doi.org/10.1016/j.devcel.2020.04.004

CellPress

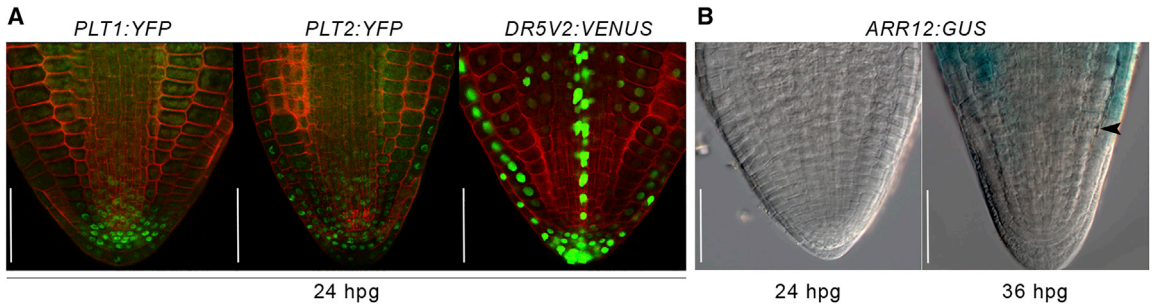

Figure 2. PLT1 and 2, Auxin Signaling Response, and ARR12 Expression Patterns in a Developing Root Meristem

(A) Confocal laser scanning microscopy images of the expression of *PLT1:YFP* (on the left), *PLT2:YFP* (middle), and *DR5V2:VENUS* (on the right) in 24 hpg germinating radicles. Scale bars represent 50 μm.

(B) DIC microscopy images of the histochemical GUS assay showing the delayed appearance and localization of *ARR12:GUS* construct in germinating roots at different time points: on the left at 24 hpg, on the right at 36 hpg. Black arrowhead points the incipient TZ. Scale bars represent 50 μm.

See also Figure S2.

re-patterning are achieved in a robust, self-organized manner is a central question in plant developmental biology.

To gain a system level understanding of the interplay between growth processes and molecular regulatory interactions, we combined experiments with a state-of-the-art model of root development incorporating cellular and tissue growth dynamics. Our results reveal how an auxin-PLT-ARR-B network enables the robust, self-organized formation and patterning of a developmental boundary, the TZ, thereby determining meristem size and overall root growth rate.

RESULTS

The TZ Appears Early upon Stem Cell Niche Activation

To get new insights in the molecular mechanism governing root growth dynamics, we first monitored early stages of root development using the cell-cycle reporter *CYCB1;1:GUS*, marking dividing cells, and the *RCH2::GUS* line, marking early stages of cell differentiation (Dello Ioio et al., 2008). At the end of embryogenesis, the root primordium consists of 8 meristematic cortex cells enclosed in the lateral root cap (LRC) (Figures 1B and S1). A few hours after seed stratification and exposure to light, germination starts with radical protrusion from the seed coat due to the elongation of hypocotyl-radicle junction cells (Sliwinska et al., 2009). Cell divisions in the radicle start only 24 h post-germination (hpg), as visualized by the presence of the *CYCB1;1:GUS* cell-cycle reporter (Figure 1C). This time point coincides with activation of the stem cell niche (Masubelele et al., 2005). No expression of the RCH2 marker line can be detected at this stage suggesting the absence of root cell differentiation activities (Figure 1D) and, hence, of a TZ. Indeed, no cells showing signs of elongation can be observed in the developing root meristem (Figures 1E, S1B, and S1C). Cell division progression causes the meristem to reach a number of 12 cortex cells at 36 hpg (Figures S1A–S1C). Interestingly, at this stage the *RCH2* marker line starts to be expressed in elongating cells defining a domain just above the developing root meristem, suggesting that these are the first postembryonic differentiated cells (Figure 1D).

To understand if these cells are indeed differentiated cells that can no longer divide, we performed clonal analysis experiments to follow their development over time and space.

With this aim, we used plants carrying a Cre/*lox* clonal system (*DHCN4a* construct) that randomly generated GFP clones in the root upon heat shock (Smetana et al., 2019). We heat shocked 36 hpg seedlings generating GFP-positive cells that we followed in time and space (Figure 1F, upper picture). Interestingly, GFP-positive cells lying in the *RCH2* expression domain did not divide and where pushed shootward relative to the root tip by the developing meristem (Figure 1F, lower picture).

Taken together, these data indicate that upon seed germination, the TZ is established at 36 hpg when the first postembryonic differentiated cells appear. Subsequently, the position of the TZ shifts away from the root tip until the meristem reaches its final, stable size at 5 dpg (Dello Ioio et al., 2008; Moubayidin et al., 2010; Ubeda-Tomás et al., 2009).

A Drop in PLT2 Levels Specifies the TZ

Next, we examined how TZ specification is controlled. Specifically, we investigated the roles of auxin, cytokinin, and *PLT* genes in this process. With this aim, we combined experimental evidence with computational modeling.

We initially monitored auxin distribution, expression of cytokinin signaling genes, and PLT expression in a developing root meristem of 24 hpg seedlings. At this stage of root meristem development, an auxin maximum (visualized by the *DR5V2::VENUS* construct) (Liao et al., 2015), coincides with a PLT maximum in the stem cell niche (visualized by the *PLT1:YFP* and *PLT2:YFP* constructs) (Galinha et al., 2007) (Figure 2A). We previously reported that during the initial steps of meristem development (3 dpg), cytokinin activity is mediated by the ARABIDIPSIS RESPONSE REGULATOR 12 (ARR12) cytokinin response factor (Moubayidin et al., 2010). Interestingly, in the root meristem of 24 hpg seedlings, no expression of ARR12 can be detected as revealed by plants carrying an *ARR12:GUS* construct (Figure 2B). ARR12 expression appeared only at 36 hpg coinciding with the appearance of the TZ and in a domain complementary to that of the PLTs and the auxin maximum (Figure 2B). Notably, among the ARR-Bs expressed in the root, ARR12 is the only one whose expression starts at 36 hpg and is TZ specific (Figures 2B and S2).

To understand the contribution of these elements in TZ patterning, we developed a dynamic computational model where the root layout consists of all the different root tissues, as well as

Please cite this article in press as: Salvi et al., A Self-Organized PLT/Auxin/ARR-B Network Controls the Dynamics of Root Zonation Development in *Arabidopsis thaliana*, Developmental Cell (2020), https://doi.org/10.1016/j.devcel.2020.04.004

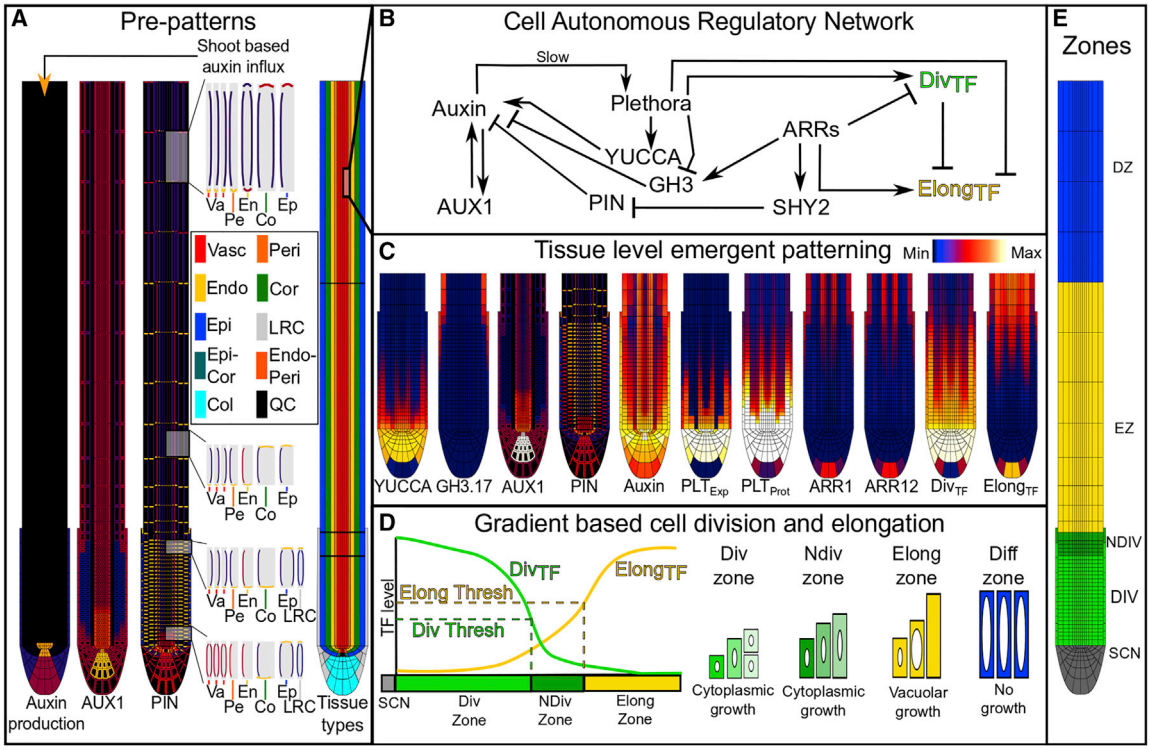

Figure 3. Overview of the Different Key Model Components and Their Interactions

(A) Patterns of auxin production (max level 50), AUX1 (max 3.0), and PIN (max 1.0) maximum expression levels and polarity are imposed in a cell and zone dependent manner. Modeled cell types, from outside to inside are epidermis (Epi), cortex (Cor), endodermis (Endo), pericycle (Peri), and vasculature (Vasc). Also included are QC, columella (Col), LRC, epidermal-cortical initials (Epi-Cor), and endodermal-pericycle initials (Endo-Peri).

(B) Cell autonomous regulatory network dictating intracellular auxin, PLT, and cytokinin signaling (ARRs) dynamics via affecting auxin import (AUX1), export (PIN), production (YUCCA), and degradation (GH3). Auxin, PLT and cytokinin signaling together control a division (DivTF) and elongation and differentiation (ElongTF) promoting factor.

(C) Dynamic spatial patterning of YUCCA (max 100), GH3.17 (max 100), AUX1 (max 300), and PIN (max 100) gene expression, auxin levels (max 1000, log scale), PLT expression ($PLT_{Exp,}$ max 500) and protein level ($PLT_{Prot,}$max 150) ARR1 and ARR12 expression (both max 100), division, and elongation ($Div_{TF,}$ $Elong_{TF,}$ both max 100) arising from the interplay between the imposed patterns in (A) and the regulatory network in (B).

(D) Longitudinal gradients of DivTF and ElongTF govern cellular division, expansion, and differentiation domains. When DivTF falls below the division threshold cells stop dividing. When the ElongTF exceeds the elongation threshold cells start elongating. Growth of dividing cells is cytoplasmic, diluting cell content. Elongation growth is vacuolar and without dilution.

(E) Root zonation dynamics. Modeled zones are root tip (gray), meristem; subdivided into a dividing (light green) and non-dividing zone (dark green), elongation zone (yellow), and differentiation zone (blue).

tissue specific patterns of auxin importers and exporters, hypocotyl derived auxin inflow, and QC centered local auxin production (Figure 3A), building on our earlier developed models (van den Berg et al., 2016; Di Mambro et al., 2017; Mähönen et al., 2014). Additionally, the model incorporates a cell autonomous regulatory network that controls the dynamics of and interactions between auxin, PLTs, and cytokinin signaling genes, including their effects on genes involved in auxin biosynthesis, degradation, and transport (Figures 3B and 3C). Dynamically patterned developmental zonation (Figure 3E) arises from a generalized division-promoting factor and differentiation-promoting factor, whose spatiotemporal dynamics depend on PLTs and cytokinin signaling dynamics (Figure 3B) (see STAR Methods). Finally, the levels of division and differentiation-promoting transcription factor (DivTF and ElongTF, respectively) determine cellular behavior. Below a certain level of the division factor, divisions stop whereas elongation and differentiation start once a certain level of differentiation factor is exceeded (Figure 3D). In between, cells grow slowly but no longer divide. Thus, importantly, root developmental zonation in our model is non-superimposed and highly dynamic. Zonation boundaries arise from the combined activities of the individual cell's networks together generating division and differentiation factor gradients. At the same time, the resulting zonation causes each individual cell to sequentially traverse the division, expansion, and differentiation zones. The initial state of the root layout consists of 8 cells for all tissues reflecting the anatomy of a 24 hpg root, i.e., before cell division starts (Figures S1A–S1C).

Given the absence of ARR12 at very early stages of root development, we first wondered to what extent the PLT proteins alone could drive the initial steps of TZ appearance. We have previously shown that in mature meristems auxin-induced PLTs control root zonation in a dosage-dependent manner (Mähönen et al., 2014). In particular, we showed that a drop of PLT proteins is necessary to allow the transition from dividing to differentiating cells. To investigate whether a drop in PLT proteins is responsible for TZ establishment, we measured PLT2 protein profiles

Please cite this article in press as: Salvi et al., A Self-Organized PLT/Auxin/ARR-B Network Controls the Dynamics of Root Zonation Development in *Arabidopsis thaliana*, Developmental Cell (2020), https://doi.org/10.1016/j.devcel.2020.04.004

CellPress

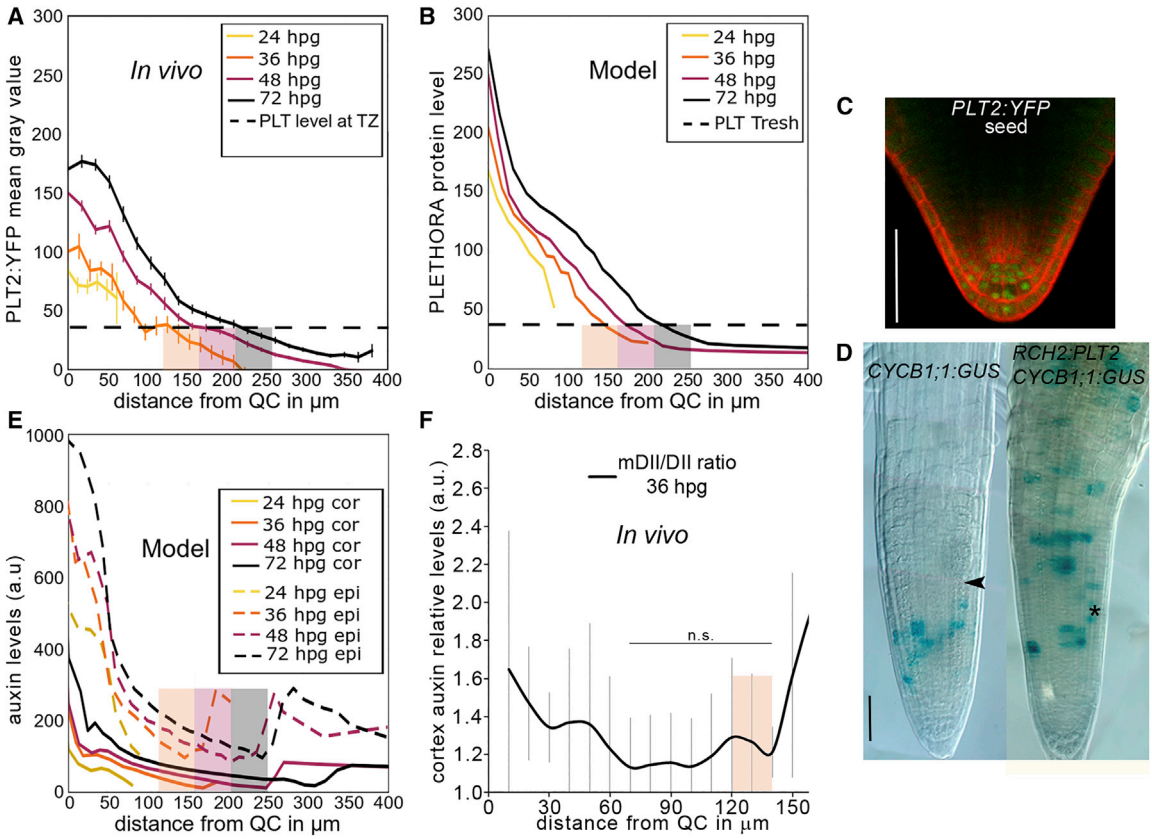

Figure 4. Establishment of the PLT Gradient and Its Role in Early Patterning *In Vivo*

(A) *In vivo* PLT2 gradient measured at 24 (yellow), 36 (orange), 48 (purple), and 72 (black) hpg in *PLT2:YFP* along the epidermal tissue (n = 10; error bars represent the SE). Mean gray values (y axis; a.u.) are shown as a function of the distance from the QC (x axis, µm). Shaded boxes are centered around the average TZ position found in wild-type roots at 36 (orange shade), 48 (purple shade), and 72 hpg (black shade). At 24 hpg, there is no TZ and meristematic PLT2 levels are uniform (one-way ANOVA $p > 0.6$). PLT2 TZ levels occurring at 36, 48, and 72 hpg are all significantly different from the PLT2 level at the end of the meristem at 24 hpg (one-way ANOVA $p < 2 \times 10^{-4}$, Student's t test 24 to 36, 48, 72 hpg all $p < 0.02$). Additionally, PLT2 TZ levels at 36, 48, and 72 hpg are consistent (cross comparison of levels at 36, 48, and 72 hpg all $p > 0.7$ for being different), enabling us to approximate a single PLT threshold level defining TZ position (dashed line). Further details can be found in STAR Methods.

(B) Model PLT gradient for wild-type settings fitted to experimentally observed PLT gradient dynamics shown in A. Colored bars indicating TZ position are taken from A and used to fit the model's PLT level below which division should halt (dashed line).

(C) Expression of *PLT2:YFP* in radicle of an imbibed seed (n = 15). Scale bar represents 50 µm.

(D) Histochemical GUS assay detecting *CYCB1;1:GUS* localization at 40 hpg in a wild-type root meristem and in a *RCH2:PLT2* background (n = 30). The asterisk marks the end of the root and the beginning of the hypocotyl, the black arrowhead indicates the cortex TZ. Scale bar represents 50 µm.

(E) Model auxin gradients at 24 (yellow), 36 (orange), 48 (purple), and 72 (black) hpg for wild-type model settings in cortical (continuous lines) and epidermal (dashed lines) cells. Colored bars are as in (B).

(F) Plot showing the *in vivo* quantification of relative auxin signaling of root tips harboring the *R2D2* construct via the ratio mDII/DII (between *mDII-ntdtomato* signal and *DII- nVENUS* signal) (y axis, a.u.) in each cortex cell along the root (x axis, distance from the QC in µm). The position where the incipient TZ is established (distance from the QC in µm) is shown as an orange-shaded box. Error bars represent SD. No significant difference (n.s. in the plot) between the mDII/DII ratios of the TZ position and −5 cells from the TZ toward the QC (one-way ANOVA for repeated measures test: F-ratio value = ~1.60; p value > 0.05). A significant difference ($p < 0.0005$) was found between the last meristematic cell (TZ position) and +2 cells (one-way ANOVA for repeated measures test: F-ratio value = 15.68; p value = 0.000027; Student's t test all p values < 0.005). Further details on the relative auxin signaling analysis can be found in STAR Methods.

See also Figure S3.

in *PLT2:YFP* roots at 24, 36, 48, and 72 hpg. We concentrated our efforts on PLT2 because changes in PLT2 protein levels are sufficient to affect meristem size. Specifically, ubiquitous overexpression of PLT2 increases meristem size whereas *plt2-2* loss-of-function mutant displays a slightly shorter meristem (Aida et al., 2004; Galinha et al., 2007).

In vivo PLT2 measurements revealed that a drop in PLT2 levels, coinciding with the independently determined location of the TZ, could only be identified in 36, 48, and 72 hpg roots (Figure 4A).

At 24 hpg, PLT2 longitudinal distribution was homogeneous and without a significant PLT2 drop (Figure 4A). These data suggest that the decrease in PLT2 levels observed at 36 hpg may be responsible for inducing cell differentiation, thus determining the appearance of the TZ. We then used this PLT2 profile to fit the parameters of our root model in order to reproduce the 24–72 hpg PLT profile dynamics (Figure 4B) (see STAR Methods). Our simulations show that in the absence of cell division, PLT distribution and TZ establishment, as observed *in vivo*, cannot be

Please cite this article in press as: Salvi et al., A Self-Organized PLT/Auxin/ARR-B Network Controls the Dynamics of Root Zonation Development in *Arabidopsis thaliana*, Developmental Cell (2020), https://doi.org/10.1016/j.devcel.2020.04.004

reproduced (Figure S3A). These data suggest that the onset of cell divisions at 24 hpg, through dilution of the PLT2 proteins, causes the decline in PLT2 levels (PLT drop) in the most shootward cells, establishing the TZ (Figure S3A). To verify *in vivo* if the presence of a PLT2 drop at 36 hpg can indeed explain the appearance of the TZ, we disrupted the PLT2 gradient expressing the PLT2 protein where the incipient TZ should appear, by using a *RCH2:PLT2* construct. In *RCH2:PLT2* seedlings, the *CYCB1;1:GUS* expression domain expands shootward, in a position where elongated cells should appear, indicating that these cells are still dividing and thus no elongation zone nor TZ could be detected (Figure 4D). Additionally, our model predicts that, given the slow auxin-mediated induction of *PLT2* expression (Mähönen et al., 2014), the observed PLT profile at 24 hpg in the model requires that *PLT* expression precedes germination (Figure S3B). Indeed, *PLT2:YFP* expression can be observed in the root stem cell niche of pre-germination seedlings confirming the model prediction (Figure 4C).

Interestingly, at 36 hpg, the model predicts the appearance of a diffuse auxin minimum, whose spatial location coincides with the drop in PLT2 levels (Figure 4E, compare Figure 4B). *In vivo*, the outline of a developing auxin minimum could be observed at 36 hpg a few cells rootward of the incipient TZ, by means of the *R2D2* construct, suggesting that they could both contribute to TZ establishment (Figure 4F). Nevertheless, precisely when the auxin minimum first appears and how it is coordinated with the PLT drop in order to establish the TZ remains to be investigated. Instead, in this study, we focus on how interactions between PLTs and CK signaling genes determine the dynamics of TZ positioning over the course of root development.

Taken together, these data indicate that a PLT gradient forms through a cell-division dilution effect upon germination. The accompanying drop in PLT2 protein levels occurring at 36 hpg in the distal meristematic cells induces cell differentiation, thus determining TZ appearance.

The Initial Steps of Meristem Growth Depend on an ARR12/PLT/Auxin Network

We next asked whether the drop of PLT2 at the TZ could be responsible for ARR12 activation at 36 hpg. ARR12 is not a direct target of the PLT factors, as revealed by chromatin immunoprecipitation sequencing (ChIP-seq) and micro-array datasets (Santuari et al., 2016). Still, upon short dexamethasone induction of *35S:PLT2:GR*, ARR12 expression in roots was rapidly inhibited as revealed by real-time qPCR experiments (Figure 4A). Furthermore, ARR12 expression in the *plt1,plt2* double mutant was anticipated at 24 hpg while, at later developmental stages, it expands into the meristem as suggested by the analysis of a *ARR12:GUS* construct in this double mutant (Figures 5B and S4A–S4C). Thus PLT2 represses ARR12 and, at 36 hpg when the levels of PLT2 locally decrease, ARR12 expression appears in the incipient TZ.

To understand the functional significance of ARR12 activation following the drop of PLTs at this early stage of root development, we analyzed TZ establishment in the *arr12* mutant. Interestingly, the TZ in this mutant at 40 hpg was present but at an increased distance from the root tip resulting in an increased number of meristematic cells (Figures 5C and 5D). Thus, ARR12 is not causal for TZ establishment *per se* but does impact its precise position during these initial steps of root meristem development. This is in accordance with previous observations showing that cytokinin controls TZ position and the differentiation rate of meristematic cells, thus controlling root meristem size (Moubayidin et al., 2010; Perilli et al., 2013).

To understand how the ARR12 transcription factor controls TZ position and root meristem growth dynamics, we performed a ChIP-seq using a fully complementing *ARR12:GFP* protein fusion.

We mapped 587 peaks (irreproducible discovery rate < 0.01) in the *ARR12:GFP* samples compared with the *Col-0* (NCBI GEO: GSE134695; Table S1). Consistent with ARR12 role as a transcription factor, these peaks mainly mapped to promoter regions (~50% 1 kb upstream transcription start site (TSS), ~20% 1–2 kb upstream TSS) (Figure S4D). We identified that the bound sites were enriched for the canonical ARR-B consensus sequence (5′-(A/G)GAT(C/T)T- 3′), supporting the success of the ChIP-seqs (Hosoda et al., 2002) (Figure S4E). ARR12 positively controls several key genes involved in root development, such as *SHY2* (*SHORT HYPOCOTYL 2)* and *GH3.17* (*GRETCHEN HAGEN 3.17*) previously identified as targets of ARR1 (Dello Ioio et al., 2008; Di Mambro et al., 2017; Moubayidin et al., 2010) (Figures S4F, S4G, and S4J; Table S1). More notably, we observed that ARR12 binds in the proximity of the *PLT2* transcription start site (Figure 5E). An independent ChIP experiment coupled to a real-time qPCR, revealed that the ARR12 protein directly binds to the PLT2 promoter (Figures 5E and 5F). To understand the effect of ARR12 on *PLT2*, we monitored *PLT2* expression in the *arr12*-1 mutant using a *pPLT2:CFP* transcriptional fusion (Galinha et al., 2007). Notably, *PLT2* levels are increased in the *arr12*-1 mutant, suggesting an inhibitory effect of ARR12 on *PLT2* expression (Figures S4H and S4I). These data were confirmed by real-time qPCR experiments monitoring *PLT2* mRNA levels in the *arr12*-1 mutants (Figure 5G). Furthermore, in agreement with these observations, PLT2 protein gradients in the *arr12*-1 mutants expand to the shootward region of the proliferation zone as revealed by the analysis of *PLT2:YFP* constructs in this mutant (Figures 4H and 4I). Interestingly ARR12 also inhibits expression of the *PLT1* gene as revealed by qRT-PCR experiments in the *arr12-1* mutant (Figure S4K). Hence, ARR12 confines the *PLT2* transcription domains to the stem cell niche, thus controlling the PLT2 protein domain in the TZ and thereby contributing to TZ establishment at early stages of root development.

To analyze the dynamics of the initial steps of root growth, we incorporated in the model both the ARR12-dependent SHY2-mediated reduction of *PIN* levels (Moubayidin et al., 2010), the ARR12-dependent GH3.17-mediated auxin degradation, as well as the PLTs-ARR12 mutual inhibition (STAR Methods, Step 3).

Upon incorporating these interactions, our model could successfully explain the ARR12 absence prior to 36 hpg but failed to correctly reproduce the confined, TZ-localized ARR12 expression pattern at 36 hpg and later (Figure 6A, right). In particular, the model revealed that for cell files with lower PLT expression, such as the cortex, ARR12 expression penetrates further rootward into the meristem, which is not observed in root of *ARR12:GUS* seedlings (Figure 2B). We then reasoned that a positive impact of auxin on ARR12 might be needed. In this way, lower auxin levels would not only lead to less PLT induction

Please cite this article in press as: Salvi et al., A Self-Organized PLT/Auxin/ARR-B Network Controls the Dynamics of Root Zonation Development in *Arabidopsis thaliana*, Developmental Cell (2020), https://doi.org/10.1016/j.devcel.2020.04.004

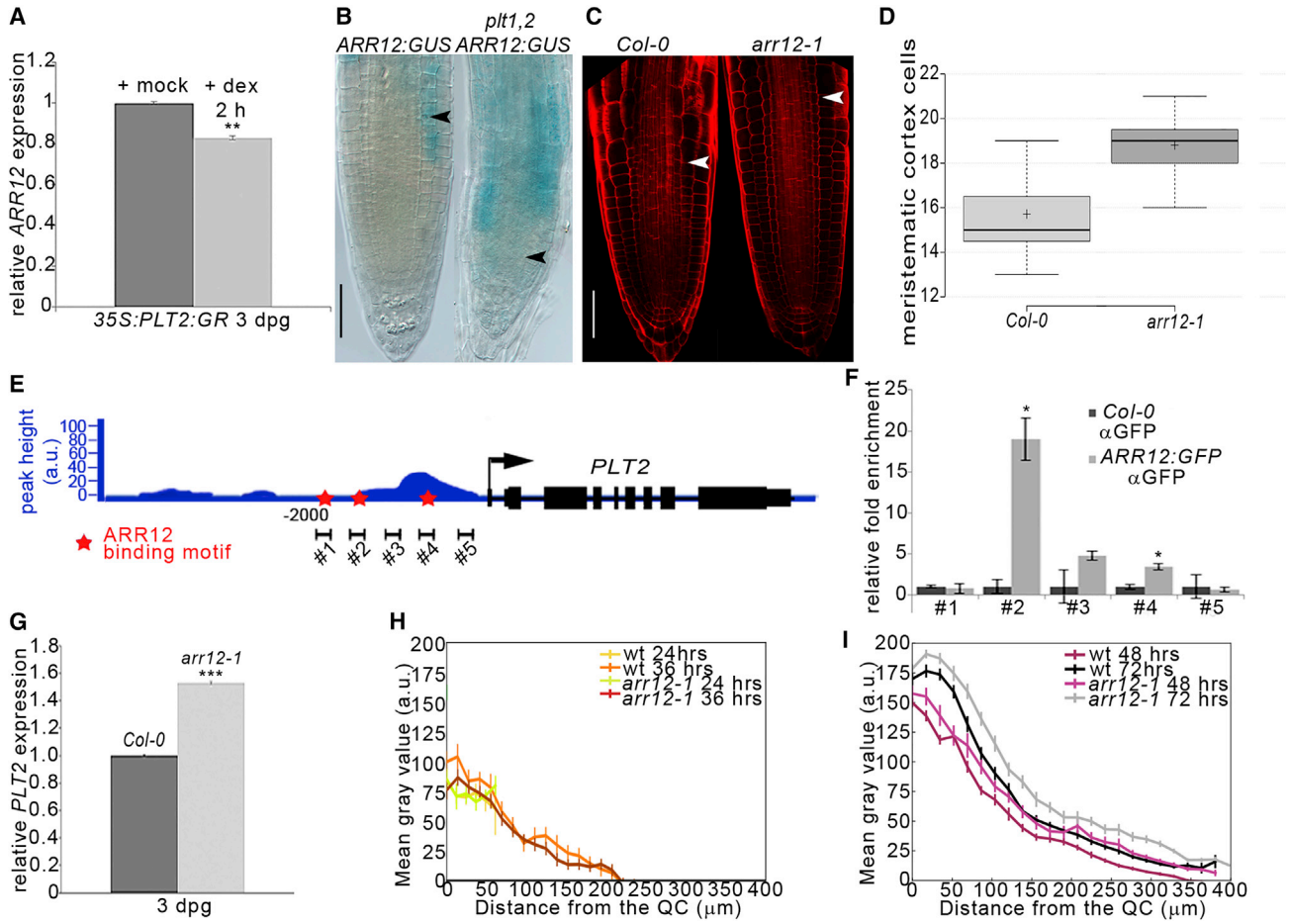

Figure 5. Initial Meristem Growth Depends on a Reciprocal ARR12/PLTs Inhibition

(A) Real-time PCR analysis of *ARR12* mRNA levels in 3 dpg old *35S:PLT2:GR* root tips upon mock and dexamethasone treatments for 2 h. Error bars represent the SE; **p < 0.001 Student's t test; two technical replicates were performed on two independent biological replicates.

(B) DIC microscopy image of the histochemical GUS assay detecting *ARR12:GUS* localization at 60 hpg in a wild-type root meristem and in a *plt1,2* mutant background (n = 20). The black arrowheads point the cortex TZ. Scale bars represent 50 μm.

(C) Confocal microscopy images of WT and *arr12-1* root meristems at 40 hpg. White arrowheads indicate the cortex TZ. Scale bars represent 50 μm.

(D) Box plot representing the number of meristematic cortex cells in a wild type (Col-0) and *arr12-1* at 40 hpg. (n = 20) (p < 0.001 Student's t test).

(E) Schematic overview of the *PLT2* gene (AT1G51190) and the −2,000 bases upstream of the *PLT2* TSS altogether with the sequencing peak annotations (in blue) of one out of two ChIP sequencing biological replica as visualized in the Integrated Genome Browser. Black squared brackets indicate the approximate genomic pairing position for the oligonucleotides used in the ChIP-qPCR experiment of (F). Red stars indicate the approximate positions of ARR12 consensus binding sites (see Figure S4). The black arrow marks the TSS of the *PLT2* gene.

(F) ChIP-qPCR analyses of *PLT2* fold enrichment relative to *ACT2* (used as negative control) performed on an independent immunoprecipitated chromatin assays (ChIP) of *ARR12:GFP* and *Col-0* roots. Columns indicate mean values, error bars represent the SE. (*p < 0.01; Student's t test; two technical replicates performed on two independent ChIPped-DNA batches).

(G) Real-time PCR analysis of *PLT2* mRNA levels in 3 dpg old *Col-0* and *arr12-1* root tips. Error bars represent the SE; ***p < 0.0001 Student's t test; two technical replicates were performed on two independent biological replicates.

(H) Quantification of the *PLT2:YFP* fluorescence along the epidermal tissue of *arr12-1* and *Col-0* root meristem at 24 and 36 hpg. Mean gray values (y axis; a.u.) are shown in function of the distance from the QC (x axis, μm). *arr12-1* is not significantly increased from wild type (*Col-0*) at 24 and 36 hpg (n = 10; Student's t test: p > 0.2; error bars represent the SE; note that the wild type is the same as in Figure 4A).

(I) Quantification of the *PLT2:YFP* fluorescence along the epidermal tissue of *arr12-1* and *Col-0* root meristem at 48 and 72 hpg. Mean gray values (y axis; a.u.) are shown as a function of the distance from the QC (x axis, μm). Wild type (*Col-0*) is significantly different from *arr12-1* at both 48 and 72 hpg (n = 10; Student's t test comparison of SCN PLT levels, p < 0.05 and p < 0.005, respectively; error bars represent the SE; note that the wild type is the same as in Figure 4A).

See also Figure S4 and Table S1.

and hence less ARR12 repression but also to less ARR12 induction. Incorporation of the auxin dependence of ARR12 induction into the model resulted in a more confined and homogeneous ARR12 localization (Figure 6A, left). Thus, our model predicted that ARR12 should be auxin inducible. In fact, ARR12 is rapidly induced by auxin as revealed by experiments where roots of plants carrying an *ARR12:GUS* construct were exposed to exogenous auxin applications (Figure 6B). In *pWOX5:IAAH* plants, where additional auxin is produced in the QC (Blilou et al., 2005), *ARR12:GUS* expression increases only at the TZ although

Please cite this article in press as: Salvi et al., A Self-Organized PLT/Auxin/ARR-B Network Controls the Dynamics of Root Zonation Development in *Arabidopsis thaliana*, Developmental Cell (2020), https://doi.org/10.1016/j.devcel.2020.04.004

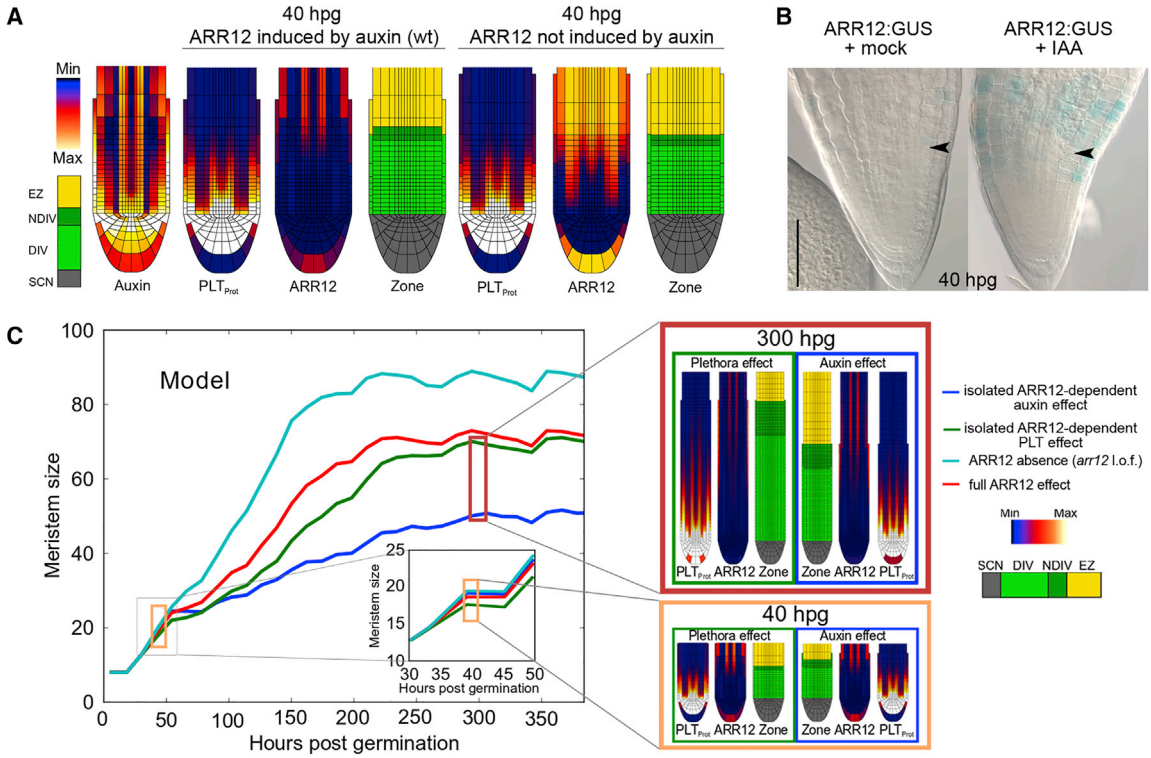

Figure 6. Exploration of ARR12 Regulation and Its Effects on Meristem Size over Time

(A) Model auxin, PLT protein, ARR12 expression and developmental zonation patterns at 40 hpg in default wild-type model settings incorporating auxin-dependent ARR12 induction (left) and alternative model settings in which ARR12 is auxin-independent (right).

(B) DIC microscopy image of histochemical GUS assay detecting *ARR12:GUS* expression at 40 hpg upon mock and indole-3-acetic acid (IAA, 5μM for 6 h) treatments (n = 20; consistent with the results shown in the figure throughout 85% of *ARR12:GUS* + mock roots and throughout 60% *ARR12:GUS* + IAA 5μM samples). The black arrowheads point to the incipient cortex TZ. Scale bar represents 50 μm.

(C) Model comparison between early (inset, orange box) and late (full graph, dark red box) effects of the auxin-repressing and PLT-repressing regulatory effects of ARR12. Blue: alternative ARR12 model setting where ARR12 only represses auxin, but this effect is enhanced. Green: alternative ARR12 model setting where ARR12 only represses PLT, but this effect is enhanced. Cyan: ARR12 knockout. Red: wild-type ARR12 settings with intermediate auxin and PLT inhibition. PLT inhibition shows a stronger effect at 40 hpg (orange box) while Auxin inhibition shows a stronger effect on final meristem size (dark red box).

See also Figure S5.

the stem cell niche has the competence to express *ARR12:GUS* (Figure S5D), corroborating our hypothesis that PLTs repress ARR12 in the stem cell niche. Thus, the concomitant auxin induction and PLT suppression of ARR12 confine its expression and activities to the TZ.

To understand the dynamics of ARR12 control of TZ positioning, we sought to dissect the relative impact of ARR12 direct control on *PLT2*, versus the ARR12 direct control on *SHY2* and *GH3.17*. This question is impossible to answer experimentally, but can be addressed using our model. To achieve this, we made two model variants, one in which ARR12 positively controls only the *SHY2* and *GH3.17* gene expressions, thus antagonizing auxin, and one in which it only antagonizes PLTs. We enhanced the strengths of these interactions to compensate for the absence of the other antagonism (Video S1). We compared simulated meristem dynamics for these model variants with a wild-type meristem (where ARR12 controls the *SHY2*, the *GH3.17*, and the *PLT* genes) and with a ARR12 loss-of-function meristem (where ARR12 does not control the *SHY2*, the *GH3.17*, and *PLT* genes) (Figure 6C). We found that at early stages of development, again, due to the slow auxin-dependent induction of *PLTs* (Mähönen et al., 2014), when ARR12 only affects the *SHY2* and the *GH3.17* genes, it is insufficient to affect *PLT* activities and TZ positioning (Figure 6C). On the contrary, direct dampening of *PLT2* activities exerted by ARR12 enables a prompter effect on TZ positioning (Figure 6C). The ARR12-dependent control of the *SHY2* and the *GH3.17* genes significantly affects TZ position only at later stages of meristem development when growth of the meristem increases the distance between the *ARR12* and the *PLT* expression domains (Figure 6C). Thus, ARR12 initially controls TZ position mainly by repressing *PLT2* transcription whereas the ARR12-dependent *SHY2* and *GH3.17* control of TZ positioning increases in importance over time.

Root Meristem Stabilization at 5 dpg Depends on a ARR1/PLT/KRP2/Auxin Network

Although the auxin, PLT, and ARR12 dynamics described so far can account for the establishment and positioning of the TZ at initial stages of root development, they cannot explain the stabilization of TZ position and meristem size occurring at 5 dpg (Dello Ioio et al., 2008; Di Mambro et al., 2017). Indeed, if we continued simulations with the model incorporating the auxin/PLT/ARR12

Please cite this article in press as: Salvi et al., A Self-Organized PLT/Auxin/ARR-B Network Controls the Dynamics of Root Zonation Development in *Arabidopsis thaliana*, Developmental Cell (2020), https://doi.org/10.1016/j.devcel.2020.04.004

CellPress

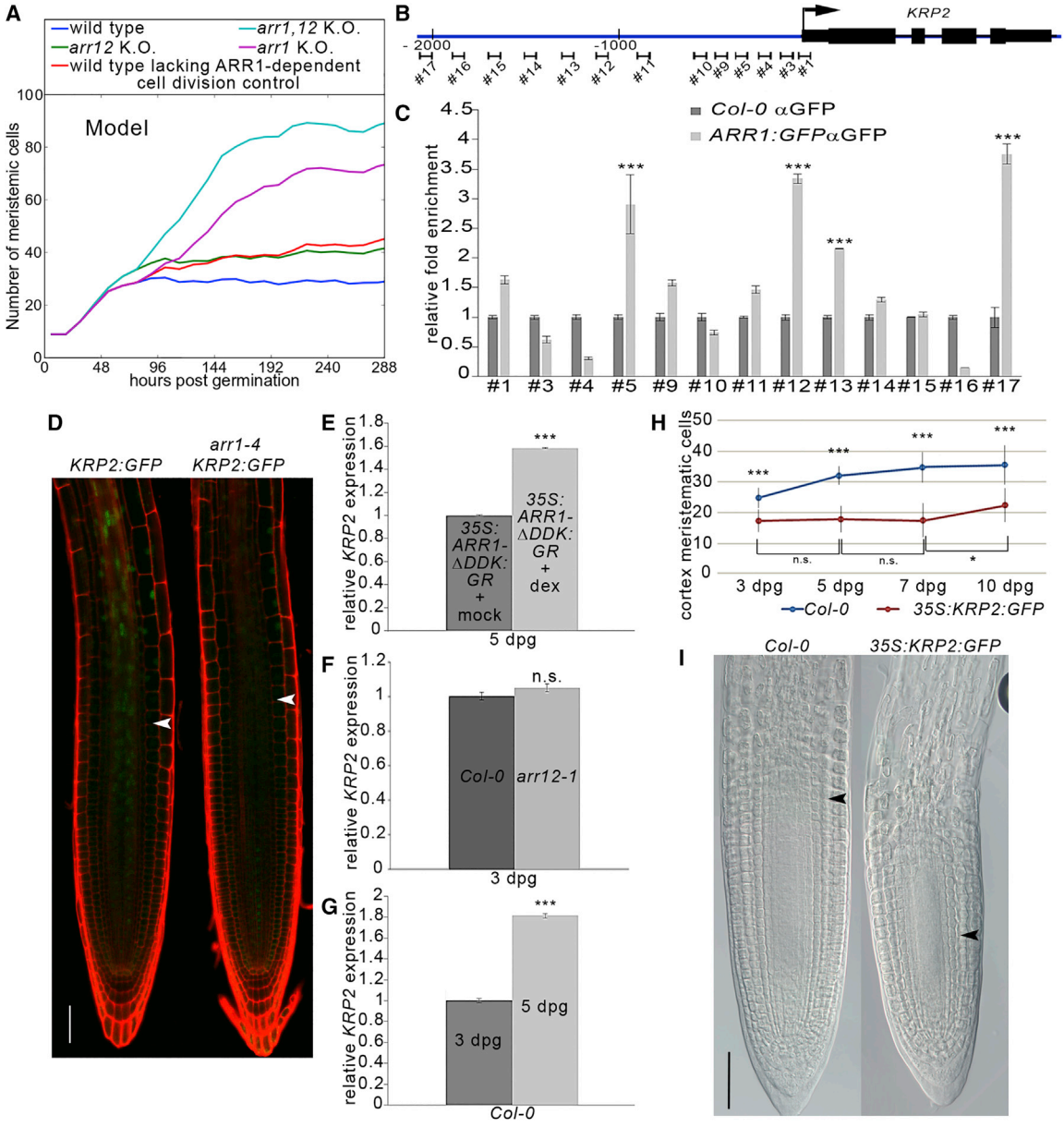

Figure 7. Root Meristem Stabilization at 5 dpg Depends on an ARR1-Dependent Control of Cell Division through the Regulation of KRP2 Expression

(A) Simulated wild type (blue), *arr1*(purple), *arr12*(green), *arr1,arr12*(cyan), and a hypothetical mutant where ARR1 only lacks its KRP2-mediated repression on cell divisions (red). The dynamics of the simulated knockout mutants match their experimental counterparts (see Moubayidin et al., 2010; Figure 2Q). KRP2 function is required for ARR1 to halt meristem growth at 5 dpg (Video S3).

(B) Schematic overview of the *KRP2* gene (AT3G50630) and the −2000 bases upstream of the *KRP2* TSS. Below the scheme, black squared brackets indicate pairing positions of the 13 oligonucleotides used in the ChIP-qPCR experiment in (C). The black arrow marks the TSS of the *KRP2* gene.

(C) ChIP-qPCR analyses of *KRP2* fold enrichment relative to the negative control (*ACT2*) performed on independent immunoprecipitated chromatin assays (ChIP) of *ARR12:GFP* and *Col-0* roots. Columns show mean values, error bars represent the SE (***$p < 0.0001$; Student's t test; two technical replicates performed on two independent ChIPped-DNA batches).

(D) Confocal microscopy images of *KRP2:GFP* and *arr1-4 KRP2:GFP* root meristems at 5 dpg. White arrowheads indicate the cortex TZ. Scale bars represent 50 μm.

(E) Real-time PCR analysis of *KRP2* mRNA levels in 5 dpg old *35S:ARR1-ΔDDK:GR* root tips upon mock and 10 μM dexamethasone treatments for 2 h. Error bars represent the SE; ***$p < 0.0001$ Student's t test; two technical replicates were performed on independent biological replicates.

(F) Real-time PCR analysis of *KRP2* mRNA levels in wild-type (*Col-0*) root tips at 3 and 5 dpg. Error bars represent the SE; n.s., not significant Student's t test; two technical replicates were performed on two independent biological replicates.

(G) Real-time PCR analysis of *KRP2* mRNA levels in wild-type (*Col-0*) root tips and *arr12-1* at 3 dpg. Error bars represent SE; ***$p < 0.0001$ Student's t test; two technical replicates were performed on two independent biological replicates.

(legend continued on next page)

Please cite this article in press as: Salvi et al., A Self-Organized PLT/Auxin/ARR-B Network Controls the Dynamics of Root Zonation Development in *Arabidopsis thaliana*, Developmental Cell (2020), https://doi.org/10.1016/j.devcel.2020.04.004

module for a longer developmental time window (over 5 dpg), a large and very slowly stabilizing meristem arises, differing in size only slightly from a meristem established in the absence of ARRs (Figure 6C, right red versus cyan lines). Thus, while ARR12 exerts sufficient antagonism to impact TZ position as early as 36 hpg, another factor is required to explain meristem stabilization.

We have previously shown that another cytokinin-dependent gene, *ARR1*, is involved in stabilizing the position of the TZ and meristem size at 5 dpg (Dello Ioio et al., 2008). Unlike *ARR12*, the *ARR1* gene is expressed at later stages of meristem development (around 5 dpg) coinciding with the time of meristem growth stabilization (Dello Ioio et al., 2008; Moubayidin et al., 2010). Indeed, analysis of the root meristems of two different *arr12* mutant alleles revealed that while they were already larger than wild type at 3 dpg, they stopped growing after reaching an increased but fixed number of cells at 5 dpg (Dello Ioio et al., 2007). In contrast, the root meristems of three different *arr1* mutant alleles, in line with the delayed expression pattern of this gene, were indistinguishable from the wild type up to 5 dpg but became significantly larger from 5 dpg onward and kept increasing in size thereafter (Dello Ioio et al., 2007).

ARR1, as *ARR12*, is induced by auxin (Figures 6A and 6B) (Moubayidin et al., 2013), but the ARR1 ChIP-on-chip dataset indicates that this transcription factor, differently from ARR12, does not directly repress *PLT2* expression (Di Mambro et al., 2017).

We therefore hypothesized that, since PLT gradient expansion strongly depends on cell division, ARR1 may instead negatively affect cell division to stabilize TZ position. To investigate this hypothesis, we extended our model with ARR1. Like ARR12, we incorporated auxin-dependent induction and PLT-dependent repression of ARR1, as well as the induction of *SHY2* and *GH3.17* by ARR1 (Dello Ioio et al., 2008; Di Mambro et al., 2017). Uniquely for ARR1, we incorporated an ARR1-dependent repression of cell division (Video S2). The model shows that while this cell division repression effect has only a limited effect on meristem size, it does strongly enhance meristem stabilization (Figure 7A, compare blue, red, and cyan lines; Video S3). Thus, the model suggests that direct repression of cell division mediated by ARR1 but not by ARR12 could serve as the mechanism through which ARR1 stabilizes TZ position, thereby setting meristem size.

To identify factors specifically controlled by ARR1 that could be responsible for meristem stabilization, we compared an *ARR1:GFP* ChIP-on-chip dataset (GEO: GSE70595; Di Mambro et al., 2017), with the *ARR12:GFP* ChIP-seq dataset. We focused on genes involved in controlling cell division and regulated by ARR1 but not by ARR12. We found 75 matches in common, 481 genes presumably direct targets of ARR12 only, and 358 genes presumably direct targets of ARR1 only (http://bioinfogp.cnb.csic.es/tools/venny/index.html) (Figure S6A). Notably, among the latter the only gene involved in cell-cycle control is the *CYCLIN-DEPENDENT KINASE INHIBITOR2* (*KRP2*), which is known to inhibit specifically the CYCD2-1/CDKA-1 complex kinase activity, blocking the transition from the G1 to the S phase of the mitotic cycle. Thus, *KRP2* could be the target gene through which ARR1 stabilizes TZ position and meristem size at 5 dpg.

We first confirmed that *KRP2* is a direct target of ARR1 by a ChIP experiment coupled to a real-time qPCR (Figure 7B). Notably, KRP2 is expressed at the TZ in a domain covering that of ARR1, as revealed by the analysis of the root meristems of plants carrying a *KRP2:GFP* construct (Sanz et al., 2011). *KRP2* is positively controlled by ARR1, as in the *arr1-4* mutant background *KRP2* mRNA and protein levels are lower than the wild type as revealed by real-time qPCR experiments and *KRP2:GFP* expression analysis, respectively (Figures 7D and S6B). Furthermore, upon dexamethasone treatments of plant carrying a *35S:ARR1-ΔDDK:GR* construct, real-time qPCR experiments showed higher *KRP2* mRNA levels (Figure 7E). As expected, *KRP2* is not controlled by ARR12 as shown by real-time qPCR analysis of *KRP2* mRNA levels in the *arr12-1* mutant background (Figure 7F).

Next, we examined if a KPR2 increment, triggered by ARR1 at 5 dpg, is indeed able to stabilize the meristem as predicted by the model. First, we monitored its expression over time during meristem development. As expected, *KRP2* expression increases in time, being lower at 3 dpg when the meristem is still growing and increasing at 5 dpg when meristem size is stabilized (Figure 7G). Finally, to understand if the ARR1-dependent *KRP2* increment at 5 dpg results in TZ stabilization and meristem size determination, we anticipated KRP2 expression at early stages of root meristem development by means of a *35S:KRP2:GFP* (Sanz et al., 2011) and a *RCH2>>KRP2 (RCH2:GAL4 x UAS:KRP2:CFP)* construct. In both cases, the root meristems of *35S:KRP2:GFP* and *RCH2>>KRP2* plants display shorter roots with meristems that set their size before 5 dpg in accordance with the anticipated higher level of KRP2 at the TZ (Figures 7H, 7I, S6C, and S6D). Thus, at 5 dpg ARR1 activity results in a *KRP2* increment that, by slowing down cell division, sets the position of TZ and determines meristem size.

DISCUSSION

Understanding organ growth dynamics is a central question in developmental biology. In particular, major questions involve how organs are enabled to expand and subsequently are ensured to stabilize when reaching a functional size. Here, by using an interdisciplinary approach combining molecular genetics with computational modeling, we identify a minimal molecular network that dynamically controls the development of the root meristem from seed germination onward. We show that an ARR12/PLT/auxin network is responsible for controlled root meristem expansion during early development while an ARR1/KRP2/PLT/auxin network determines meristem size and TZ stabilization at later developmental stages thus setting the final rate of root growth. Additionally, we illustrate how these networks rely on and interact with cellular growth processes to enable a continuous re-patterning of the TZ position.

(H) Plot of meristematic cortex cells measured at 3-, 5-, 7-, and 9-dpg-old wild type (*Col-0*) and in *35S:KRP2:GFP* roots. (*$p < 0.01$, ***$p < 0.0001$, and n.s., not significant Student's t test; representative results from one out of two independent biological replicates performed).
(I) DIC microscopy images of 5 dpg old *Col-0* and *35S:KRP2:GFP* root meristems (n = 20). Black arrowheads indicate the cortex TZ. Scale bars represent 50 μm. See also Figure S6.

Please cite this article in press as: Salvi et al., A Self-Organized PLT/Auxin/ARR-B Network Controls the Dynamics of Root Zonation Development in *Arabidopsis thaliana*, Developmental Cell (2020), https://doi.org/10.1016/j.devcel.2020.04.004

We show that, upon seed germination, cell division starts at 24 hpg with a PLT gradient formed at 36 hpg. Modeling the previously identified cell-division-induced PLT dilution (Mähönen et al., 2014) demonstrates that it is sufficient for PLT2 gradient formation at 36 hpg (Figure 4B). Recently, degradation of PLT proteins was shown to refine the PLT gradient (Matsuzaki et al., 2010; Yamada et al., 2020), yet whether this degradation is active at early developmental stages remains to be investigated. Our data also demonstrate that the resulting drop in PLT levels is sufficient to trigger cell differentiation, thereby establishing the TZ and enabling activation of ARR12 that antagonizes the PLT1/PLT2 genes. The mutual ARR12-PLTs inhibition constrains the PLT expression domains to the stem cell niche while positioning ARR12 shootward of the TZ. At slightly later stages, the SHY2- and GH3.17-dependent ARR12-auxin antagonism has had sufficient time to affect PLT levels and further contributes to TZ positioning. While the auxin-ARR12-PLT network controls TZ positioning, we show that another network consisting of ARR1/KRP2/auxin is essential for meristem size stabilization at 5dpg when the decrease in concentration of another hormone, gibberellin, de-represses ARR1 expression (Moubayidin et al., 2010). ARR1, but not ARR12, directly activates *KRP2*, inhibiting cell division. This inhibition allows ARR1 to limit the division-dependent expansion of the PLT gradient, enabling meristem size stabilization.

We recently showed that cytokinin controls meristem size and root growth also by directly promoting cell expansion processes, by activating the expression of α-EXPANSINs (EXPAs) (Pacifici et al., 2018). Thus, cytokinin directly promotes cell differentiation by activating the EXPA proteins (Pacifici et al., 2018) and represses cell division by activating the *KRP2* gene (this paper). This indicates that the transition from division to differentiation does not merely involve the cytokinin-induced repression of division stimulating signals (auxin and PLTs) but instead also involves the active induction of differentiation and repression of cell division. Analogously, during mouse smooth muscle terminal differentiation, the MyoD skeletal-muscle-specific transcription factor coordinates cell differentiation by directly activating at the same time the expression of pro-differentiating factors and the expression of cell-cycle inhibitors, such as the cyclin-dependent kinase inhibitors (CKI) $p21^{Cip1}$ and $p57^{Kip2}$, that exert the same function as KRP2 (Halevy et al., 1995; Ruijtenberg and van den Heuvel, 2016; Zhang et al., 1999).

Our proposed regulatory network provides an elegant explanation for how division and differentiation activities are positioned in the developing root. As cells divide and move away from the root tip, cell division induces PLT protein dilution enabling the most shootward localized meristematic cells to switch from a division to an elongation state (Mähönen et al., 2014, this paper). This transition is enhanced through the activation of, first, ARR12 and, at later stages, ARR1, resulting in the continuous dynamic re-patterning of new cells transiting from the meristem into the elongation/differentiation zone (this paper). The TZ, where this transition occurs, becomes stably positioned at 5 dpg when ARR1 is activated. At this stage, both ARR12 and ARR1 are active, increasing SHY2 and GH3.17 expression, that in turn impact auxin homeostasis, thereby reducing PLT levels (Dello Ioio et al., 2008; Di Mambro et al., 2017). Furthermore, ARR1 represses cell division via KRP2 and, hence, the spread of the PLT2 protein. The combined effects of the ARR1-mediated auxin and cell division antagonism strongly constrain the extent of the PLT gradient, setting the position of the TZ.

Finally, we discovered that the proper positioning of the ARR12 expression domain arises not only from its mutual antagonism with PLTs but also requires that ARR12 expression is auxin dependent. Since auxin induces ARR-Bs whereas it suppresses ARR-Bs in the meristem by inducing PLTs, ARR-B expression is possible only at the transition and elongation zone. Thus, two domains arise: the meristem, where high auxin levels co-occur with the PLTs, and the elongation zone, where high auxin levels co-occur with the ARR-Bs. In this scenario the auxin/PLT/ARR-B interaction network is a self-organized pattern generator in which auxin generates distinct PLT and ARR-B domains that enable auxin to control different processes in different contexts as well as to control the size of these domains.

STAR★METHODS

Detailed methods are provided in the online version of this paper and include the following:

- KEY RESOURCES TABLE
- RESOURCE AVAILABILITY
  - Lead Contact
  - Materials Availability
  - Data and Code Availability
- EXPERIMENTAL MODEL AND SUBJECT DETAILS
  - Plant Growth Conditions
- METHOD DETAILS
  - Experiments
  - Computational Model
  - Additional PLT Dynamics
  - Initial Conditions
  - Model Construction and Parametrization
  - Step 1: An Auxin-PLT Model Simulating the arr1,arr12 Double Mutant
  - Step 2: Tuning Initial Conditions
  - Step 3: An Auxin-PLT-ARR12 Model Simulating the arr1 Mutant
  - Step 4: The Auxin-PLT-ARR12-ARR1 Model Simulating the Wildtype
  - Alternative Model Settings
  - Model Code and Simulation
- QUANTIFICATION AND STATISTICAL ANALYSIS

SUPPLEMENTAL INFORMATION

Supplemental Information can be found online at https://doi.org/10.1016/j.devcel.2020.04.004.

ACKNOWLEDGMENTS

We thank Noemi Svolacchia, Gaia Bertolotti, Emanuela Pierdonati, and Elena Pacifici for technical support and Thea van den Berg for reading the manuscript and helpful discussions. We also thank Renze Heidstra, Ari Pekka Mähönen, Lieven De Veylder, and Walter Dewitte for providing material. The ChIP-seq data have been deposited in the NCBI Gene Expression Omnibus under GEO: GSE134695. This work was supported by the European Research Council grant number 260368 (to S.S. and E.S.), the Company of Biologists

Limited grant number DEVTF-170510 (to E.S.), and the NWO (Dutch Organization for Scientific Research) grant number 864.14.009 (to J.R. and K.T.T.).

AUTHOR CONTRIBUTIONS

E.S. planned and performed the experiments, J.R. planned and performed the simulations, K.T.T. and J.R. developed the code for the simulations, E.S., R.D.M., L.P., and R.D.I. cloned the genes, R.N. and V.L. performed bioinformatics analysis of ChIP-seq results and discussed the experiments, J.R., E.S., K.T.T., and S.S. discussed and interpreted all results and wrote the manuscript, S.S. and K.T.T. conceived the research.

DECLARATION OF INTERESTS

The authors declare no competing interests.

Received: December 13, 2019
Revised: February 20, 2020
Accepted: April 6, 2020
Published: May 7, 2020

WEB RESOURCES

Venny 2.1, https://bioinfogp.cnb.csic.es/tools/venny/index.html

REFERENCES

Aida, M., Beis, D., Heidstra, R., Willemsen, V., Blilou, I., Galinha, C., Nussaume, L., Noh, Y.S., Amasino, R., and Scheres, B. (2004). The PLETHORA genes mediate patterning of the Arabidopsis root stem cell niche. Cell *119*, 109–120.

Band, L.R., Wells, D.M., Fozard, J.A., Ghetiu, T., French, A.P., Pound, M.P., Wilson, M.H., Yu, L., Li, W., Hijazi, H.I., et al. (2014). Systems analysis of auxin transport in the Arabidopsis root apex. Plant Cell *26*, 862–875.

Blilou, I., Xu, J., Wildwater, M., Willemsen, V., Paponov, I., Friml, J., Heidstra, R., Aida, M., Palme, K., and Scheres, B. (2005). The PIN auxin efflux facilitator network controls growth and patterning in Arabidopsis roots. Nature *433*, 39–44.

Boudonck, K., Dolan, L., and Shaw, P.J. (1998). Coiled body numbers in the Arabidopsis root epidermis are regulated by cell type, developmental stage and cell cycle parameters. J. Cell Sci. *111*, 3687–3694.

Brumfield, R.T. (1942). Cell growth and division in living root meristems. Am. J. Bot. *29*, 533–543.

Burch-Smith, T.M., Stonebloom, S., Xu, M., and Zambryski, P.C. (2011). Plasmodesmata during development: re-examination of the importance of primary, secondary, and branched plasmodesmata structure versus function. Protoplasma *248*, 61–74.

Casamitjana-Martínez, E., Hofhuis, H.F., Xu, J., Liu, C.M., Heidstra, R., and Scheres, B. (2003). Root-specific CLE19 overexpression and the sol1/2 suppressors implicate a CLV-like pathway in the control of Arabidopsis root meristem maintenance. Curr. Biol. *13*, 1435–1441.

Curaba, J., Moritz, T., Blervaque, R., Parcy, F., Raz, V., Herzog, M., and Vachon, G. (2004). AtGA3ox2, a key gene responsible for bioactive gibberellin biosynthesis, is regulated during embryogenesis by LEAFY COTYLEDON2 and FUSCA3 in Arabidopsis. Plant Physiol. *136*, 3660–3669.

Dello Ioio, R., Linhares, F.S., Scacchi, E., Casamitjana-Martinez, E., Heidstra, R., Costantino, P., and Sabatini, S. (2007). Cytokinins determine Arabidopsis root-meristem size by controlling cell differentiation. Curr. Biol. *17*, 678–682.

Dello Ioio, R., Nakamura, K., Moubayidin, L., Perilli, S., Taniguchi, M., Morita, M.T., Aoyama, T., Costantino, P., and Sabatini, S. (2008). A genetic framework for the control of cell division and differentiation in the root meristem. Science *322*, 1380–1384.

Di Mambro, R., Svolacchia, N., Dello Ioio, R., Pierdonati, E., Salvi, E., Pedrazzini, E., Vitale, A., Perilli, S., Sozzani, R., Benfey, P.N., et al. (2019). The lateral root cap acts as an auxin sink that controls meristem size. Curr. Biol. *29*, 1199–1205.

Di Mambro, R., De Ruvo, M., Pacifici, E., Salvi, E., Sozzani, R., Benfey, P.N., Busch, W., Novak, O., Ljung, K., Di Paola, L., et al. (2017). Auxin minimum triggers the developmental switch from cell division to cell differentiation in the Arabidopsis root. Proc. Natl. Acad. Sci. USA *114*, E7641–E7649.

Di Mambro, R., and Sabatini, S. (2018). Developmental analysis of Arabidopsis Root meristem. In Root Development: Methods and Protocols, D. Ristova and E. Barbez, eds. (Springer), pp. 33–45.

Farcot, E., Lavedrine, C., and Vernoux, T. (2015). A modular analysis of the auxin signalling network. PLoS One *10*, e0122231.

Galinha, C., Hofhuis, H., Luijten, M., Willemsen, V., Blilou, I., Heidstra, R., and Scheres, B. (2007). PLETHORA proteins as dose-dependent master regulators of Arabidopsis root development. Nature *449*, 1053–1057.

Grieneisen, V.A., Xu, J., Marée, A.F.M., Hogeweg, P., and Scheres, B. (2007). Auxin transport is sufficient to generate a maximum and gradient guiding root growth. Nature *449*, 1008–1013.

Guilfoyle, T.J. (2015). The PB1 domain in auxin response factor and aux/IAA proteins: A versatile protein interaction module in the auxin response. Plant Cell *27*, 33–43.

Halevy, O., Novitch, B.G., Spicer, D.B., Skapek, S.X., Rhee, J., Hannon, G.J., Beach, D., and Lassar, A.B. (1995). Correlation of terminal cell cycle arrest of skeletal muscle with induction of p21 by MyoD. Science *267*, 1018–1021.

Hosoda, K., Imamura, A., Katoh, E., Hatta, T., Tachiki, M., Yamada, H., Mizuno, T., and Yamazaki, T. (2002). Molecular structure of the GARP family of plant Myb-related DNA binding motifs of the Arabidopsis response regulators. Plant Cell *14*, 2015–2029.

Kim, J., Harter, K., and Theologis, A. (1997). Protein–protein interactions among the Aux/IAA proteins. Proc. Natl. Acad. Sci. USA *94*, 11786–11791.

Korasick, D.A., Westfall, C.S., Lee, S.G., Nanao, M.H., Dumas, R., Hagen, G., Guilfoyle, T.J., Jez, J.M., and Strader, L.C. (2014). Molecular basis for AUXIN RESPONSE FACTOR protein interaction and the control of auxin response repression. Proc. Natl. Acad. Sci. USA *111*, 5427–5432.

Krichevsky, A., Zaltsman, A., Kozlovsky, S.V., Tian, G.W., and Citovsky, V. (2009). Regulation of root elongation by histone acetylation in Arabidopsis. J. Mol. Biol. *385*, 45–50.

Kumar Meena, M., Kumar Vishwakarma, N., Tripathi, V., and Chattopadhyay, D. (2019). CBL-interacting protein kinase 25 contributes to root meristem development. J. Exp. Bot. *70*, 133–147.

Langmead, B., Trapnell, C., Pop, M., and Salzberg, S.L. (2009). Ultrafast and memory-efficient alignment of short DNA sequences to the human genome. Genome Biol. *10*, R25.

Li, H., Handsaker, B., Wysoker, A., Fennell, T., Ruan, J., Homer, N., Marth, G., Abecasis, G., and Durbin, R.; 1000 Genome Project Data Processing Subgroup (2009). The Sequence Alignment/map format and SAMtools. Bioinformatics *25*, 2078–2079.

Liao, C.Y., Smet, W., Brunoud, G., Yoshida, S., Vernoux, T., and Weijers, D. (2015). Reporters for sensitive and quantitative measurement of auxin response. Nat. Methods *12*, 207–210.

Ljung, K., Hull, A.K., Celenza, J., Yamada, M., Estelle, M., Normanly, J., and Sandberg, G. (2005). Sites and regulation of auxin biosynthesis in Arabidopsis roots. Plant Cell *17*, 1090–1104.

Mähönen, A.P., Ten Tusscher, K., Siligato, R., Smetana, O., Díaz-Triviño, S., Salojärvi, J., Wachsman, G., Prasad, K., Heidstra, R., and Scheres, B. (2014). PLETHORA gradient formation mechanism separates auxin responses. Nature *515*, 125–129.

Maraschin, Fdos S., Memelink, J., and Offringa, R. (2009). Auxin-induced, SCF(TIR1)-mediated poly-ubiquitination marks AUX/IAA proteins for degradation. Plant J. *59*, 100–109.

Mason, M.G., Mathews, D.E., Argyros, D.A., Maxwell, B.B., Kieber, J.J., Alonso, J.M., Ecker, J.R., and Schaller, G.E. (2005). Multiple type-B response regulators mediate cytokinin signal transduction in Arabidopsis. Plant Cell *17*, 3007–3018.

Masubelele, N.H., Dewitte, W., Menges, M., Maughan, S., Collins, C., Huntley, R., Nieuwland, J., Scofield, S., and Murray, J.A.H. (2005). D-type cyclins

activate division in the root apex to promote seed germination in Arabidopsis. Proc. Natl. Acad. Sci. USA *102*, 15694–15699.

Matsuzaki, Y., Ogawa-Ohnishi, M., Mori, A., and Matsubayashi, Y. (2010). Secreted peptide signals required for maintenance of root stem cell niche in Arabidopsis. Science *329*, 1065–1067.

Miyawaki, K., Matsumoto-Kitano, M., and Kakimoto, T. (2004). Expression of cytokinin biosynthetic isopentenyltransferase genes in Arabidopsis: tissue specificity and regulation by auxin, cytokinin, and nitrate. Plant J. *37*, 128–138.

Moore, S., Zhang, X., Mudge, A., Rowe, J.H., Topping, J.F., Liu, J., and Lindsey, K. (2015). Spatiotemporal modelling of hormonal crosstalk explains the level and patterning of hormones and gene expression in Arabidopsis thaliana wild-type and mutant roots. New Phytol. *207*, 1110–1122.

Moubayidin, L., Di Mambro, R., Sozzani, R., Pacifici, E., Salvi, E., Terpstra, I., Bao, D., van Dijken, A., Dello Ioio, R., Perilli, S., et al. (2013). Spatial coordination between stem cell activity and cell differentiation in the root meristem. Dev. Cell *26*, 405–415.

Moubayidin, L., Perilli, S., Dello Ioio, R., Di Mambro, R., Costantino, P., and Sabatini, S. (2010). The rate of cell differentiation controls the Arabidopsis root meristem growth phase. Curr. Biol. *20*, 1138–1143.

Muraro, D., Larrieu, A., Lucas, M., Chopard, J., Byrne, H., Godin, C., and King, J. (2016). A multi-scale model of the interplay between cell signalling and hormone transport in specifying the root meristem of Arabidopsis thaliana. J. Theor. Biol. *404*, 182–205.

Pacifici, E., Di Mambro, R., Dello Ioio, R., Costantino, P., and Sabatini, S. (2018). Acidic cell elongation drives cell differentiation in the Arabidopsis root. EMBO J. *37*, e99134.

Peaceman, D.W., and Rachford, H.H. (1955). The numerical solution of parabolic and elliptic differential equations. J. Soc. Ind. Appl. Math. *3*, 28–41.

Perilli, S., Perez-Perez, J.M., Di Mambro, R., Peris, C.L., Díaz-Triviño, S., Del Bianco, M., Pierdonati, E., Moubayidin, L., Cruz-Ramírez, A., Costantino, P., et al. (2013). RETINOBLASTOMA-RELATED protein stimulates cell differentiation in the Arabidopsis root meristem by interacting with cytokinin signaling. Plant Cell *25*, 4469–4478.

Raines, T., Shanks, C., Cheng, C.Y., McPherson, D., Argueso, C.T., Kim, H.J., Franco-Zorrilla, J.M., López-Vidriero, I., Solano, R., Vaňková, R., et al. (2016). The cytokinin response factors modulate root and shoot growth and promote leaf senescence in Arabidopsis. Plant J. *85*, 134–147.

Rouse, D., Mackay, P., Stirnberg, P., Estelle, M., and Leyser, O. (1998). Changes in auxin response from mutations in an AUX/IAA gene. Science *279*, 1371–1373.

Ruijtenberg, S., and van den Heuvel, S. (2016). Coordinating cell proliferation and differentiation: antagonism between cell cycle regulators and cell type-specific gene expression. Cell Cycle *15*, 196–212.

Rutten, J.P., and Ten Tusscher, K. (2019). In silico roots: room for growth. Trends Plant Sci. *24*, 250–262.

Sabatini, S., Beis, D., Wolkenfelt, H., Murfett, J., Guilfoyle, T., Malamy, J., Benfey, P., Leyser, O., Bechtold, N., Weisbeek, P., and Scheres, B. (1999). An auxin-dependent distal organizer of pattern and polarity in the Arabidopsis root. Cell *99*, 463–472.

Santuari, L., Sanchez-Perez, G.F., Luijten, M., Rutjens, B., Terpstra, I., Berke, L., Gorte, M., Prasad, K., Bao, D., Timmermans-Hereijgers, J.L.P.M., et al. (2016). The PLETHORA gene regulatory network guides growth and cell differentiation in Arabidopsis roots. Plant Cell *28*, 2937–2951.

Sanz, L., Dewitte, W., Forzani, C., Patell, F., Nieuwland, J., Wen, B., Quelhas, P., De Jager, S., Titmus, C., Campilho, A., et al. (2011). The Arabidopsis D-type cyclin CYCD2;1 and the inhibitor ICK2/KRP2 modulate auxin-induced lateral root formation. Plant Cell *23*, 641–660.

Scacchi, E., Salinas, P., Gujas, B., Santuari, L., Krogan, N., Ragni, L., Berleth, T., and Hardtke, C.S. (2010). Spatio-temporal sequence of cross-regulatory events in root meristem growth. Proc. Natl. Acad. Sci. USA *107*, 22734–22739.

Scheres, B., Wolkenfelt, H., Willemsen, V., Terlouw, M., Lawson, E., Dean, C., and Weisbeek, P. (1994). Embryonic origin of the Arabidopsis primary root and root meristem initials. Development *120*, 2475–2487.

Sliwinska, E., Bassel, G.W., and Bewley, J.D. (2009). Germination of Arabidopsis thaliana seeds is not completed as a result of elongation of the radicle but of the adjacent transition zone and lower hypocotyl. J. Exp. Bot. *60*, 3587–3594.

Smetana, O., Mäkilä, R., Lyu, M., Amiryousefi, A., Sánchez Rodríguez, F., Wu, M.F., Solé-Gil, A., Leal Gavarrón, M., Siligato, R., Miyashima, S., et al. (2019). High levels of auxin signalling define the stem-cell organizer of the vascular cambium. Nature *565*, 485–489.

Sozzani, R., Cui, H., Moreno-Risueno, M.A., Busch, W., Van Norman, J.M.V., Vernoux, T., Brady, S.M., Dewitte, W., Murray, J.A., and Benfey, P.N. (2010). Spatiotemporal regulation of cell-cycle genes by SHORTROOT links patterning and growth. Nature *466*, 128–132.

Stepanova, A.N., Robertson-Hoyt, J., Yun, J., Benavente, L.M., Xie, D.Y., Doležal, K., Schlereth, A., Jürgens, G., and Alonso, J.M. (2008). TAA1-mediated auxin biosynthesis is essential for hormone crosstalk and plant development. Cell *133*, 177–191.

Takatsuka, H., Higaki, T., and Umeda, M. (2018). Actin reorganization triggers rapid cell elongation in roots. Plant Physiol. *178*, 1130–1141.

Tian, Q., Uhlir, N.J., and Reed, J.W. (2002). Arabidopsis SHY2/IAA3 inhibits auxin-regulated gene expression. Plant Cell *14*, 301–319.

Truernit, E., Bauby, H., Dubreucq, B., Grandjean, O., Runions, J., Barthélémy, J., and Palauqui, J.C. (2008). High-resolution whole-mount imaging of three-dimensional tissue organization and gene expression enables the study of phloem development and structure in Arabidopsis. Plant Cell *20*, 1494–1503.

Ubeda-Tomás, S., Federici, F., Casimiro, I., Beemster, G.T.S., Bhalerao, R., Swarup, R., Doerner, P., Haseloff, J., and Bennett, M.J. (2009). Gibberellin signaling in the endodermis controls Arabidopsis root meristem size. Curr. Biol. *19*, 1194–1199.

Ursache, R., Andersen, T.G., Marhavý, P., and Geldner, N. (2018). A protocol for combining fluorescent proteins with histological stains for diverse cell wall components. Plant J. *93*, 399–412.

van den Berg, T., Korver, R.A., Testerink, C., and ten Tusscher, K.H.W.J. (2016). Modeling halotropism: a key role for root tip architecture and reflux loop remodeling in redistributing auxin. Development *143*, 3350–3362.

Verbelen, J.P., De Cnodder, T., Le, J., Vissenberg, K., and Baluška, F. (2006). The root apex of Arabidopsis thaliana consists of four distinct zones of growth activities: meristematic zone, transition zone, fast elongation zone and growth terminating zone. Plant Signal. Behav. *1*, 296–304.

Weele, C.M. van der, Jiang, H.S., Palaniappan, K.K., Ivanov, V.B., Palaniappan, K., and Baskin, T.I. (2003). A new algorithm for computational image analysis of deformable motion at high spatial and temporal resolution applied to root growth. Roughly uniform elongation in the meristem and also, after an abrupt acceleration, in the elongation zone. Plant Physiol *132*, 1138–1148.

Wendrich, J.R., Möller, B.K., Li, S., Saiga, S., Sozzani, R., Benfey, P.N., De Rybel, B., and Weijers, D. (2017). Framework for gradual progression of cell ontogeny in the Arabidopsis root meristem. Proc. Natl. Acad. Sci. USA *114*, E8922–E8929.

Wisniewska, J., Xu, J., Seifertová, D., Brewer, P.B., Ruzicka, K., Blilou, I., Rouquié, D., Benková, E., Scheres, B., and Friml, J. (2006). Polar PIN localization directs auxin flow in plants. Science *312*, 883.

Yamada, M., Han, X., and Benfey, P.N. (2020). RGF1 controls root meristem size through ROS signalling. Nature *577*, 85–88.

Zhang, J.M., Zhao, X., Wei, Q., and Paterson, B.M. (1999). Direct inhibition of G(1) cdk kinase activity by MyoD promotes myoblast cell cycle withdrawal and terminal differentiation. EMBO J. *18*, 6983–6993.

Zhang, Y., Liu, T., Meyer, C.A., Eeckhoute, J., Johnson, D.S., Bernstein, B.E., Nusbaum, C., Myers, R.M., Brown, M., Li, W., and Liu, X.S. (2008). Model-based analysis of ChIP-Seq (MACS). Genome Biol. *9*, R137.

Please cite this article in press as: Salvi et al., A Self-Organized PLT/Auxin/ARR-B Network Controls the Dynamics of Root Zonation Development in *Arabidopsis thaliana*, Developmental Cell (2020), https://doi.org/10.1016/j.devcel.2020.04.004

STAR★METHODS

KEY RESOURCES TABLE

REAGENT or RESOURCE	SOURCE	IDENTIFIER
Antibodies		
Rabbit polyclonal anti-GFP	Abcam	Cat# ab290; RRID: AB_303395
Bacterial and Virus Strains		
Escherichia coli DH5α	N/A	N/A
Agrobacterium tumefaciens GV3101	N/A	N/A
Chemicals, Peptides, and Recombinant Proteins		
Murashige & Skoog basal salts Medium	Duchefa	Cat# M0221
Plant-agar	Duchefa	Cat# P1001
MES	Duchefa	Cat M1503
Sucrose	Duchefa	Cat# S0809
Agarose	Aurogene	Cat# AU1103
Kanamycin	Sigma-Aldrich	Cat# K1377
Rifampicin	Duchefa	Cat# R0146
Tetracycline	Duchefa	Cat# T0150
Gentamicin	Duchefa	Cat# G0124
Streptomycin	Duchefa	Cat# S0148
Spectinomycin	Duchefa	Cat# S0188
Phosphinothricin (PPT)	Sigma-Aldrich	Cat# 77182-82-2
Phusion High-Fidelity DNA Polymerase	New England Biolabs	Cat# M0530S
Indole-3-acetamide (iam)	Sigma-Aldrich	Cat# 879-37-8
3-indolacetic acid (IAA)	Sigma-Aldrich	Cat# 87-51-4
Complete Protease Inhibitor Cocktail	Roche Diagnostics	Cat# 11697498001
X-GlcA, 5-Bromo-4-chloro-3-indolyl-ß-D-glucuronic acid	Duchefa	Cat# 114162-64-0
Dimethyl-sulfoxide	Sigma-Aldrich	Cat# 67-68-5
Ethanol	Sigma-Aldrich	Cat# 64-17-5
Na_2HPO_4	Duchefa	Cat# 10028-24-7
NaH_2PO_4	Carlo Erba	Cat# 7558-80-7
K_3 Fe(CN)$_6$	Sigma-Aldrich	Cat# 13746-66-2
K_4Fe(CN)$_6$	Sigma-Aldrich	Cat# 14459-95-1
Triton X100	Sigma-Aldrich	Cat# 9002-93-1
Chloral Hydrate	Acros	Cat# 302-17-0
Glycerol	Sigma-Aldrich	Cat# 56-81-5
Direct Red 23	Sigma-Aldrich	Cat# 3441-14-3
Propidium iodide	Sigma-Aldrich	Cat# 25535-16-4
Xylitol	Sigma-Aldrich	Cat# 87-99-0
Sodium deoxycholate	Sigma-Aldrich	Cat# 302-95-4
Urea	Acros	Cat# 57-13-6
Paraformaldehyde	Sigma-Aldrich	Cat# 30525-89-4
Phosphate buffered saline	Sigma-Aldrich	Cat# P3813
Glycine, Molecular Biology Grade	Sigma-Aldrich	Cat# 56-40-6
Phenylmethylsulfonyl fluoride (PMSF)	Sigma-Aldrich	Cat# 93482
Ethylenediaminetetraacetic acid (EDTA)	Sigma-Aldrich	Cat# 60-00-4
Protein A agarose beads (Upstate)	Sigma-Aldrich	Cat# 16-157
LiCl	Sigma-Aldrich	Cat# 7447-41-8

(*Continued on next page*)

Please cite this article in press as: Salvi et al., A Self-Organized PLT/Auxin/ARR-B Network Controls the Dynamics of Root Zonation Development in *Arabidopsis thaliana*, Developmental Cell (2020), https://doi.org/10.1016/j.devcel.2020.04.004

Continued

REAGENT or RESOURCE	SOURCE	IDENTIFIER
TRIS Ultrapure	Duchefa	Cat# 77-96-1
Periodic Acid	Sigma-Aldrich	Cat# P7875
Sodium metabisulphite	Sigma-Aldrich	Cat# 7681-57-4
Arabic gum	Sigma-Aldrich	Cat# 9000-01-5
Methanol	Sigma-Aldrich	Cat# 67-56-1
Hydrochloric acid	Sigma-Aldrich	Cat# 7647-01-0
RNase A	Roche Diagnostics	Cat# 10109169001
10 mg/mL Proteinase K	Roche Diagnostics	Cat# 40-5203-01
Miracloth	Merck Millipore Calbiochem	Cat# 475855-1)
Critical Commercial Assays		
SensiFAST™ Lo-Rox SYBR®	Bioline	Cat# BIO-92005
NucleoSpin RNA Plus	Macherey-Nagel	Cat# 740984
qPCRBIO SyGreen Mix	PCR Biosystems	Cat# PB20.11-05
Gel/PCR DNA Fragments Extraction Kit	Geneaid	Cat# DF100
NucleoSpin Plasmid	Macherey-Nagel	Cat# 740588
Gateway™ BP Clonase™ II	Thermo Fisher Scientific	Cat# 11789
Gateway™ LR Clonase™ II	Thermo Fisher Scientific	Cat# 11791
Superscript® VILO™ cDNA Synthesis Kit	Thermo Fisher Scientific	Cat# 11754
Rneasy® Micro Kit	Qiagen	Cat# 74004
MiniElute Reaction Cleanup kit	Qiagen	Cat# 28206
Deposited Data		
ChIP-seq experiment data	NCBI Gene Expression Omnibus	GEO: GSE134695
Experimental Models: Organisms/Strains		
A.thaliana: Col-0	Nottingham Arabidopsis Stock Centre	N/A
A.thaliana: Wassiwjeska	Nottingham Arabidopsis Stock Centre	N/A
A.thaliana: arr12-1	Nottingham Arabidopsis Stock Centre	SALK_ 054752
A.thaliana: arr12-2	Nottingham Arabidopsis Stock Centre	SALK_054752
A.thaliana: arr1-4	Nottingham Arabidopsis Stock Centre	SALK_042196
A.thaliana: plt1,2	Aida et al., 2004	N/A
A.thaliana: pCYC-B1:GUS	Dello Ioio et al., 2007	N/A
A.thaliana: 35S:ARR1-ΔDDK:GR	Moubayidin et al., 2013	N/A
A.thaliana: ARR1:GUS	Mason et al., 2005	N/A
A.thaliana: ARR2:GUS	Mason et al., 2005	N/A
A.thaliana: ARR11:GUS	Mason et al., 2005	N/A
A.thaliana: ARR12:GUS	Mason et al., 2005	N/A
A.thaliana: ARR20:GUS	Mason et al., 2005	N/A
A.thaliana: 35S:PLT2:GR	Galinha et al., 2007	N/A
A.thaliana: PLT2:YFP	Galinha et al., 2007	N/A
A.thaliana: PLT2::CFP	Galinha et al., 2007	N/A
A.thaliana: pWOX5:IAAH	Blilou et al., 2005	N/A
A.thaliana: DR5V2::VENUS	Liao et al., 2015	N/A
A.thaliana: R2D2	Liao et al., 2015	N/A
A.thaliana: DHCN4a	Smetana et al., 2019	N/A
A.thaliana: KRP2:GFP	Sanz et al., 2011	N/A
A.thaliana: 35S:KRP2:GFP	Sanz et al., 2011	N/A
A.thaliana: pARR12:ARR12:GFP	This manuscript	N/A
A.thaliana: pARR10:ARR12:GUS	This manuscript	N/A
A.thaliana: RCH2:GUS	This manuscript	N/A
A.thaliana:pRCH2:PLT2	This manuscript	N/A

(*Continued on next page*)

Please cite this article in press as: Salvi et al., A Self-Organized PLT/Auxin/ARR-B Network Controls the Dynamics of Root Zonation Development in *Arabidopsis thaliana*, Developmental Cell (2020), https://doi.org/10.1016/j.devcel.2020.04.004

Continued

REAGENT or RESOURCE	SOURCE	IDENTIFIER
A.thaliana:pARR10:ARR10:GUS	This manuscript	N/A
A.thaliana: RCH2:KRP2:CFP	This manuscript	N/A
A.thaliana: RCH2:GAL4 x UAS:KRP2:CFP	This manuscript	N/A
A.thaliana: RCH2:GAL4	This manuscript	N/A
Oligonucleotides		
See STAR Methods section and Table S2	N/A	N/A
Recombinant DNA		
pB7m34GW	Ghent University https://gatewayvectors.vib.be/collection	Vector ID: 2-15
p4p1-RCH2	Dr. R.Heidstra (Wageningen University, The Netherlands)	N/A
p221-GAL4-VP16	Dr. R.Heidstra (Wageningen University, The Netherlands)	N/A
p221-PLT2	This manuscript	N/A
p2p3-GUS	This manuscript	N/A
p4p1-pARR10	This manuscript	N/A
p221-ARR10	This manuscript	N/A
p2P3-eNOS	Prof. P.Benfey (Duke University, NC, USA) and Prof. R.Sozzani (North Carolina State University, NC, USA)	N/A
p2p3-CFP	Prof. P.Benfey (Duke University, NC, USA) and Prof. R.Sozzani (North Carolina State University, NC, USA)	N/A
p221-KRP2	This manuscript	N/A
p4p1-UAS	Di Mambro et al., 2019	N/A
pB7m34GW-pARR10:ARR10:GUS	This manuscript	N/A
pB7m34GW-RCH2:PLT2stop:eNOS	This manuscript	N/A
	This manuscript	N/A
pB7m34GW-UAS:KRP2:CFP	This manuscript	N/A
pB7m34GW-RCH2:GAL4-VP16:eNOS	This manuscript	N/A
pGreenII0229-ARR12:ARR12:GUS	Dello Ioio et al., 2007	N/A
pGreenII0229G-RCH2:GUS	Casamitjana-Martínez et al., 2003	N/A
Gateway® pDONR™p4p1/Zeo Vector	Thermo Fisher Scientific	Cat# 12535035
Gateway® pDONR™221 Vector	Thermo Fisher Scientific	Cat# 12536017
Gateway® pDONR™223 Vector	Thermo Fisher Scientific	Cat# N/A
Software and Algorithms		
ImageJ	http://rsbweb.nih.gov/ij	RRID: SCR_003070
In silico root Array eFP browser	http://bar.utoronto.ca/eplant/	N/A
Adobe Photoshop CS2	Adobe Acrobat	(RRID: SCR_002078)
Graphapad	http://graphpad.com/quickcalcs/ttest1/	N/A
Excel	Microsoft	N/A
bowtie version 1.1.1	Langmead et al., 2009	N/A
samtools version 1.2	Li et al., 2009	N/A
MACS2 (version 2.1.0)	Zhang et al., 2008	N/A
Integrated Genome Browser	http://bioviz.org/igb/index.html	N/A
MEME	http://meme-suite.org/tools/meme	N/A
DREME	http://meme-suite.org/tools/dreme	N/A
JASPAR database	http://jaspar.genereg.net/	N/A
AgriGO	http://bioinfo.cau.edu.cn/agriGO/	N/A
ReviGO	http://revigo.irb.hr/	N/A

(*Continued on next page*)

Please cite this article in press as: Salvi et al., A Self-Organized PLT/Auxin/ARR-B Network Controls the Dynamics of Root Zonation Development in *Arabidopsis thaliana*, Developmental Cell (2020), https://doi.org/10.1016/j.devcel.2020.04.004

Continued

REAGENT or RESOURCE	SOURCE	IDENTIFIER
Other		
Fitotron SGC 120 Growth chamber	Weiss Technik, UK	N/A
Zeiss Axio Imager A2	Zeiss	N/A
7500 Fast Real-Time PCR system	Applied Biosystems	N/A
Zen software	Zeiss	N/A
Zeiss LSM 780	Zeiss	N/A
Branson Sonifier 250D	Marshall Scientific	Cat# 100-214-239

RESOURCE AVAILABILITY

Lead Contact

Further information and requests for resources should be directed to and will be fulfilled by the Lead Contact, Sabrina Sabatini (sabrina.sabatini@uniroma1.it).

Materials Availability

Plasmids and transgenic plant lines generated in this study will be made available on request to the lead contact. This study did not generate new unique reagents.

Data and Code Availability

The code for the computational model generated in this study is available at http://bioinformatics.bio.uu.nl/khwjtuss/AuxinCytokinin/PlethoraRoot. The ChIP-seq original datasets generated during this study are available at the NCBI Gene Expression Omnibus under GEO: GSE134695. The published article includes the Table S1 dataset generated and analyzed during this study. It includes a list of the ARR12 presumptive target genes from the ChIP-seq experiment.

EXPERIMENTAL MODEL AND SUBJECT DETAILS

The *Arabidopsis Thaliana (L.) Heynh.* plants were used as the experimental model in the study.

Columbia-0 (*Col-0*) and *Wassilewskija* (*Ws*) ecotypes were used as wild types with mutants and transgenic lines in these backgrounds as detailed in the Key Resources Table.

The *arr12-1* (SALK_ 054752), *arr12-2* (SALK_054752), *arr1-4* (SALK_042196) mutants were obtained from Nottingham Arabidopsis Stock Centre and *plt1,2* were described previously (Aida et al., 2004; Galinha et al., 2007). *pCYC-B1:GUS*, *35S:ARR1-ΔDDK:GR* have been published in (Dello Ioio et al., 2007; Moubayidin et al., 2013). *ARR1:GUS*, *ARR2:GUS*, *ARR11:GUS*, *ARR12:GUS*,*ARR20:-GUS* have been published in (Mason et al., 2005). *pARR12:ARR12:GFP* plants were generated retransforming plants with the *pAR-R12:ARR12:GFP* construct published in (Dello Ioio et al., 2007), *RCH2:GUS* plants were generated retransforming plants with the construct published in (Casamitjana-Martínez et al., 2003).

The following transgenic plants used in this study:

- *35S:PLT2:GR, PLT2:YFP, PLT2::CFP* (Galinha et al., 2007) and *pWOX5:IAAH* (Blilou et al., 2005) were provided by prof. Ben Scheres.
- *DR5V2::VENUS* and *R2D2* (Liao et al., 2015) were provided by Prof. Dolf Weijers (Wageningen University, The Netherlands).
- *DHCN4a* (Smetana et al., 2019) plants were provided by Prof. Ari Pekka Mahonen (University of Helsinki, Finland).
- *KRP2:GFP* and *35S:KRP2:GFP* (Sanz et al., 2011) plants were provided by Prof. John Murray (University of Cardiff, United Kingdom).

Plant Growth Conditions

Seeds were surface sterilized with gaseous chlorine produced according the following reaction: 100 mL of 20% sodium hypochlorite and 3 mL of 37% of HCl for 3 hours. Then, seeds were stratified in agorose 0.1% at 4°C for 5 days in dark light conditions and sown on square Petri dishes (12×12cm) containing 50ml of solid half-strength (½) Murashige and Skoog (MS) growth medium: 0.02% Murashige and Skoog basal salts (Duchefa), 0.05% MES (Duchefa), 1% sucrose (Sigma-Aldrich) and 1% plant agar (Duchefa) at pH = 5.6. The plates were vertically incubated in a growth chamber at 22°C under long-day (LD; 16 h light/8 h dark) conditions with a light intensity of 130 μEm-2 s-1 and photosynthetically active radiation supplied by neon tubes (Fitothrone).

Please cite this article in press as: Salvi et al., A Self-Organized PLT/Auxin/ARR-B Network Controls the Dynamics of Root Zonation Development in *Arabidopsis thaliana*, Developmental Cell (2020), https://doi.org/10.1016/j.devcel.2020.04.004

METHOD DETAILS

Experiments

DIC and Confocal Microscopy Analysis

For light microscopy, roots were cleared with a solution composed of: 8 parts (volume) chloral hydrate (Sigma-Aldrich) : 3 parts (volume) glycerol : 1 part (volume) water. Root tissues were visualized using Nomarski optics under a Zeiss Axio Imager.A2 microscope with a dry 40× objective. For confocal microscopy, cell walls from 3 days post germination (3 dpg) and older roots were stained with 30 μM propidium iodide (Sigma-Aldrich) solution (30 μg/mL). Roots of 24 hpg, 36 hpg and 48 hpg were visualized after the mPS-PI staining protocol or the ClearSee + DirectRed staining procedure as specified (Truernit et al., 2008; Ursache et al., 2018). Images were acquired using Zeiss LSM 780 confocal microscope with an oil immersion 40× objective, with laser lines and setting according to the staining dye and the fluorescent protein(s) in analysis (Truernit et al., 2008; Ursache et al., 2018). Images were analyzed with ImageJ (ImageJ, RRID: SCR_003070), stitched and post-processed with Adobe Photoshop CS2 (RRID: SCR_002078). Image post-processing was minimal and restricted to corrections in brightness and contrast. All corrections were uniformly applied to the entire images so that all final figures properly reflect the original data.

Root Size and Root Meristem Size Analysis

The number of root cells (Figure S1) in imbibed seeds (0 hpg), at 24 hpg, 36 hpg, 2 dpg, 3 dpg, 5 dpg and 6 dpg in each root zone was counted in the cortex tissue, considering as cells of the Proliferation Zone those cells spanning from the QC to the first longitudinally non-isodiametric cell; as TZ those elongated cells where their length was less than the double of their width; as cells belonging to the Elongated/Differentiated Zone those cells that displayed a length of more than the double of their width up to the beginning of the hypocotyl organ (marked by the presence of two cell files in its cortex tissue). For younger than 36 hpg roots, cells enclosed within the LRC were considered belonging to the Proliferation Zone, while cells above the LRC and below the double cell file of the cortex (which marks the hypocotyl starting) were considered as hypocotyl-radicle junction cells. At least, 10 roots were analyzed for each time point and the mean and SD were then calculated. For this experiment, two independent biological replicates were carried out.

Root meristem size is expressed as the number of meristematic cortex cells in a file extending from the QC to the first longitudinally elongated cortex cell (Di Mambro and Sabatini, 2018). The number of root meristematic cortex cells was counted considering as meristematic cells those spanning from the QC to the first longitudinally non-isodiametric cell where their length was less than the double of their width. The normality of the sample distribution was tested with a Shapiro-Wilk test and then Student's t-test was performed to assess the significance of the differences between each sample and the control sample (http://graphpad.com/quickcalcs/ttest1/). p-values are indicated in the corresponding figure and figure legend, with at least $p<0.05$ or lower considered statistically significant. Graphs, plots and statistics (mean, SD) were performed with Excel software.

Clonal Analysis

The clonal analysis was performed using *DHCN4a* doubly transgenic plants (Smetana et al., 2019).

DHCN4a seeds were routinely sterilized, plated and grown in the growth chambers for 30 hpg as described in the *Plant Growth Conditions* subsection. Then, *DHCN4a* germinating seeds were subjected to heat shock at ~37°C (in a dark room) for 1 hour. The plates were then transferred at 4°C (in a dark room) for 15 minutes and put back in the growth chambers (Fitothrone) for 6 hours. Plants randomly generated GFP clones upon heat shock. The plants were then screened at the confocal microscope using vital propidium iodide as counterstaining (30μL/100μL) and images were acquired for plants carrying GFP-positive cells in proximity of the last LRC cell in the root. The same plants were then put back into a Petri plate containing the (½) Murashige and Skoog (MS) and back into the growth chamber to follow up GFP-positive cells over time at following time-points. A total of 3 roots (n=3) displaying GFP-positive cells falling in the region of the putative incipient TZ were found at 36 hpg and their behaviour followed over time (60hpg). Among these samples, results were consistent with the one showed in Figure 1. Images were stitched and post-processed (corrections in brightness/contrast/color balance to better visualize the GFP clones so that final figures reflect the original data) with Adobe Photoshop CS2 (RRID: SCR_002078).

Drug Treatments

36 hpg-old *ARR12:GUS* seedlings were transferred with tweezers onto solid ½ MS medium plates containing *iam* (Indole-3-acetamide) (Sigma-Aldrich) at a final concentration of 10 μM or 3-indol acetic acid (IAA) (Sigma-Aldrich) at a final concentration of 5 μM; and in parallel onto MS plates containing respectively the corresponding volumes of DMSO and ethanol as a control, in both cases, for 6 hours.

3 dpg-old *35S:PLT2:GR* and 5 dpg-old *35S:ARR1-ΔDDK:GR* seedlings were transferred with tweezers onto solid ½ MS medium plates containing *dexamethasone* (Sigma-Aldrich) at a final concentration of 10 μM and, in parallel, onto MS plates containing the corresponding volumes of ethanol as a control for 2 hours.

B-Glucuronidase (GUS) Histochemical Assay

β-Glucuronidase activity of transgenic lines carrying the GUS enzyme was assayed essentially as described in (Moubayidin et al., 2013) using the ß-glucoronidase substrate X-GlcA, (5-Bromo-4-chloro-3-indolyl-ß-D-glucuronic acid, Duchefa) dissolved in DMSO. X-gluc solution: 100 mM Na_2HPO_4, 100 mM NaH_2PO_4, 0.5 mM K3 $Fe(CN)_6$, 0.5 mM $K_4Fe(CN)_6$, 0.1% Triton X100 and 1 mg/ml X-gluc. Seedlings were incubated at 37°C in the dark for an appropriate time allowing tissue staining depending on the GUS line assayed. Imaging was done using the Axio Imager.A2 (Zeiss) microscopy. For each line and time-point, at least 50 roots

Please cite this article in press as: Salvi et al., A Self-Organized PLT/Auxin/ARR-B Network Controls the Dynamics of Root Zonation Development in *Arabidopsis thaliana*, Developmental Cell (2020), https://doi.org/10.1016/j.devcel.2020.04.004

were analyzed, and the percentages of phenotypes were evaluated. Images were stitched and post-processed with Adobe Photoshop CS2 (RRID: SCR_002078). Image post-processing was minimal and uniformly applied, consisting in corrections in brightness/contrast and in the addition of a uniform background.

Cloning and Generation of Transgenic Plants

Cloning was performed using the MultiSite Gateway cloning system® (ThermoFisher Scientific™) according to the manufacturer's manual (https://tools.thermofisher.com/content/sfs/manuals/gatewayman.pdf).

Gateway® pDONR™p4p1/Zeo Vector (ThermoFisher Scientific™) for promoter clones, Gateway® pDONR™221 Vector (ThermoFisher Scientific™) for gene of interest and Gateway® pDONR™223 (ThermoFisher Scientific™) for reporter or terminator clones were used

For *pRCH2:PLT2* construct: the *p4p1-pRCH2* vector was provided by Dr. Renze Heidstra (Wageningen University, the Netherlands); the *PLT2* gene (AT1G51190) was PCR-amplified from genomic *Col-0* DNA using Phusion Taq polymerase (ThermoFisher Scientific™) with appropriate *attB* oligonucleotides complimentary to *PLT2* sequences, then subcloned into the pDONR221™ vector via a BP recombinase reaction (ThermoFisher Scientific™) to generate the *p221-PLT2* vector; the *p2p3-eNOS* vector was kindly provided by Prof. Benfey and Prof. Rosangela Sozzani. The *pB7m34GW* (which includes the gene conferring resistance to Phosphinotricine (PPT, Duchefa) for following *in planta* selections), from the collection available from Ghent University, Belgium, was used as destination vector for the LR II recombinase reaction (ThermoFisher Scientific™).

For *pARR10:ARR10:GUS* construct: the ~ –2000 bases upstream the starting codon of *ARR10* gene were PCR-amplified from genomic *Col-0* DNA using Phusion Taq polymerase (ThermoFisher Scientific™) with appropriate *attB* oligonucleotides complimentary to the sequence, then subcloned into the pDONRp4p1™ Vector via a BP recombinase reaction (ThermoFisher Scientific™). Similarly, the *ARR10* gene (AT4G31920) was PCR-amplified from genomic *Col-0* DNA using Phusion Taq polymerase (ThermoFisher Scientific™) with appropriate *attB* oligonucleotides complimentary to *ARR10* sequence, then subcloned into the pDONR221™ Vector. The *p2p3-GUS* vector was generated by PCR-amplifying the *GUS* gene from the *RCH2:GUS* construct with appropriate *attB* oligonucleotides complimentary to *GUS cds* sequence. The *pBm43GW* (which includes the gene conferring resistance to Phosphinotricine for following *in planta* selections), from the collection available from Ghent University, Belgium, was used as destination vector for the LR II recombinase reaction (ThermoFisher Scientific™).

RCH2>>KRP2 transgenic plants were generated crossing *RCH2:GAL4* plants *x UAS:KRP2:CFP* plants.

For the *RCH2:GAL4* construct: the *p4p1-RCH2* and the *p221-GAL4VP16* vectors were kindly provided by Dr. Renze Heidstra (Wageningen University, the Netherlands). The *pB7m34GW* (Ghent University, Belgium), was used as destination vector for the LR II Plus recombinase reaction (Thermo Fisher Scientific™) with *p4p1-RCH2*, *p221-GAL4VP16* and *p2p3-eNOS* (kindly provided by Prof. P. Benfey and Prof. R. Sozzani) vectors.

For the *UAS:KRP2:CFP* construct: the *p4p1-UAS* vector was generated in our published Di Mambro et al. (2019); the KRP2 gene (AT3G50630) was PCR-amplified from genomic *Col-0* DNA using Phusion Taq polymerase (ThermoFisher Scientific ™) with appropriate *attB* oligonucleotides complimentary to KRP2 sequences, then subcloned into the pDONR221™ vector via a BP recombinase reaction (ThermoFisher Scientific™) to generate the *p221-KRP2* vector; the *p2p3-CFP* vector was kindly provided by Prof. P. Benfey and Prof. R. Sozzani. The *pB7m34GW* (which includes the gene conferring resistance to Phosphinotricine for following *in planta* selections), from the collection available from Ghent University, Belgium, was used as destination vector for the LR II recombinase reaction (Thermo Fisher Scientific™).

All constructs were sequenced prior to transformation via floral dipping into *Col-0* backgrounds.

The following oligonucleotides (see Table S2 for their sequences) were used:

attB1-PLT2-FWD and attB1-PLT2stop-REV for cloning *PLT2* cds;
attB1-pARR10 FWD and attB4-pARR10 REV for cloning *ARR10* promoter;
attB1-ARR10-FWD and attB1-ARR10-REV for cloning *ARR10* cds;
attB2-GUS FWD and attB3-GUS REV for cloning *GUS* cds;
attB1-KRP2-FWD and attB1-KRP2-REV for cloning *KRP2* cds.

ChIP Followed by High Throughput Sequencing

For the genome-wide identification of ARR12 direct targets, firstly two independent biological replicates of a Chromatin Immunoprecipitation (ChIP) experiment were performed (Sozzani et al., 2010). Briefly, material from micro-dissected 3 dpg-old root apical meristems expressing *pARR12:ARR12:GFP* and Col-0 were used. The roots were fixed in 1,8% formaldehyde (in 1xPBS buffer supplemented with 5mM EDTA) at room temperature applying house-vacuum. After fixation, 2.5 M glycine was added in ice. Solution was filtered away using Miracloth (Merck Millipore Calbiochem, 475855-1) and samples were freezed in liquid N_2. The tissues were ground in liquid N_2, and resuspended in extraction buffer [50mM Tris-HCl, pH 7.5, 150mM NaCl, 1% Triton X-100, 0.1% Na deoxychlorate, 2.5mM EDTA, 10% glycerol, supplemented with 1X protease inhibitor cocktail (Roche,) and 1mM PMSF (Sigma)]. Samples were filtered through miracloth (Merck Millipore Calbiochem, 475855-1) and centrifuged to collect nuclei. The pellet was resuspended in ice-cold extraction buffer, and centrifuged. Samples were sonicated for 3 cycles of 10 seconds at 35-40% amplitude (Branson Sonifier, Marshall Scientific). An aliquot of each sample was retained as the INPUT control (and was not further treated with the addition of antibody). Extraction Buffer, 0.1% SDS, 10 μl BSA (of 20mg/ml) were added. Immunoprecipitation was done using a rabbit polyclonal antibody to GFP (ab290; Abcam). 20 μl of solid volume of BSA-equilibrated protein A agarose beads (Upstate,

Please cite this article in press as: Salvi et al., A Self-Organized PLT/Auxin/ARR-B Network Controls the Dynamics of Root Zonation Development in *Arabidopsis thaliana*, Developmental Cell (2020), https://doi.org/10.1016/j.devcel.2020.04.004

Cat#16-157) were added. The beads were washed consecutively with low salt washing buffer (150 mM NaCl,.2% SDS, 0.5% Triton X-100, 2 mM EDTA, 20 mM Tris-HCl pH 8), high salt washing buffer (500 mM NaCl,.2% SDS, 0.5% Triton X-100, 2 mM EDTA, 20 mM Tris-HCl pH 8), LiCl washing buffer (0.25 M LiCl,.5% NP-40,0.5% sodium deoxycholate, 1 mM EDTA, 10 mM Tris-HCl pH 8) and TE buffer. Finally, TES (25mM Tris-HCl pH 8.5, 5mM EDTA, 0.5% SDS) was added and incubated at 65°C. 20mg/ml RNase A and then 10mg/ml Protease K (Roche) were added. Crosslink reversal was done at 65°C. The DNA was cleaned up using the MiniElute Reaction Cleanup kit (QIAGEN). An aliquot of the isolated DNA was used to check its quality (2% agarose gel electrophoresis of the ChIPped DNA to check length of sonicated fragments followed by qPCR analysis of putative ARR12 target genes) prior to sequencing. 50 bp single-end sequencing by Illumina HiSeq 2000 platform and library construction were performed by IGA Technology Services Srl, Udine, Italy.

ChIP-Sequencing Analysis

Reads from two independent biological replicates (both INPUT and ChIP libraries) were aligned to the Arabidopsis genome build TAIR10 by *bowtie* version 1.1.1 (Langmead et al., 2009) with the following settings "-m 1 -k 1 –best –strata –sam". Duplicated reads and reads with low mapping quality were identified and removed with *samtools* version 1.2 (Li et al., 2009). Enriched intervals between IP sample and its relative INPUT were identified by MACS2 (version 2.1.0) program (Zhang et al., 2008) with following settings "-g 1.35e8, -B and -q 0.01" and merged the overlapped peaks from two replicates. In order to separate signal from noise across the two replicate experiments the IDR (Irreproducible Discovery Rate) threshold of 0.01 was used. The peaks were classified according to the following criteria: (i) peaks occurring within 2,000-bp upstream and 200-bp downstream of the TSS of a gene were classified as promoter region binding sites; (ii) peaks localized within a gene body were further categorized as CDS, 5′-UTR, 3′-UTR, or intron region binding sites; and (iii) peaks not selected by the two preceding criteria were classified as intergenic region binding sites. The differentially enriched peaks of ARR12 binding in *pARR12:ARR12:GFP* roots were also determined using MACS *bdgcmp* pipeline in comparison with Col-0. Bedgraph files were visualized with the Integrated Genome Browser (http://bioviz.org/igb/index.html).

Sequence Motif and Gene Ontology Analysis

To discover the consensus DNA sequence motifs underlying the ARR12 binding peaks, all the ARR12 binding peaks with summit score >10 in *pARR12:ARR12:GFP* were first trimmed to 1000-bp genomic regions centered on their peak summits. Then, DNA motifs within these 1000-bp DNA sequences were identified by MEME and DREME, tools for motif discovery, with default parameters (http://meme-suite.org/tools/meme and http://meme-suite.org/tools/dreme). To identify potential cofactors of ARR12, the 1000 bp sequences surrounding the summits of the ARR12 binding peaks were searched for plant TF binding motifs in JASPAR database (http://jaspar.genereg.net/). GO analysis was performed using AgriGO (http://bioinfo.cau.edu.cn/agriGO/) and visualization of enriched GO categories using ReviGO (http://revigo.irb.hr/).

ChIP Followed by qRT-PCR

A total of two additional independent ChIP experiments in *pARR12:ARR12:GFP* and *Col-0* seedlings were performed dissecting sections comprising 5 millimeters of root lengths from *Col-0*, as the control, or *pARR12:ARR12:GFP 3* days old roots as described above (*see ChIP followed by high throughput sequencing* sub-section for protocol details). Enrichment of promoter-regions of the *PLT2* was determined using RT-qPCR. The qPCR efficiency of 2-fold amplifications per cycle was tested for every oligonucleotide, and relative enrichment was calculated by normalizing the amount of target DNA, first to the internal control gene *ACTIN2* and then to the corresponding amount in the input. Data are mean and SD of one out of two technical replicates from a representative experiment, out of the three biological replicates performed. Tiling along the *PLT2* promoter was done using the sets of adjacent specific amplified regions listed in STAR Method Table 2.

Material from ChIP experiments of *pARR1:ARR1:GFP* and *Col-0* seedlings were performed in (Di Mambro et al., 2017) (GEO accession no. GSE70595) and re-used for this study. Enrichment of the promoter-region of the *KRP2* gene was determined using RT-qPCR. The qPCR efficiency of 2-fold amplifications per cycle was tested, and relative enrichment was calculated by normalizing the amount of target DNA, to the internal control gene *ACTIN2* (see below for the sequence, subsection "*RNA isolation, retro-transcription and qRT-PCR*"). Data are means and SDs from a representative experiment out of two technical replicates, out of the two biological replicates performed. Tiling along the *KRP2* promoter was done using the sets of adjacent specific amplified regions listed in STAR Method Table 2.

RNA Isolation, Retrotranscription and qRT-PCR

Total RNA was extracted from 3-day-old *Col-0* and *arr12-1* roots using the RNeasy Mini Kit (Qiagen) and NucleoSpin RNA Plus (Macherey-Nagel) and performing a DNase treatment (Qiagen) step before retrotranscription. The cDNA was retrotranscribed using the SuperScript® III First-Strand VILO™ cDNA Synthesis Kit (Thermo Fisher Scientific). Quantitative RT-PCR (qRT-PCR) analysis were performed using the gene-specific primers listed in STAR Method Table 2.

All the oligonucletides were tested for their qPCR efficiency of 2-fold amplifications per cycle by qRT-PCR with the Standard curve method. PCR amplifications were carried out using the SensiFast SYBR Lo-Rox (Bioline) mix and the qPCR BIO SyGreen Mix (PCR BioSystems). Amplification was monitored in real time with a 7500 Real Time PCR System (Applied Biosystems). Amplification of *ACTIN 2* and *GLYCERALDEIDE-PHOSPHATE-DEHIDROGENASE GAPDH* served as housekeeper controls. Data are expressed in $2^{-\Delta\Delta ct}$ value. Three technical replicates of qRT-PCR were performed on two independent RNA batches. Results were comparable in all the experiments. Student's t-test was performed to assess the significance of the differences between each sample and the control sample.

Please cite this article in press as: Salvi et al., A Self-Organized PLT/Auxin/ARR-B Network Controls the Dynamics of Root Zonation Development in *Arabidopsis thaliana*, Developmental Cell (2020), https://doi.org/10.1016/j.devcel.2020.04.004

Reporter Gene Analysis

pPLT2:CFP and *PLT2:YFP* reporter lines were crossed to *arr12-1,* and *KRP2:GFP* was crossed to *arr1-4*. Plants homozygous for the *arr12-1* and *arr1-4* mutations as well as for transgene markers were isolated from the F3 population and analyzed in homozygous lines. In all experiments, parental transgenic lines were used as control. The homozygous *arr12-1* and *arr1-4* mutations were isolated by PCR as described (http://signal.salk.edu/tdnaprimers.2.html). Plant DNAs were analyzed with specific oligonucleotides complementary to gene sequence flanking the insertion and the sequence of the T-DNA. These oligonucleotides (listed in (Dello Ioio et al., 2007)) discriminate the wild type from the mutated allele based on the amplicon length.

PLT2:YFP Fluorescence Quantification

The fluorescence intensity of plants carrying *PLT2:YFP* in wild type and *arr12-1* mutant backgrounds were quantified at 24 hpg, 36 hpg, 48 hpg and 72 hpg on the *Maximum Intensity Projection* pictures of Z-stacks images of root tips acquired with a Zeiss LSM 780 laser-scanning microscope (Argon lines 488nm). After collecting the samples at the appropriate developmental stage, they were fixed and treated according to the Clear See protocol (Ursache et al., 2018) and stained with Direct Red dissolved in the Clear See solution. Z-stack images (intervals ~1 μm; 4-7 stacks per sample) of root tips were acquired with a Zeiss LSM 780 laser-scanning microscope (ZEN 2010 software). Confocal and acquisition settings as follow:

- mode of acquisition, single track
- laser beam 514 nm
- emission filters 511-547 nm for *YFP*; 606-735 nm for *DirectRed*
- pinhole 55 μm
- laser master gains 1030 for *YFP* (*chS1*) and 870 (*ch1*) for *DirectRed*
- digital offsets 0 for *YFP*, variable for *DirectRed*

Pictures were acquired with the same microscope settings for the 24 and 36 hpg time points (first tranche of the experiment) and the 48 and 72 hpg time points (second tranche of the experiment). A single Z-stack acquisition was taken for each root. To allow comparisons of samples from both experimental tranches, acquisition of 24 hpg samples (not used in the previous tranche of the experiment to avoid YFP photobleaching biases) were also taken during the second experimental tranche and used as reference to normalise the first tranche to the second one. The plugin *Measure Mean Gray Value* of the software *ImageJ* was used on images where a segmented linear ROI in the epidermis tissue was drawn by hand for each root. *PLT2:YFP* expression profiles were then derived by plotting the *Mean Gray* values obtained from the green channel (corresponding to the YFP fluorescence) against the distance from the QC (in μm) and then these values for the 24 and 36 hpg time points (first tranche of the experiment) were normalized to those for the 48 and 72 hpg time points (second tranche of the experiment). The number of samples analysed was at least 10 for each time point. Means and SD were computed per 15μm distance from the QC. Mean gray values were compared within the SCN and at the TZ location across timepoints- and between wild type and arr12-*1* by 1-way ANOVA and Student's t-test.

Quantification of R2D2 Reporter

Analyses of the *R2D2* (Liao et al., 2015) fluorescence intensity at 36 hpg were performed on Maximum Intensity Projections of Z-stack images (intervals ~1 μm) (generated via the *Fiji* software) of root tips acquired with a Zeiss LSM780 laser-scanning microscope. To analyse the fluorescence signal in cell nuclei of selected root tissues, nuclei areas were manually selected in the cortex tissue of the roots using the *ROI manager* tool of the *Fiji* software. The resulting signals were obtained by the *Mean Gray Value* tool either for *mDII- nuclear tdtomato* and *DII-VENUS* signal. The ratio between *mDII-ntdtomato* signal and *nuclear DII-VENUS* signal (mDII/DII) was then computed in each cell nucleus. These signal intensity ratios were normalized for the lowest value of the ratio between *nuclear mDII-ntdtomato* signal and *nuclear DII-VENUS* signal (mDII/DII) in each root sample and then aligned among different roots referring to the last meristematic cell value in each root. Mean and SD were computed for each meristematic cell position from all the samples. The results from the experiment were linearly plotted with Excel software, converting them into "distances from QC in μm" (x-axis) considering the length of a meristematic cell as 10 μm. In order to compare the mean of multiple samples (i.e. the mDII/DII ratio corresponding to different meristematic cell positions) 1-way ANOVA for repeated measures test was performed among cells in the +2/-5 cells from the TZ position. *p-values* < 0.05 were considered statistically significant. The experiment was repeated twice, and the number of samples analysed was n=18 and n=30. Comparable results were obtained in each replicate, in Figure 3 a representative result is shown. In more detail, an auxin minimum (a minimum value in the mDII/DII ratio) was found to be dispersed along the meristematic cortex cells (-5 cells from the TZ): the 1-way ANOVA for repeated measures test computed for the mDII/DII ratios of the last meristematic cell (TZ position identified as in *Root size and root meristem size analysis* paragraph) and for -5 cells was not significant at p<0.05 (F-ratio value ~1.60; p-value >0.05). The auxin minimum value was found in cells spanning from the "TZ position" to the "-5 position from the TZ" in the 15/18=83.5% of the roots. The 1-way ANOVA for repeated measures test computed for the mDII/DII ratios of the last meristematic cell ("TZ position") and "+2 position from the TZ" cells was significant at p < 0.0005 (F-ratio value = 15.67678; p-value= 0.000027) indicating an auxin rise in these cells. The auxin minimum value was never found in the + 2 cells from the TZ (0/18=0%).

Computational Model

Growing Root Zonation Model

The model we developed in this study is a combination and extension of two of our previously developed models, the Mähönen et al. (2014) model that was used to study the role of auxin and PLETHORA (PLT) in controlling root growth dynamics, and the van den Berg et al. (2016) model that demonstrated the importance of a realistic root tip architecture for correctly simulating root auxin patterns.

Please cite this article in press as: Salvi et al., A Self-Organized PLT/Auxin/ARR-B Network Controls the Dynamics of Root Zonation Development in *Arabidopsis thaliana*, Developmental Cell (2020), https://doi.org/10.1016/j.devcel.2020.04.004

Tissue Architecture

The model incorporates an idealized, realistic root anatomy, with a wedge shaped root tip encompassed by a lateral root cap, on which intracellular regulatory dynamics, intercellular hormone and protein transport, and cell growth, division, expansion and differentiation are modeled (Figure 3). The model describes all tissue types present in the adult Arabidopsis root, from inside to outside these are the vasculature, pericycle, endodermis, cortex and epidermis, and for the root tip also the quiescent center, stem cells, columella cells and root cap (Figure 3A). Additionally, the model describes the different developmental zones present in the root (Figure 3E, see also later sections). The model is grid based, meaning that individual cells, but also cell walls, occupy a set of connected grid points. Modeled cell sizes and shapes are based on experimental data, with cell widths dependent on tissue type (18microm epidermis, 20 microm cortex, 12 microm endodermis, 8 microm pericycle and 6 microm vasculature), and cell height dependent on the developmental phase of the cell (just divided cells have a height of 8 microm and increase to 16microm before dividing, maximally elongated cells reach a height of 144 microm).

To simulate realistic auxin patterning, we incorporate cell type specific and zone specific expression patterns for both the auxin exporting PIN proteins and the auxin importing AUX/LAX proteins (Figure 3A), as done in other modeling studies (Band et al., 2014; van den Berg et al., 2016; Grieneisen et al., 2007; Mähönen et al., 2014) with adjustments to compensate for differences in the precise tissue layout used, as well as to ensure robust auxin patterning in a large range of meristem sizes. Specifically, for AUX1 spatial transitions in AUX1 levels were applied more smoothly. Also, the start of epidermal AUX1 patterning was chosen to overlap more with the end of the lateral root cap, ensuring more efficient auxin transport from the lateral root cap into the rest of the reflux loop. Additionally, we found that to ensure that for larger meristems the lateral root cap still is able to transport significant amounts of auxin into the reflux loop at the shootward boundary of the meristem, PIN patterning in the lateral root cap and epidermis required adjustments. The smaller wedge shaped part in this study compared to that used in van den Berg et al. turned out to reduce effective auxin loading in the lowermost parts of the epidermis, to compensate for this effect we increased the inwards PIN2 mediated flux in the lowermost part of the lateral root cap. Additionally, above the stem cell niche, we lowered the level of lateral PIN2 oriented from the lateral root cap towards the epidermis Combined these adjustments ensure that more auxin is first taken up and subsequently maintained in the lateral root cap, and less is lost through reflux alongside the meristem. This ensures that the lateral root cap maintains sufficient auxin for the reflux taking place at the shootward end of the meristem.

Previous research has indicated that in addition to auxin influx from the shoot, local root tip auxin production plays an important role in root auxin patterning (Ljung et al., 2005; Stepanova et al., 2008). We therefore incorporated elevated auxin production in the QC, columella and lateral root cap (Figure 3A, auxin production in the QC 50x basal rate, SCN 25x basal rate, and LRC 10x basal rate).

Growth Dynamics

To be able to apply the simplified algorithm we previously used in the Mähönen et al., 2014 model for cell growth and expansion, in which cells increase in size through the simple addition of a row of grid points and the upward shifting of above lying cells on our simulation grid, cell growth, division and expansion dynamics are restricted to cells with a strictly rectangular shape. Thus, cell division in the columella, lowermost lateral root cap and QC are ignored. In order to avoid the biologically unrealistic sliding of cells past one another, we assume that cell growth and developmental transitions are coordinated across neighboring cells (see section on radial coordination).

Growth, division and expansion of cells are modeled as described previously (Mähönen et al., 2014). Briefly, growth and expansion of cells is modeled in a discretized manner by adding a row of grid points to an existing cell at given time intervals (Figure 3E). Timing of these growth and expansion events is determined by the duration of cell division (typically 10 hours), and expansion (typically 7 hours), respectively. Note that since growth per microm is measured to be constant (Brumfield, 1942; Weele et al., 2003), cell-level growth rate increases exponentially with cell size, causing cellular growth events to occur more closely spaced in time as cells become larger. The growth events lead to the increase of cell volume. In case of cytoplasmic, but not vacuolar expansion driven growth, we compute the resulting dilution in cytoplasmic concentrations (concentration after growth event = concentration before growth event times the fraction of volume increase). In the meristimatic zone, cells divide once they have doubled their size (change in height from 8 to 16 microm). Upon division, daughter cells inherit their maternal PIN and AUX/LAX patterns, yet cells adjust their PIN and AUX/LAX pattern when entering a new developmental zone in which these patterns are different.

Zonation

Experimental data indicate that besides discerning a meristem, elongation and differentiation zone, inside the meristem two seperate zones can be distinghuished. A first proximal zone consists of mitotically active cells, whereas a second distal zone comprising up to one third of the total meristem consists of cells that hardly undergo division yet still slowly grow (Boudonck et al., 1998; Scacchi et al., 2010; Verbelen et al., 2006), Rather than undergoing rapid vacuolar expansion these cells still appear to be growing cytoplasmatically. We therefore extended our previous description of developmental zonation with these two distinct meristematic domains, simplifying matters by assuming no further divisions in the distal meristem zone (Figures 3D and 3E).

In our earlier model, we assumed PLT levels to be the sole determinant of the boundary between meristem and elongation zone (Mähönen et al., 2014), ignoring the importance of cytokinin signaling for root zonation dynamics (Di Mambro et al., 2017; Moubayidin et al., 2010; Raines et al., 2016). Additionally, no subdivision of the meristem into two distinct zones was yet considered in that model. To investigate how auxin, PLT and cytokinin signaling together govern detailed root meristem patterning we thus need a more realistic, versatile modeling of zonation, enabling the generation of a within meristem boundary as well as a meristem-elongation zone boundary, and enabling the incorporation of PLT and cytokinin inputs on these boundaries. To achieve this, we make use of the observation that root zonation is accompanied by a gradual decline of division associated transcription factors and an increase of

Please cite this article in press as: Salvi et al., A Self-Organized PLT/Auxin/ARR-B Network Controls the Dynamics of Root Zonation Development in *Arabidopsis thaliana*, Developmental Cell (2020), https://doi.org/10.1016/j.devcel.2020.04.004

differentiation associated transcription factors (Wendrich et al., 2017), with the transition in dominance from division to differentiation markers demarcating the transition from meristem to elongation zone. Based on this we incorporated in our model a generalized (DivTF) and elongation factor (ElongTF). We assume that if the division factor exceeds a certain level cells are meristematic, while if the elongation factor exceeds a certain level cells start elongation and differentiation, and if both division and elongation factors are below these threshold levels cells are in a slowly growing but no longer dividing state (Figure 3D).

Based on our previous demonstration that overexpression of PLT maintains cells in a dividing state, while removal of PLT expression leads to meristem differentiation (Mähönen et al., 2014), we incorporate that PLT enhances the expression of DivTF while repressing the expression of ElongTF. Additionally, based on our earlier research on ARR-mediated CK signalling demonstrating its elongation (Pacifici et al., 2018; Takatsuka et al., 2018)) and differentiation promoting effects, we incorporate the promotion of ElongTF by both ARR1 and ARR12. Since elongation and differentiation, although postphoned, also occur in absence of cytokinin signalling, an ARR independent production of ElongTF is also taken into account. Next, based on the data obtained in the current study showing that ARR1, via inducing KRP2, represses cell cycle progression (Figures 7H and 7I main manuscript), we incorporated the ARR1 dependent repression of DivTF. In the arr1,arr12 double mutant, in absence of ARR mediated auxin and PLT antagonism, a long and shallow PLT gradient arises. In absence of further regulation on DivTF and ElongTF this results in a relatively large region in which DivTF is already below the threshold for division yet ElongTF is not yet above the threshold for elongation and differentiation, resulting in an unrealistically long transition zone domain (dark green in Figures 3D and 3E). To prevent this, we incorporate a repressive effect of the division status itself, as represented by DivTF level, on elongation and differentiation. This regulatory effect represents the repressive effects of epigenetic modifications associated with stemness and division on cell elongation (Krichevsky et al., 2009) As a consequence of this additional regulation, if PLT levels drop, ElongTF increases both directly due to the PLT drop as well as indirectly due to the decrease in DivTF levels, which both contribute to a release of repression of ElongTF. Combined, this ensures a realistically sized transtion zone even in absence of ARRs. Combined this led to the following equations:

$$\frac{dDivTF}{dt} = \frac{p_{Div} * Plts^2}{Plts^2 + KM_{Plts,Div} *} * \frac{KM^2_{ARR1,Div}}{ARR1^2 + KM_{ARR1,Div^2}} - d_{Div} * DivTF \,, \qquad \text{(Equation 1)}$$

where p_{Div} is the maximum production rate of DivTF, $KM_{Plts,Div}$ is the PLT level for which the production is raised to half maximum, $KM_{ARR1,Div}$ is the ARR1 level for which the DivTF production is downregulated to half maximum, and d_{Div} is the DivTF degradation rate.

$$\frac{dElongTF}{dt} = p_{El} * \left(\frac{Divfrac * KM^4_{,El}}{DivTF^4 KM^4_{Div,El}} + \frac{Pltsfrac * KM^2_{Plts,El}}{Plts^2 + KM^2_{Plts,El}} + \frac{ARRFrac * ARRs^2_{eff}}{ARRs^2_{eff} + KM^2_{ARRs,El}} \right) - d_{El} * ElongTF \qquad \text{(Equation 2)}$$

$$ARRs_{eff} = ARR1 * ARR1maximumeffect + ARR12 \,,$$

where pEl is the maximum production rate of ElongTF, Divfrac is the maximum fraction the DivTF can repress ElongTF production by, $DivKM_{El}$ is the DivTF level for which this repression is half maximum, pltsfrac is the maximum fraction PLT can repress pEl by, $PltsKM_{El}$ is the PLT level for which this repression is half maximum, ARRfrac is the maximum fraction ARRs can raise ElongTF production by, $ARRsKM_{El}$ is the ARR effect level at which said raise is half maximum, dEl is the degradation rate of ElongTF, and ARR1maximumeffect is the weight factor for ARR1 resulting in a stronger effect of ARR1 over ARR12 on ElongTF. Parameter values are given in STAR Method Table 1.

Star Method Table 1. Growth parameters

Parameter	Explanation	Fit based on	Value	Dimension
p_{Div}	Maximum production rate of division TF	arr1arr12 knockout	0.01	s^1
d_{Div}	Degradation rate of division TF	arr1arr12 knockout	0.0001	s^1
$KM_{Plts,Div}$	PLT concentration at which PLT induction of division TF is half maximum	arr1arr12 knockout	40	
$KM_{ARR1,Div}$	ARR1 level at which ARR repression of division TF is half maximum	arr1 knockout	20	
Divisionthreshold	Division TF concentration above which cells divide rapidly	arr1arr12 knockout	45	
p_{El}	Maximum production rate of elongation TF	arr1arr12 knockout	0.01	s^{-1}
d_{El}	Degradation rate of elongation TF	arr1arr12 knockout	0.0001	s^{-1}
DivElongFrac	Maximum fraction of elongation TF production that Division TF can block	arr1arr12 knockout	0.5	Dimensionless
$KM_{Div,El}$	Concentration of division TF at which it represses elongation TF to half its maximum capacity	arr1arr12 knockout	30	
PltsElongFrac	Maximum fraction of elongation TF production that PLT can block	arr1arr12 knockout	0.25	Dimensionless

(*Continued on next page*)

Please cite this article in press as: Salvi et al., A Self-Organized PLT/Auxin/ARR-B Network Controls the Dynamics of Root Zonation Development in *Arabidopsis thaliana*, Developmental Cell (2020), https://doi.org/10.1016/j.devcel.2020.04.004

Star Method Table 1. ***Continued***

Parameter	Explanation	Fit based on	Value	Dimension
$KM_{Plts,El}$	Concentration of PLT at which it represses elongation TF to half its maximum capacity	arr1arr12 knockout	20	
$KM_{ARRs,El}$	Combined ARR effect at which it induces elongation TF to half its maximum capacity	arr12 knockout	80	
Elongtreshold	Concentration of ElongTF at which cells start elongating	arr1arr12 knockout	40	

Radial Coordination of Zonation

The aim of our current study is to unravel how the longitudinal pattern of root developmental zones is controlled in a robust and self-organizing manner. In order to not further complicate our model, we ignore the additional, unresolved problem of how (approximate) radial coordination of developmental zonation across different tissue files is achieved, similar to earlier studies (see e.g. Mähönen et al., 2014)). For simplicity, we assume that cells coordinate their developmental decisions perfectly with neighboring cells in the radial direction, although this results in a more perfect synchrony amongst cell files than is experimentally observed. This coordination can be achieved in several manners, either through averaging DivTF and ElongTF across a row of neighboring cells, and using these average values to decide on the zonation status of the cells, or through using the DivTF and ElongTF levels of a particular cell type, e.g. the epidermis or vasculature, as a zonation decision criterium for all neighboring cells. We experimented with several approaches, and although simulation outcomes are qualitatively similar we found that model behaviour was most robust when taking vasculature levels as a zonation decision criterium. Analysis of our simulations revealed that in the vasculature auxin, PLT and ARR domains come in closest proximity, resulting in the sharpest boundary formation.

Cell Level Regulation

To investigate how auxin, PLT s and cytokinin signaling affect root zonation dynamics we need not only to incorporate their direct effects on zonation, as modeled via DivTF and ElongTF, but also the regulatory network through which they mutually affect one another. The network of regulatory interactions incorporated in our model is shown in STAR Method Figure 1A and is based on interactions that were previously identified in the literature as playing a role in root zonation dynamics, as well as interactions newly identified in our current study.

Auxin Signalling

We incorporate TIR1/AFB-AUX/IAA mediated transcriptional auxin signalling (Guilfoyle, 2015; Rouse et al., 1998), which we will use as a first step in auxin mediated PLT induction. Auxin signalling is modeled as in (Mähönen et al., 2014):

The interaction between auxin and PLTs is based on our previous research showing the delayed induction of PLT transcription by prolonged high auxin levels (Mähönen et al., 2014). Interestingly, PLTs in turn enhance auxin levels through inducing the auxin synthesizing YUCCA3 gene, repressing the auxin degrading GH3.3 gene as well as repressing PIN2 that functions to funnel auxin out of the meristem (Santuari et al., 2016). These interactions are also integrated into our model. Similarly, we have previously shown that ARR1 induces SHY2 and GH3.17, thereby reducing PIN levels and enhancing auxin degradation respectively (Di Mambro et al., 2017; Kumar Meena et al., 2019). Also based on existing data we incorporated the repression of SHY2 by auxin (Maraschin et al., 2009; Tian et al., 2002), and the developmentally delayed induction of ARR1 relative to ARR12 (Moubayidin et al., 2010). Based on the research described in this article we incorporated the auxin dependent induction of ARR1 and ARR12 (Figures 6A and S5C), the PLT dependent repression of ARR1 and ARR12 (Figures S4A and S4B), the ARR12 dependent repression of PLT (Figures S4H, S4I, and S4K), the ARR12 dependent induction of SHY2 (Moubayidin et al., 2010) and GH3.17 (Figure S4J). All regulatory interactions are modeled on the cell level using ODEs, and will be described in detail below.

$$\frac{dARF_{free}}{dt} = diss * (ARF_{total} - ARF_{free}) - assARF_{free} * AUX/IAA$$
$$\frac{dAUX/IAA}{dt} = P_{AUX/IAA} - d_{AUX/IAA,basal} * AUX/IAA - d_{AUX/IAA,TIR} * Auxin * AUX/IAA\ , \quad \text{(Equation 3)}$$

,where diss is the rate of dissociation of the ARF-AUX/IAA complex, ass is the rate of ARF association with AUX/IAA, $P_{AUX/IAA}$ is the production rate of AUX/IAA, $d_{AUX/IAA,basal}$ is the basal degradation rate of AUX/IAA and $d_{AUX/IAA,TIR}$ is the TIR mediated degradation rate of AUX/IAA.where we assume a constant level of total ARF. Parameter values are provided in STAR Method Table 2.

Taking a QSSA for AUX/IAA and substituting this in the equation for ARF_free gives

$$\frac{dARF_{free}}{dt} = diss * (ARF_{total} - ARF_{free}) - \frac{assARF_{free} * p_{AUX/IAA}}{d_{AUX/IAA,basal} + d_{AUX/IAA,TIR1} * Auxin} \quad \text{(Equation 4)}$$

Which can be rewritten as

$$\frac{dARF_{free}}{dt} = dissARF_{total} - \left(diss + \frac{ass * P_{AUX/IAA}}{d_{AUX/IAA,basal} + d_{AUX/IAA<TIR1} * Auxin}\right) * ARF_{free} \quad \text{(Equation 5)}$$

Please cite this article in press as: Salvi et al., A Self-Organized PLT/Auxin/ARR-B Network Controls the Dynamics of Root Zonation Development in *Arabidopsis thaliana*, Developmental Cell (2020), https://doi.org/10.1016/j.devcel.2020.04.004

Based on recent data suggesting the importance of AUX/IAA dimerisation for auxin signaling (Farcot et al., 2015; Kim et al., 1997; Korasick et al., 2014), we subsequently rewrite the latter equation to obtain a second order relation between auxin levels and free ARF levels:

$$\frac{dARF_{free}}{dt} = dissARF_{total} - \left(diss + \frac{ass * P_{AUX/IAA}}{d_{AUX?IAA,basal} + d^2_{AUX/IAA<TIR1} * Auxin^2} \right) * ARF_{free} \quad \text{(Equation 6)}$$

Star Method Table 2. ARF AUX/IAA parameters

Parameter	Explanation	Fit based on	Current value	Dimension
Ass	Association ARF to AUXIAA	Mähönen et al., 2014	0.01	s^{-1}
Diss	Dissociation ARF from AUXIAA	Mähönen et al., 2014	0.001	s^{-1}
$P_{AUX/IAA}$	Multiplied with association	Mähönen et al., 2014	0.01	s^{-1}
dIbasal	Minimum division value association ARF	Mähönen et al., 2014	0.0002	s^{-1}
DITIR1	Determines auxin contribution disassociation	arr1arr12 knockout	0.0008	$^{-1}s^{-.5}$
ARFtotal	Total ARF present in cell	Mähönen et al., 2014	100	

PLT Transcription

Our previous research indicated that PLT transcription is induced by auxin only after a prolonged period (24 hours or more) of exposure to high auxin levels (Mähönen et al., 2014). To model this delayed induction, we incorporated downstream of auxin signaling a cascade of 4 transcription factors, with the final one inducing PLT transcription, as we did in our previous model (Mähönen et al., 2014). In addition, based on our current findings we incorporate a repressive effect of ARR12 signaling on PLT transcription. We assume a saturating dependence of gene expression on the concentration of the inducing and repressing transcription factors.

$$\begin{aligned}
\frac{dA}{dt} &= \frac{pA * maxcorrection * ARF^2_{free}}{ARF^2_{free} + KM^2_{ARF,A}} - d_A * A \\
\frac{dB}{dt} &= \frac{p_B * maxcorrection * A^2}{A^2 + KM_{A,B}} - d_B * B \\
\frac{dC}{dt} &= \frac{p_C * maxcorrection * B^2}{B^2 + KM^2_{B,C}} - d_C * C \\
\frac{dD}{dt} &= \frac{p_D * maxcorrection * C^2}{C^2 + KM^2_{C,D}} - d_D * D
\end{aligned} \quad \text{(Equation 7)}$$

$$\frac{dPlts}{dt} = \frac{p_{Plts} * D^2}{D^2 + KM^2_{D,Plts}} * \frac{KM^2_{ARR12,Plts}}{ARR12^2 + KM^2_{ARR12,Plts}} - d_{Plts} * Plts \quad \text{(Equation 8)}$$

where p_A,p_B,p_C,p_D. are the maximum production rates, $KM_{ARF,A}KM_{A,B}$, $KM_{B,C}$ $KM_{C,D}$, and $KM_{D,Plts}$ are the half-maximum saturation constants, and d_A,d_B,d_C,d_D,and d_{Plts} are the degradation rates of A, B, C, D and PLT respectively. Parameter values are given in STAR Method Table 3.

As a side effect of using a cascade of factors each depending in a saturating manner on the previous one, each subsequent factor is reaching lower levels for a given auxin input. We compensate for this by using a factor maxcorrection, that ensures that for high auxin levels all factors in the cascade are still capable of reaching their maximum transcriptional level.

Star Method Table 3. ABCD TF cascade parameters

Parameter	Description	Fit based on	New	dimension
$P_{A,B,C,D}$	Max production of ABCD TFs	Re-evaluation Mähönen et al., 2014	0.0065	$*s^{-1}$
d_{ABCD}	Decay rate of ABCD TFs	Re-evaluation Mähönen et al., 2014	0.000065	s^{-1}
$KM_{ARF,A}$	Arf km for B production	Re-evaluation Mähönen et al., 2014	55	
$KM_{A,B}$	A km for B production	Re-evaluation Mähönen et al., 2014	55	
$KM_{B,C}$	B km for C production	Re-evaluation Mähönen et al., 2014	55	
$KM_{C,D}$	C km for D production	Re-evaluation Mähönen et al., 2014	55	
Maxcorrection	Corrects A-D for full activation capacity	Re-evaluation Mähönen et al., 2014	1.3025	Dimensionless

Please cite this article in press as: Salvi et al., A Self-Organized PLT/Auxin/ARR-B Network Controls the Dynamics of Root Zonation Development in *Arabidopsis thaliana*, Developmental Cell (2020), https://doi.org/10.1016/j.devcel.2020.04.004

Additional PLT Dynamics

PLT Growth Dilution

A key difference between this model and the one described in (Santuari et al., 2016) from the (Mähönen et al., 2014) study is that here we take cytoplasmic growth induced dilution of protein levels fully into account. In the original Mähonen model, assuming that transcription factors predominantly reside in the nucleus, and ignoring nucleus growth, we assumed less dilution for TF than non-TF protein. However, since nuclei in fact do grow proportionally to cells, TF will undergo similar dilution effects as non-TF. For most transcription factors the production and degradation speeds are relatively fast, enabling them to rapidly recover from cellular growth dependent dilution. However, for the stable, slowly turning over PLT proteins, this dilution likely has a substantial effect on protein concentration levels.

To determine the rate of cellular growth induced dilution on PLT levels, we write the following equation:

$$dilutionrate = 1 - (0.5)^{\left(\frac{1}{(10 * 3600)}\right)} = 0.0000192539 \quad \text{(Equation 9)}$$

This equation can be understood as follows. We know that in the process of cell growth preceding cell division, cell and nuclear volumes double and hence protein levels are halved. Based on the cell division duration of 10 hours applied in our model, this halving of concentrations takes 10 hours or 10*3600 seconds. For the remaining 50% of proteins we can thus write *r*emaining fraction per 10 *hours* $= 0.5 = x^{(3600*10)}$, where x is the retention rate per second. Thus. $x = 0.5^{\frac{1}{3600*10}}$ Since the dilution rate is the loss rate, or what is not retained per second, we finally obtain it as1 minus thisretention rate. We thus find that the rate at which PLT protein concentration levels decline due to dilution (0.0.0000192539) is roughly on par with its degradation rate (see STAR Method Table 4). Additionally, the domain of PLT protein production (i.e. the region of PLT gene expression, which is centred around the QC) is relatively small compared to the overall protein domain (the entire meristem). In order for the small stem cell niche to stock the cells with sufficient protein to last through several rounds of division before they leave the transcription domain, we had to increase the production rate to 5 times the value used in (Mähönen et al., 2014).

It is noteworthy that the small domain of maximum PLT transcription is centred around the QC, and thus encompasses the most slowly dividing, and hence least growth dilution experiencing cells. This property is key to enable a small source of PLT producing cells to maintain a stable, extended PLT gradient.

PLT Movement

Importantly, effective PLT displacement, and the effect it can have on meristem size, is a result of both the rate at which PLT s move through plasmodesmata and the PLT concentration gradient driving PLT motility. As explained above, to compensate for the growth induced dilution of PLT proteins, we substantially enhanced maximum PLT expression levels, resulting in a steeper PLT concentration gradient. The lower cell-to-cell motility rate combined with the steeper PLT gradient together give rise to a similar sized effect of PLT motility on meristem size as in our previous model.

PLT Removal in Bottom Columella Cells

In planta, columella and root cap cells continuously slough off and are replaced by newer cells. However, in our model, growth, replacement and loss of columella cells is not incorporated (for lateral root cap cells it is). Because of the slow PLT turnover dynamics, absence of columella cell growth and division (causing PLT dilution) and detachment (causing PLT loss) leads to the artificial accumulation of PLT protein in the columella. To prevent this, we added an additional PLT decay term to the lowermost columella cells. While this measure is effective in preventing the artificial accumulation of PLT in the entire columella, this does drastically reduce PLT levels particularly in the lowermost columella cells. As a consequence, in our model ARR expression is repressed less in these cells than one would expect based on experimental data (see eg Figures 2B and 3C).

In our previous study we established that PLT proteins move from cell to cell through plasmodesmata and that this process contributes to PLT gradient formation (Mähönen et al., 2014). In absence of direct measurement data, we derived the rate for PLT motility in that study by fitting the amount of decrease in meristem size when blocking (reducing) PLT cell-to-cell movement in the model with our experimental data. However, applying the same motility rate for PLT in our current model would lead to PLT gradient collapse due to the far greater source (PLT producing cells) to sink (non PLT producing cells to which PLT proteins may move) mismatch in our current model. This source-sink mismatch increased both due to a decrease in source size -the QC-centered area of PLT producing cells in our realistic root tip topology is smaller than in a squared root topology-, as well as an increase in sink size -the non- PLT producing but PLT receiving cells now also encompass a lateral root cap and larger columella. As a consequence, under the PLT motility rates applied previously, the PLT producing cells would simply "bleed out" and be incapable of maintaining high PLT levels. To prevent this, we applied a 50 times reduced PLT cell-to-cell motility rate, necessary to ensure that the PLT producing cells around the QC do not export more PLT than they can produce. In addition, to reproduce the experimental observation that PLT levels in neighboring cell files differ significantly, implying that these differences are not smoothened out through pronounced radial PLT movement, we decreased PLT motility through radially oriented plasmodesmata with a further factor of 10. Similar ratios for longitudinal and transversal plasmodesmatal connectivity have been previously reported ((Burch-Smith et al., 2011))

Please cite this article in press as: Salvi et al., A Self-Organized PLT/Auxin/ARR-B Network Controls the Dynamics of Root Zonation Development in *Arabidopsis thaliana*, Developmental Cell (2020), https://doi.org/10.1016/j.devcel.2020.04.004

Star Method Table 4. PLT parameters

Parameter	Description	Fit based on	Current value	Dimension
p_{Plts}	Max PLT production	Re-evaluation Mähönen et al., 2014	0.00875	$*s^{-1}$
d_{Plts}	PLT degradation	Mähönen et al., 2014	0.0000175	s^{1}
$KM_{D,Plts}$	DD Km half max production	Re-evaluation Mähönen et al., 2014	60	
Pltsdiff	PLT diffusion across membrane	Re-evaluation Mähönen et al., 2014, arr1arr12 knockout	0.0000534	s^{1}

CK Signaling

Cytokinin has a major impact on root developmental zonation, yet modeling its impact on root zonation dynamics has so far remained problematic. First, the locations of cytokinin production and perception show limited overlap, with cytokinin production predominantly occurring in the root tip and lateral root cap (Miyawaki et al., 2004), yet cytokinin perception has been demonstrated to be around the transition and early elongation zone as indicated by the expression patterns of ARRs (Moubayidin et al., 2010; Muraro et al., 2016). As a consequence, modeling cytokinin levels as a proxy for cytokinin signaling is insufficient to explain root zonation patterning (Moore et al., 2015; Muraro et al., 2016; Rutten and Ten Tusscher, 2019). For this reason, focusing instead on the patterning and activity of cytokinin response factors has proven to be a more fruitful approach (Di Mambro et al., 2017; Rutten and Ten Tusscher, 2019), which we also adopted in the current study. However, the location of cytokinin signaling has been statically superimposed in previous models, precluding the use of these models to study self-organized dynamic patterning of auxin and cytokin domains. Therefore, in the current study, we let the levels and location of the cytokinin signaling mediating ARRs be dynamically regulated.

Based on findings in our current study (Figures 5A, 5B, 6A, and 6B) we model the auxin dependent induction and PLT dependent repression of ARR12 and ARR1. While ARR12 mediated cytokinin signaling is present from early stages of root development, ARR1 signaling becomes fully active only at 5dpg (Moubayidin et al., 2010).The initial repression of ARR1 is mediated by giberellin, which levels are high prior to germination and decline over the course of development (Curaba et al., 2004; Moubayidin et al., 2010). We simulate this in our model using a time dependent repressor for ARR1 (Equation 10, $timeREP_{ARR1}$). Up until 3 dpg, this repression is fully active, after which it gradually releases its repressive effect until it is completely gone at 4.5 dpg. This allows ARR1 to have some time to become fully active at 5 dpg.

$$\frac{dARR_1}{dt} = \frac{p_{ARR1} * Auxin^2}{Auxin^2 + KM^2_{Auxin,ARR1}} * \frac{TimeREP_{ARR1} * KM^2_{Plts,ARR1}}{Plts^2 + KM^2_{Plts,ARR1}} - d_{ARR1} * ARR1_1$$

$$TimeREP_{ARR1} = min\left(1, max\left(0, \frac{(tpg - ARR1esxpressionstart)}{(ARR1maximumeffect - ARR1expressionstart)}\right)\right), \quad \text{(Equation 10)}$$

where p_{ARR1} is the maximum ARR1 production rate, $KM_{Auxin,ARR1}$ the concentration of auxin at which ARR1 production is half maximum, tpg is the time post germination (developmenntal time) in seconds, ARR1expressionstart is the time at which ARR1 expression starts (i.e. GA levels start declining), ARRmaximumeffect is the time at which ARR1 becomes fully active (i.e. GA levels have reached a minimum level), $KM_{Plts,ARR1}$ is the PLT concentration for which ARR1 production is repressed to half its maximum and d_{ARR1} is the ARR1 degradation rate.

$$\frac{dARR_{12}}{dt} = p_{ARR12} * \frac{\text{Auxin}^2}{Auxin^2 + KM^2_{Auxin,ARR12}} + \frac{KM^2_{Plts,ARR12}}{Plts^2 + KM^2_{Plts,ARR12}} - d_{ARR12} * \text{ARR12}\,, \quad \text{(Equation 11)}$$

where p_{ARR12} is the maximum ARR12 production rate, $KM_{Auxin,ARR12}$ the concentration of auxin at which ARR12 production is half maximum $KM_{Plts,ARR12}$ is the PLT concentration for which ARR12 production is repressed to half its maximum and d_{ARR12} is the ARR12 degradation rate.

The ARR12 and ARR1 parameter values provided below are the default values, and are used in all simulations unless explicitly stated otherwise. Alternative parameter settings used in certain simulations are discussed in the hypothetical scenario section. All parameters not mentioned in that section maintain their default values.

Star Method Table 5. ARR1 Parameters

Parameter	Description	Fit based on	Current value	Dimension
p_{ARR1}	Maximum ARR1 production rate	wt	0.02	s^{-1}
d_{ARR1}	ARR1 degradation rate	wt	0.0002	s^{-1}
$KM_{Auxin,ARR1}$	Auxin level at which ARR1 production is induced to half maximum	arr12 knockout	160	

(*Continued on next page*)

Please cite this article in press as: Salvi et al., A Self-Organized PLT/Auxin/ARR-B Network Controls the Dynamics of Root Zonation Development in *Arabidopsis thaliana*, Developmental Cell (2020), https://doi.org/10.1016/j.devcel.2020.04.004

Star Method Table 5. ***Continued***

Parameter	Description	Fit based on	Current value	Dimension
$KM_{Plts,ARR1}$	PLT level at which ARR1 production is repressed to half maximum	arr12 knockout	30	
ARR1expressionstart	runtime when ARR1 starts being expressed	arr12 knockout	259200(3dpg)	s
ARR1fullexpression	Runtime from when ARR1 is fully active	arr12 knockout	388800(4.5dpg)	s
ARR1maximumeffect	Multiplication of ARR1 relative to ARR12 effect	wt,arr1 knockout, arr12 knockout, arr1arr12 knockout	2	dimensionless

Star Method Table 6. ARR12 parameters

Parameter	Description	Fit Based on	Current value	Dimension
p_{ARR12}	Maximum ARR12 production rate	wt	0.02	s^{-1}
d_{ARR12}	ARR12 degradation rate	wt	0.0002	s^{-1}
$KM_{Auxin,ARR12}$	Auxin level at which ARR12 production is induced to half maximum	Arr12 seperate effect tests	175	
$KM_{Plts,ARR12}$	PLT level at which ARR12 production is repressed to half maximum	ARR12 separate effect tests	30	
$KM_{ARR12,Plts}$	ARR12 level at which PLT production is reduced to half its maximum	ARR12 separate effect tests	25	
ARR12Pltsrepressfrac	Maximum fraction of PLT repression by ARR12	ARR12 separate effect tests	1.0	dimensionless

Auxin Production

Production of auxin occurs in all intra-cellular gridpoints at a basal rate. Additionally, since our study focuses at the interactions between auxin, PLT and cytokinin, we incorporated additional auxin production that depends on the expression of the PLT inducible YUCCA3 (Santuari et al., 2016), which catalyzes a rate limiting step in auxin metabolism. We model YUCCA3 expression as:

$$\frac{dYUC3}{dt} = \frac{p_{YUC3} * Plts^2}{Plts^2 + KM^2_{Plts,YUC3}} - d_{YUC3} * YUC3\ , \qquad \text{(Equation 12)}$$

where p_{Yuc} is the maximum YUCCA3 production rate, $KM_{Plts,YUC3}$ is the PLT value for which YUCCA production is half maximum and d_{Yuc3} is the YUCCA3 degradation rate.

STAR Method Table 7. YUCCA parameters

Parameter	Description	Fit based on	Current value	Dimension
p_{YUC3}	Maximum YUCCA production rate s^{-1}	Re-evaluation Mähönen et al., 2014	0.03	s^{-1}
d_{YUC3}	Yucca degradation rate s^{-1}	Re-evaluation Mähönen et al., 2014	0.0003	s^{-1}
$KM_{Plts,YUC3}$	Yucca production PLT KM	arr1arr12 knockout	175	
Ap_{YUC}	Yucca based auxin production rate	arr1arr12 knockout	0.0015	

Auxin Degradation

Auxin is degraded in all intra-cellular grid points at a basal rate. Additional auxin degradation occurs dependent on the level of expression of two auxin degrading GH enzymes, GH3.3 that is repressed by PLT (Santuari et al., 2016) and the previously identified GH3.17 that is induced by CK signaling and expressed specifically in the lateral root cap and epidermis (Di Mambro et al., 2017) GH3.3 and GH3.17 expression is modeled as

$$\frac{dGH33}{dt} = \frac{p_{GH33} * KM^2_{Plts,GH33}}{Plts^2 + KM^2_{Plts,GH33}} - d_{GH33} * GH33 \qquad \text{(Equation 13)}$$

$$\frac{dGH317}{dt} = \frac{p_{GH317} * ARRs_{eff}}{ARRs^2_{eff} + KM^2_{ARRs,GH317}} - d_{GH317} * GH317\ , \qquad \text{(Equation 14)}$$

Please cite this article in press as: Salvi et al., A Self-Organized PLT/Auxin/ARR-B Network Controls the Dynamics of Root Zonation Development in *Arabidopsis thaliana*, Developmental Cell (2020), https://doi.org/10.1016/j.devcel.2020.04.004

with p_{GH33} and p_{GH317} as the maximum production rates of GH3.3 and GH3.17 respectively, d_{GH33} and d_{GH317} as the degradation rates of GH3.3 and GH3.17 respectively. $KM_{Plts,GH33}$ is the PLT concentration for which GH33 production is repressed to half its maximum. Finally $KM_{ARRs,GH317}$ is the combined ARR effect level for which GH317 production is at half maximum.

Star Method Table 8. GH parameters

Parameter	Description	Fit based on	Current value	dimension
p_{GH33}	Maximum GH3.3 production rate	Re-evaluation Mähönen et al., 2014	0.03	s^{-1}
d_{GH33}	GH3.3degradation rate	Re-evaluation Mähönen et al., 2014	0.00003	s^{-1}
$KM_{PltsGH33}$	PLT level at which GH3.3 production is half maximum	Re-evaluation Mähönen et al., 2014	100 (plts)	
Ad_{Gh33}	GH3.3 based auxin degradation per GH3.3(a.u.)	Re-evaluation Mähönen et al., 2014	$1.45*10^{-7}$	$Dimensionless^{-1}$
p_{GH317}	Maximum GH3.17 production rate	Re-evaluation Mähönen et al., 2014	0.03	s^{-1}
d_{GH317}	GH3.17 degradation rate	Re-evaluation Mähönen et al., 2014	0.0003	s^{-1}
$KM_{ARRs,GH317}$	ARR level at which GH3.17 production is half maximum	ARR12 separate effect tests,arr1 knockout	75	
Ad_{GH317}	GH3.17 based auxin degradation per GH3.17(a.u.)	ARR12 separate effect tests, arr12 knockout	$1.16*10^{-6}$	

Auxin Import

In addition to a baseline passive auxin import rate, influx of auxin from the apoplast into the cell is enhanced by the presence of AUX/LAX auxin importers Similar to our previous study (van den Berg et al., 2016) we incorporated the auxin dependent expression of AUX1 as follows:

$$\frac{dAUX1}{dt} = \frac{p_{AUX1} * Auxin^2}{Auxin^2 + KM^2_{Auxin,AUX1}} - d_{AUX1} * AUX1\ , \qquad \text{(Equation 15)}$$

where p_{AUX1} is the maximum AUX1 production rate and d_{AUX1} is the AUX1 degradation rate. $KM_{Auxin,AUX1}$ this the auxin level fro which the AUX1 production is half maximum.

Star Method Table 9. AUX1 parameters

Parameter	Description	Fit Based on	Current Value	Dimension
aux1fac	Aux1 influx strength	Mähönen et al., 2014	0.21	Dimensionless
p_{AUX1}	Aux1 maximum production	Mähönen et al., 2014	0.01	s^{-1}
$KM_{Auxin,AUX1}$	Aux1 production half saturation value for auxin	Mähönen et al., 2014	50	
decay_aux1	Aux1 degradation	Mähönen et al., 2014	0.0001	s^1

Auxin Export

Auxin only leaves cells through active export. A major determinant of active auxin export are the polarly localised PIN transporters. In our model we incorporate the dynamic regulation of PIN1, which has an endodermal and vascular expression pattern and predominantly basal orientation, and PIN2 which is expressed in the lateral root cap, and epidermis where it has a predominant apical orientation, and in the cortex where orientation switches from basal to apical as cells move from the meristem to the elongation zone (Figure 3A). We incorporate for both PIN1 and PIN2 the SHY2 mediated repression downstream of ARR1 and ARR12, taking int account the previously reported stronger effect of ARR1 (Moubayidin et al., 2010), as well as the auxin dependent repression of SHY2 counteracting this effect. Additionally, for PIN2 we incorporate its PLT dependent repression (Santuari et al., 2016) for simplicity, other PIN types (PIN3, and PIN7 in the collumella) are kept constant.

$$\frac{dPIN1}{dt} = p_{PIN} * SHY2_{reg} - d_{PIN} * PIN1$$

$$\frac{dPIN2}{dt} = p_{PIN} * SHY2_{reg} * Plts_{reg} - d_{PIN} * PIN1$$

$$SHY2_{reg} = 1 - \left(PIN_{ARRs} \frac{fac * KM^2_{ARRs,PINs}}{ARRs^2_{eff} * KM^2_{ARRs,PINs}} \right) * Auxin_{regSHY2}$$

$$ARRs_{eff} = ARR1 * ARR1maximumeffect + ARR12$$

$$Auxin_{regSHY2} = 1 - \frac{Auxin^2}{Auxin^2 + KM^2_{Auxin,SHY2}}$$

$$Plts_{reg} = \left(1 - PIN2_{Plts}fac + \frac{PIN2_{Plts}fac * KM_{Plts,PIN2}}{Plts^2 * KM^2_{Plts,PIN2}} \right),$$

(Equation 16)

where p_{PIN} is the maximum PIN production rate and d_{PIN} is the PIN degradation rate for both PIN1 and PIN2. $KM_{ARRs,PINs}$ is the combined ARR effect value for which the ARR PIN repression effect is half maximal, $KM_{Auxin,SHY2}$ is the auxin level at which the ARR effect is repressed to half its value and $KM_{Plts,PIN2}$ is the PLT value for which PIN2 is repressed to half of the remaining value. $PIN_{ARRs}fac$ is the maximum factor by which PIN1 and PIN2 can be repressed by ARRs and $PIN2_{Plts}fac$ is the maximum factor by which PLT can repress PIN2.

Star Method Table 10. Efflux parameters

Parameter	Description	Fit based on	Current value	Dimension
pPUMP	PIN efflux strength	Mähönen et al., 2014	0.2	dimensionless
p_{PIN}	PIN maximum production	Mähönen et al., 2014	0.01	s^{-1}
d_{PIN}	PIN degradation	Mähönen et al., 2014	0.0001	s^{-1}
Pin1regfac	Fraction pin 1 upregulation under PLT	arr1arr12 knockout	0.0	0.0
$PIN2_{Plts}fac$	Fraction PIN2 downregulation under PLT	arr1arr12k nockout	0.7	0.7
$KM_{Plts,PIN2}$	Km of PIN2 downregulation by PLT	Arr1arr12 knockout	80	
$PIN_{ARRs}fac$	Fraction pin downregulation under ARR(via SHY2)	ARR12 separate effect tests,arr12 knockout	0.3	dimensionless
$KM_{ARRs,PINs}$	Km of PIN(s) downregulation by ARR	ARR12 separate effect tests,arr12 knockout	75	
$AuxinKM_{SHY2}$	Km of repression auxin repression of SHY2	arr1 knockout	225	

Auxin Dynamics

Auxin dynamics are modeled on the grid level, enabling the simulation of intracellular and intra-apoplast auxin gradients. Local changes in auxin levels are governed by auxin production and degradation, import into and export from cells and diffusion inside cells and apoplast and are described using the following differential equation:

$$\frac{\partial Auxin}{\partial t} = Ap_b + Ap_{YUC} * YUC_3 - (Ad_b + Ad_{GH33} * GH33 + Ad_{GH317} * GH317) * Auxin_{ij} + \sum_{i,j} \left((i_{pas} + i_{act*AUX1_{ij}}) * Auxin_{i'j'} \right) - \sum_{i,j} \left((e_{pas} + e_{act*PIN_{ij}}) * Auxin_{i,j} \right) + D \left(\frac{\partial^2 Auxin}{\partial^2 x} + \frac{\partial^2 Auxin}{\partial^2 y} \right),$$

(Equation 17)

where Ap_b is a baseline, per grid point auxin production, which for QC, columella, and LRC cells is multiplied by a factor, 50,25 and 12, respectively to incorporate elevated auxin production in these cells (see also section on Tissue architecture and Figure 3A). Ap_{YUC} is the YUCCA3 dependent auxin production in YUCCA3 expressing cells, Ad_b is the basal degradation rate, Ad_{GH33} is the GH3.3 mediated degradation and Ad_{GH317} is the GH3.17 mediated degradation in the epidermis and LRC.

At the interface between cell wall grid points and neighboring cellular grid points passive influx i_{pas} as well as active AUX1 mediated import of auxin $i_{act*AUX_{ij}}$ takes place. Here, $AUX1_{ij} = AUX1Prepat_{ij} * AUX1$ where AUX1Prepat represents the predefined cell and zonation type dependent AUX1 expression pattern (Figure 3A), while AUX1 represents the dynamically regulated concentration of AUX1(Equation 15) in the corresponding cell.

At this same interface auxin export also occurs. Due to the deprotonation of auxin inside cells no passive export of auxin occurs. Active auxin export is mediated through several families of transporters, with a dominant role for the polarly localised PIN proteins (Wisniewska et al., 2006)

(Wisniewska et al., 2006) In our model we consider both a constant active export mediated by ABCB transports e_{bas} As well as an active, PIN mediated export, $e_{act*PIN_{ij}}$. Similar as for AUX1, here PIN_{ij} = $PINxPrepat_{ij}$ * PINx+$PINxPrepat_{ij}$ * PINx where. PINxPrepat represents the predefined cell and zonation dependent PIN expression pattern of the relevant PIN type (Figure 3A) and PINx represents the dynamically regulated concentration of the relevant PIN type (Equation 16) and PINxPrepat are predetermined according to cell file and zone as seen in Figure 3A and explained earlier in the *spatial layout* section. Auxin production and degradation occur only in intracellular grid points, auxin import and export occurs only between pairs of adjoining cell wall and cell membrane grid points, and auxin diffusion is limited to occur between adjoining cell or adjoining wall grid points.

Star Method Table 11. Basic Auxin parameters

Parameter	Description	Fit based on	value	Dimension
APb_b	basal Auxin production	arr1arr12 knockout	0.003	s^{-1}
Inf	Auxin level shoot influx	Mähönen et al., 2014	0.8	
Ad_b	Basal degradation	Re-evaluation Mähönen et al., 2014	0.000058	s^{-1}
DauxC	Auxin diffusion in cell	Mähönen et al., 2014	600	$\mu m^2 s^{-1}$
DauxW	Auxin diffusion in wall	Mähönen et al., 2014	40	$\mu m^2 s^{-1}$
eff	Passive auxin efflux	Mähönen et al., 2014	1	$\mu m s^{-1}$
InAux	Passive auxin influx	Mähönen et al., 2014	2.5	$\mu m s^{-1}$

Initial Conditions

Since we are interested in explaining the setting up, growth and stabilisation of the root meristem, we model root meristem dynamics from directly post-germination onwards. Therefore, we start our simulations with an initial root tip topology as shown in STAR Method Figure 1B fourth figure, consisting of a columella, lateral root cap and small root tip meristem containing 7 rows of meristematic cells. In addition, we incorporate the hypocotyl-radicle junction, the tissue connecting the embryonic root and shoot tissues, which in our model consists of 5 rows of cells. Finally, 8 rows of buffer cells, not corresponding to any real embryonic plant tissue are incorporated to ensure that the boundary of the simulated tissue (where exchange of auxin with the not explicitly modeled shoot occurs) resides at a sufficiently large distance from the meristem also at early developmental stages. This is necessary to ensure that early on no auxin patterning artifacts occur from not simulating the complete plant. In absence of any detailed data we assume that PIN and AUX/LAX patterns are similar to adult meristem patterns from germination onwards. For hypocotyl-radicle junction and buffer cells PIN and AUX/LAX patterns identical to those used in the elongation zone of a more mature root were used.

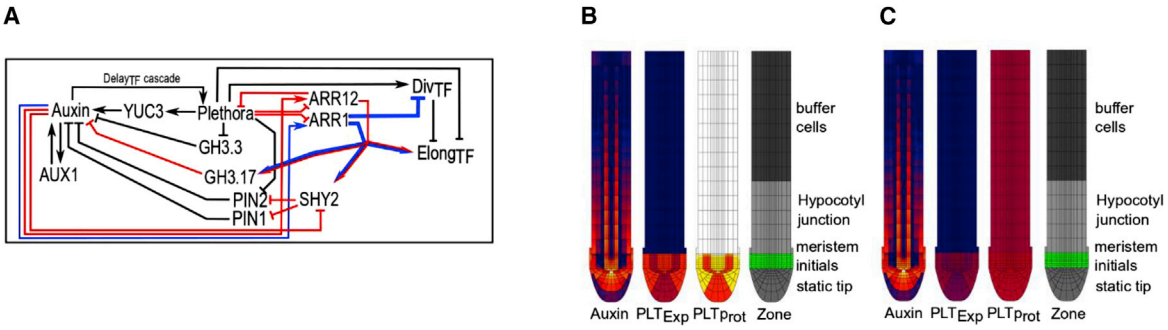

Star Method Figure 1:

(A) Overview of the final network of regulatory interactions incorporated in the model. In black are the interactions corresponding to a simulated arr1 arr12 double knockout plant, based on interactions previously incorporated in the (Mähönen et al., 2014) paper as well as more recent data. These interactions form the initial model used for the first step of parameter fitting. In red are the additional interactions present in plants expressing ARR12, based on both previous experimental data as well as findings in the current manuscript. Black and red interactions together correspond to the situation in an arr1 single knockout plant. Finally, in black are the additional interactions arising from the presence of ARR1, again based on previous data as well as this manuscript. Black, red and blue interactions together represent the wild type situation.

(B) Initial state of auxin levels, PLT expression, PLT protein levels, and root zonation from which simulations are started (1hpg). At the start, in silico tissue topology consists of root cap and columella (grey), a small meristem (green, 7 rows of cells), a hypocotyl radicle junction (light grey, 5 rows of cells), and 8 rows of buffer cells (rightmost picture). Auxin fluxes in from the shoot and quickly forms gradients. At the start of our simulations, we imposed an I intermediate levels of PLT expression (55) and protein level (125) throughout the meristem, with somewhat lower levels (40 and 75, respectively) applied in the cortex, endodermis and columella to prevent excessive auxin accumulation. Additionally, we imposed an initial high level (250) of PLT proteins in the hypocotyl-radicle junction and buffer cells (250).

(C) Alternative initial conditions with lower PLT expression and protein levels. In the vasculature, pericycle, epidermis, lateral root cap and QC, PLT expression is 30 and initial PLT protein level is 65. In the endodermis, cortex and columella PLT expression is 20 and PLT protein levels are 50. In the hypocotyl junction PLT protein is reduced to 65 as well.

Please cite this article in press as: Salvi et al., A Self-Organized PLT/Auxin/ARR-B Network Controls the Dynamics of Root Zonation Development in *Arabidopsis thaliana*, Developmental Cell (2020), https://doi.org/10.1016/j.devcel.2020.04.004

Model Construction and Parametrization

Above we described all components and regulatory interactions incorporated in the final model we developed here. Obviously, this model is highly complex and involves a large number of parameters. Determining all these parameters by fitting to experimental observations is a daunting task that may easily lead to non-unique, non robust and/or non biologically meaningful parameter settings. To determine biologically meaningful parameter values and ensure that model outcomes do not critically depend on exact parameter values but rather remain qualitatively the same and quantitatively very similar when varying them over a limited range, we reduced the parameter fitting problem by building up our model in an incremental manner, starting from the smallest number of relevant variables and parameters and gradually extending from there.

Step 1: An Auxin-PLT Model Simulating the arr1,arr12 Double Mutant

We take the ARR1-ARR12 double mutant roots as our starting point, thus removing not only two model variables but also a large number of interactions (Star Method Figure 1A black interactions). This starting model basically has the same regulatory complexity as the Mähönen et al., 2014 model. Parameters relating to auxin import, export and diffusion rates, the delayed auxin dependent induction of PLT, PLT stability, and baseline auxin production and degradation rates were taken from this model (indicated in Star Method Tables 2, 4, and 9–11 with Mähönen et al., 2014). A subset of these parameters were adjusted to compensate for changes in tissue topology (see section on PLT cell to cell movement) and modeling assumptions (see section on growth dilution of PLT necessitating enhanced maximum transcription rates) (indicated in Star Method Tables 3, 4, 7, 8, and 11 with Re-evaluation Mähönen et al., 2014).

Remaining parameters in this initial model are the maximum PLT dependent induction of YUCCA3, repression of GH3.3 and PIN2, and auxin dependent induction of AUX1, saturation constants for these regulatory interactions, turnover of these proteins, and the effect of YUCCA3 and GH3.3 on auxin production and degradation (indicated in Star Method Tables 1, 2, 7, 10, and 11 with arr1arr12 knockout). Additionally, since zonation dynamics are now governed by DivTF and ElongTF, we needed to parametrize the effects of PLTs on these factors (Equations 1 and 2)

Parameters were fitted to reproduce the experimentally observed meristem size growth dynamics for arr1,arr12 double mutants while maintaining a normal, QC-focussed auxin gradient. As an additional constraint, the experimentally measured PLT gradient should be reproduced at each time point. The in vivo PLT gradients shown in Figures 4A and S5A were obtained in roots that had higher PLT expression than wild type and arr12 respectively owing to their YFP bound copy of PLT2. In accordance with our prediction the roots of these experiments had slightly enlarged meristems. Star Method Figure 2 shows that there is also a consistent PLT level at the actual TZ in these roots, both in *PLT2:YFP wild type* (Star Method Figure 2A) and in *PLT2:YFP arr12-1* (Star Method Figure 2B).

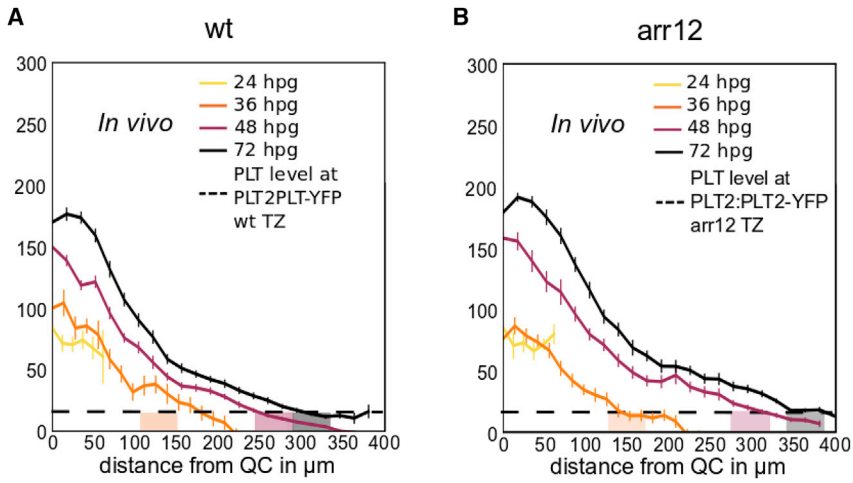

Star Method Figure 2:

(A) Same PLT2: YFP fluorescence quantification as in Figure 3A, but now indicating with light shaded boxes the TZ locations observed in PLT2:YFP (wild type background) instead of wild type roots, and indicating with a dashed line the PLT threshold level corresponding to these TZ positions (Students T test shows consistent PLT2 levels at the TZ at 48 and 72 hpg ($p > 0.1$) PLT2 at 36 hpg is significantly different from both 48 and 72 hpg with $p<0.01$ due to a bias introduced by only the largest meristems reaching those lengths at 36 hpg). Comparison with Figure 3A indicates that due to the additional PLT2 copy, the TZ is shifted shootward in PLT2:PLT2-YFP (wild type background) relative to wild type, resulting in a lower estimated, yet still consistent PLT2 threshold.

(B) Same PLT2:PLT2-YFP fluorescence quantification as in Figure S5A, but now indicating with light shaded boxes the TZ locations observed in PLT2:PLT2-YFP arr12-1 instead of arr12-1 roots. and indicating with a dashed line the PLT threshold level corresponding to these TZ positions (Students t test between PLT levels at TZ zone position at 36,48, and 72 hpg cross comparison all $p>0.5$ indicating absence of significant differences). Comparison with Figure 5A indicates that due to the additional PLT2 copy, the TZ is shifted shootward in PLT2:YFP arr12-1 relative to arr12, again resulting in a lower estimated, yet consistent PLT threshold. Note that this PLT threshold level is consistent with the one obtained in A.

Please cite this article in press as: Salvi et al., A Self-Organized PLT/Auxin/ARR-B Network Controls the Dynamics of Root Zonation Development in *Arabidopsis thaliana*, Developmental Cell (2020), https://doi.org/10.1016/j.devcel.2020.04.004

Additionally, since zonation dynamics are now governed by DivTF and ElongTF, we needed to parametrize the effects of Additionally, since zonation dynamics are now governed by DivTF and ElongTF, we needed to parametrize the effects of PLTs on these factors (Equations 1 and 2) on these factors (Equations 1 and 2) gradients during the first 72 hours of development in the arr12 single mutant were used. Since these measurements were performed well before the 5dpg at which ARR1 becomes active, Additionally, since zonation dynamics are now governed by DivTF and ElongTF, we needed to parametrize the effects of PLTs on these factors (Equations 1 and 2) dynamics of the arr12 mutants should be similar to those of arr1,arr12 double mutant at these time points. This combination of meristem size and PLT gradient data enables us to infer both the parameters governing the dependence of zonation factors DivTF and ElongTF on PLT levels, as well as the parameters governing auxin PLT interactions. We find that to allow a small embryonic root meristem just after germination to grow into the large meristems observed for mature roots, the auxin-PLT positive feedback loop from the auxin induced PLT transcription and the PLT induced enhancement of auxin production and reduction of auxin degradation needs to be sufficiently strong. Although substantially constrained, the obtained the parameter settings for the various feedbacks of auxin production and degradation are not entirely unique. As an example, to some extent it is possible to enhance YUCCA based auxin production to compensate for an increased Km value for PLT induced YUCCA expression. On a similar note, a reduction in the PLT mediated increase in auxin production can be compensated for with an increase in the PLT mediated repression of auxin degradation.

Step 2: Tuning Initial Conditions

Upon starting our simulations on the initial root tip layout illustrated in Star Method Figure S1Bs fourth panel, auxin gradients rapidly become established. In contrast, due to the slow induction of PLT expression by auxin, PLT expression and protein domains take substantially longer to become established if we were to start from zero PLT expression and protein levels. Based on the experimentally determine PLT protein gradient at 24hpg, we derive that intermediate levels of PLT expression and protein (Star Method Figure 1Bs second and third panel) need to be present in the incipient root meristem prior to seed germination, in order for these 24hpg patterns to be formed. Consistent with the lower PLT levels we observe in cortex and endodermal cells in simulated later stage, mature meristems (see for example Figure 6A), we found that initial levels in these cell types also needed to be lower to also reproduce realistic initial auxin patterns.

This initial condition basically reflects the assumption that during embryogenesis, PLT expression and proteins domains have been formed, and that during seed dormancy at least a certain level of expression and protein is maintained. We subsequently confirmed this assumption experimentally (Figure 2A) Note that these levels are only imposed as an initial condition. As soon as the model is running PLT expression and protein levels are free to evolve based on local and surrounding auxin, cytokin signalling and PLT levels.

Additionally to imposing PLT expression and proteins in the meristem, we also imposed an initial high level of PLT proteins (but not expression) in the hypotocyl-radicle juntion and buffer cells (Star Method Figure 1Bs third figure),. This effectively prevents these tissues from forming a major sink for the motile PLT protein. Otherwise, such a major sink would prevent PLT gradient formation and meristem activation. This condition effectively implies that prior to seed germination PLT expression in the meristem has led to a buildup of PLT protein also outside the meristem. As an alternative to assuming high PLT protein levels in these extra meiristematic tissues one could also assume limited plasmodesmatal connectivity between these tissues and the meristem, this would give similar outcomes. We assume that hypocotyl-radicle junction cells (and buffer cells) do not express PLT or ARR production.

Step 3: An Auxin-PLT-ARR12 Model Simulating the arr1 Mutant

Having established a baseline auxin-PLT model for the arr1,arr12 double mutant situation, we next extend our model to incorporate the antagonistic effects of ARR12-mediated CK signalling on root growth dynamics. This means that we effectively are modeling an arr1 mutant. Our study indicates that, similar to ARR1, ARR12 reduces auxin signalling levels via GH3.17 mediated auxin degradation as well as SHY2 mediated repression of the auxin exporting PINs (Equation 16). Additionally, we identified a mutual repression between PLTs and ARR12, as well as ARR12 expression being auxin dependent (Figures 5A, 5B, 6A, and 6B; Equations 8, 10, and 11; red colour in Figure S1A). Finally, based on the known promoting effect of cytokinin on cell differentiation, we incorporated a positive effect of ARR12 on the ElongTF governing the transition to elongation and differentiation (Equation 2).

Parameter settings for the added regulatory interactions (indicated with ARR12 separate effects tests in Star Method Tables 6, 8, and 10) were obtained by fitting model behavior to the experimentally observed meristem growth dynamics. A key characteristic of meristem growth dynamics in the arr1 (purple line in Figure 7A) s is that early in development arr1 meristem sizes are highly similar to wt (darkblue line in Figure 7A), while at later stages arr1 meristems are only slightly smaller than arr1arr12 (lightblue line in Figure 7A, approximately 13 cell difference) (For experimental counterparts see (Dello Ioio et al., 2007; Moubayidin et al., 2010). This absence of early differences between the arr1 and wt can be easily understood from ARR1 not being active early during development, causing meristem dynamics to be dominated by ARR12, while the small and relatively constant difference at later stages implies a limited effect of ARR12 on final meristem size. When we compare wildtype and arr12 mutant meristem dynamics, we see again a small difference in final meristem size with arr12 mutants having slightly larger meristems than wildtype, consistent with a limited effect of ARR12 on meristem size. However, we now also see that this difference in meristem size already occurs from early stages of development onwards, in line with the early activation of ARR12. This early onset of ARR12 effects on meristem size, combined with this effect remaining relatively constant over time puts certain constraints on the model parameter settings.

Our experimental data indicates that ARR12 antagonizes the auxin-PLT positive feedback loop both through repressing PLT transcription and through reducing auxin levels. Naievely, one may expect that similar root zonation dynamics could be obtained through

Please cite this article in press as: Salvi et al., A Self-Organized PLT/Auxin/ARR-B Network Controls the Dynamics of Root Zonation Development in *Arabidopsis thaliana*, Developmental Cell (2020), https://doi.org/10.1016/j.devcel.2020.04.004

various combinations of these antagonistic effects, and that a decrease in ARR12 mediated PLT repression can be compensated for with an increase in ARR12 mediated auxin antagonism. However, by playing around with hypothetical ARR12 variants in which ARR12 either only antagonizes PLT expression or only antagonizes auxin levels, we find that this is not the case (for settings used see section on alternative model settings). Given the delay between auxin signalling and PLT transcription, ARR12 mediated PLT antagonism has a relatively faster effect on root zonation dynamics than its auxin antagonism and as such is important particularly in the early phases of root development (Figure 6C). In contrast, at later stages when the PLT protein gradient has extended, and has thus pushed the ARR12 domain to lie at some distance from the PLT transcriptional domain, the ARR12 mediated auxin antagonism gains importance (Figure 6C).

As an additional constraint for the ARR12-set of parameters we require the model to fit the experimentally observed ARR12 expression domain. Parameters for auxin dependent induction and PLT dependent repression of ARR12 are chosen such that combined these interactions ensure that ARR12 are kept outside the PLT protein gradient domain and start to become expressed shootward of the meristem (Figure 6A). Due to cumulative cell growth and division, at the shootward end of the meristem cells become displaced at a significant rate. As a consequence, to maintain stable root zonation and thus ARR12 patterning, ARR12 expression needs to become continuously reestablished in newly arriving cells. This requires sufficiently fast ARR12 production and degradation rates. Finally, we use the differences between the experimentally determined PLT protein gradient dynamics in wt and arr12 plants to determine the effect ARR12 signalling should have on PLT patterning.

Step 4: The Auxin-PLT-ARR12-ARR1 Model Simulating the Wildtype

As a final step we add the interactions between auxin, PLT and ARR1 mediated cytokinin signalling to our model, thus effectively simulating a wildtype plant (blue lines in Star Method Figure 1A). Auxin dependence of ARR1 induction, and ARR1 production and degradation rates are set similar to ARR12, to obtain a similar expression domain and rapid enough ARR1 induction to compensate for the continuous displacement of cells, as explained above. Additionally, we assume a similar effect of ARR1 on the ElongTF factor controlling the transition to elongation and differentiation (Equation 2).

We again determine the remaining parameter settings (indicated by & in Star Method Tables 5 and 6, indicated by ARR12 knockout) for ARR1 dependent interactions from our experimental data on PLT gradient dynamics and meristem size growth dynamics. Comparing meristem growth dynamics for wild type, arr1, and arr12 single mutants, and arr1,arr12 double mutants shows that ARR1 has no effect on meristem size early in development, consistent with it only becoming active at 5dpg. Furthermore, this comparison demonstrates that ARR1 has a substantially larger effect on final meristem sizes than does ARR12.

A major question thus is what explains this larger effect on final meristem size. Importantly, in the current study we revealed that ARR12 does, yet ARR1 does not repress PLT transcriptional output (Di Mambro et al., 2017). Thus, ARR1 only antagonizes the auxin-PLT positive feedback loop through reducing auxin but not PLT levels. Given the stronger effect of ARR1 on final meristem dynamics this may imply that either the effect of ARR1 on SHY2 and GH3.17 expression is stronger than that of ARR12. Previous work (Moubayidin et al., 2010) has shown that SHY2 is more strongly activated by ARR1 than ARR12. We assume the same holds for GH3.17 and conservatively assume ARR1 has twice as strong an effect on both SHY2 and GH3.17 as ARR12.

Additionally, we showed that ARR1, but not ARR12, affects the KRP2 gene influencing cell division dynamics (Figure 7), thus part of the stronger effect of ARR1 on meristem size may arise through its KRP2 mediated influence on division dynamics at the shootward end of the meristem.

In order for ARR1, via KRP2, to affect the size of the zone in which cells divide, ARR1 has to necessarily be expressed in cells in which, in absence of KRP2, PLT levels would still support division. Under conditions in which we assume an identical auxin-induction and PLT-repression of ARR1 and ARR12, and hence identical expression domains, tuning parameters such that ARR1 is able to influence the division domain would result in appropriate meristem size dynamics for wt, arr1 and arr1,arr12 roots, but not for arr12 roots. In the latter case, a too large effect of ARR12 on meristem size as compared to experimental conditions was observed. This can be understood from the fact that ARR12 but not ARR1 represses PLT expression. As a consequence, positioning the ARR domains such that ARR1 can affect the division domain results in a too large repressive effect of ARR12 on PLT expression. We solved this discrepancy by assuming a less strong repressive effect of PLT on ARR1 (higher Km), and a stronger induction by auxin of ARR1 (lower Km). As a consequence, the ARR1 domain is positioned somewhat more rootward relative to the ARR12 domain. In this manner, we can obtain a situation in which ARR1 is effective in influencing the division domain via KRP2, while also reproducing the small effect ARR12 mutation has on meristem size for which a somewhat larger distance to the PLT expression domain is required.

Assuming that ARR1 effects on SHY2 and GH3.17 are only double those of ARR12, and assuming the somewhat more rootward domain of ARR1, our model simulations indicate that the ARR1 effect on KRP2 contributes significantly to meristem size stabilisation (Figure 7A).

We conclude that the best agreement with experimental data is achieved when we assume that ARR1 differrs from ARR12 in several aspects, i.e. that it affects divisions thereby mildly affecting meristem size, that it is less strongly repressed by PLT s enabling it to operate more independently form ARR1, and that it has a somewhat stronger effect (2 fold) on SHY2 and GH3.17 expression.

Please cite this article in press as: Salvi et al., A Self-Organized PLT/Auxin/ARR-B Network Controls the Dynamics of Root Zonation Development in *Arabidopsis thaliana*, Developmental Cell (2020), https://doi.org/10.1016/j.devcel.2020.04.004

Alternative Model Settings

To disentangle the contribution of ARR12 mediated auxin and PLT antagonism on meristem dynamics and determine their relative strengths and contributions to meristem size control we performed alternative simulations in which ARR12 only antagonizes auxin, or only antagonizes PLT (Figure 5C). Parameter settings used in these simulations are given below.

Star Method Table 12. ARR12 only antagonizes auxin not PLT

Parameter	explanation	Altered value	Original value
Ad_{GH317}	Maximum effect of GH3.17 increased	$2.32*10^{-6}$	$1.16*10^{-6}$
$KM_{ARRs,GH317}$	We drastically lower the KM at which ARR12 induces GH3.17	35	75
$KM_{ARRS,PINs}$	We drastically lower the KM at which ARR12 induces SHY2 mediated PIN repression	35	75
$PIN_{ARRs}fac$	Maximum repression of PINs increased	0.5	0.25
ARR12Pltsrepressfrac	No ARR12 repression of PLT in this scenario	0	1

Star Method Table 13. ARR12 only antagonizes PLT not auxin.

Parameter	Explanation	Altered value	Original value
Ad_{GH317}	No Gh317 effect in this scenario	0	$1.16*10^{-6}$
Maxarrpinregfac	No PIN repression by ARR12 in this scenario	0	.25
ARR12Pltsrepressfrac	Maximum possible repression of PLT transcription by ARR12	1	1
$KM_{ARR12,Plts}$	Lower KM allows ARR12 to more effectively block PLT transcription	20	30
$KM_{Plts,ARR12}$	Weaker KM allow ARR12 to penetrate into the PLT transcription domain more effectively	30	25

To demonstrate the importance of auxin induction for ARR patterning, we performed an alternative simulation in which ARR expression is made auxin independent (Figure 5A). For this we reformulated Equation 11 into Equation 18:

$$\frac{dARR_{12}}{dt} = \frac{p_{ARR12} * KM^2_{Plts,ARR12}}{Plts^2 + KM^2_{Plts,ARR12}} - d_{ARR12} * ARR_{12} \quad \text{(Equation 18)}$$

To compensate for the accompanying increase in ARR12 levels, we lowered the saturation constant for PLT mediated ARR12 repression (ARR12KMPlts). from 30 to 15. This enables us to reduce changes in overall ARR12 levels, enabling a better focus on spatial pattern specific changes (see Figure S6C).

STAR Method Table 14. ARR12 without auxin induction

Parameter	Explanation	Altered value	Original value
$KM_{Auxin,ARR12}$	Set to 0 so that ARR12 is independent of auxin	0	175
$KM_{Plts,ARR12}$	Lowered to demonstrate that PLT is unable to keep ARR12 from penetrating cortex even at very strong repression	15	25

To demonstrate the need for growth to create the PLT drop, we performed a simulation in which we prevented meristem growth (Figures S3A–S3D). We find that in this simulation the PLT protein levels continue to rise over time. We additionally show the importance of cell growth mediated dilution on PLT patterning (Figures S3B and S3C). For this we performed an alternative simulation in which cell growth induced dilution of PLT proteins is ignored, while all other factors dilute at the regular, cell volume increase dependent rate. To make sure that the increase in meristem size is due to a lack of PLT dilution, and not due to a lack of ARR12 ability to repress PLT, we additionally lower the KM at which ARR12 effectively represses PLT. Without dilution the PLT gradient expands rapidly (Figure S3B) and meristem size expansion is not slowed effectively (Figure S3C).

Finally, to show that our experimental data imply that significant PLT expression and protein is present prior to germination, we performed an alternative simulation using an alternative initial condition with lower PLT expression and protein levels (STAR Method Figure 1C). To illustrate, that a reduced initial level of PLT can not be compensated for by enhanced PLT production, we doubled the

maximum PLT production rate p_{Plts} to 0.00175. Our simulations demonstrate that the slow auxin-dependent induction pathway of PLT transcription rate makes it impossible for the additional production to compensate for the lower initial levels by 24 hpg (see Figure S3E).

STAR Method Table 15. Altered growth conditions no growth or no growth PLT dilution

Parameter	Explanation	Altered valueValue	Original value
Divtime	Growth turned off to demonstrate lack of PLT drop without growth (Figures S3A and S3D)	Infinite	36000
PLT Dilution	Dilution of PLT turned off to demonstrate importance of dilution to halting growth (Figures S3B and S3C)	0	0.5
$KM_{ARR12,Plts}$	Demonstration that ARR12 invasion into meristem is not due to lack of PLT suppression (Figure S5C)	10	25
p_{Plts}	Combined with lower initial PLT (STAR Methods 1C) level to show that doubling production cannot compensate a lowered initial PLT condition. (Figure S3E)	0.0175	0.00875

Model Code and Simulation

The models were written in C++. Numerical integration of cell-level ODEs was done using simple Euler forward integration, using a timestep of 2s. For integration of the PDE describing auxin dynamics, an alternating direction implicit integration scheme was used (Peaceman and Rachford, 1955), with a timestep of 0.2s and a spacestep of 1 microm.

QUANTIFICATION AND STATISTICAL ANALYSIS

Statistical analysis was performed using online resources: GraphPad (http://www.graphpad.com) for Student's t-test and (https://www.socscistatistics.com/tests/anova/default2.aspx) for the 1-way ANOVA. For all experiments, analyses were performed in sufficiently large samples to ensure statistical significance, as reported in corresponding figure legends and paragraphs of STAR Methods - Method detail section.

No statistical sample size predetermination nor randomization were undertaken. Criteria for data and samples inclusion and exclusion are reported in the corresponding STAR Methods - Method detail section. The investigators were not blinded to allocation during experiments and outcome assessment.

All the statistical details of each experiment (including, -whenever present- the statistical tests used, values of n, mean, SD, SE, confidence intervals) can be found in the corresponding figure legend (and further details in the corresponding Method Details subsections). For all figures, representative pictures of samples were chosen. In figures, statistical significance is conventionally indicated by * and the p-value is reported in the corresponding figure legend.